Multi-dimensional higher resolution methods for flow in porous media.

Lamine, Mohamed Sadok

Swansea University
Prifysgol Abertawe

Multi-Dimensional Higher Resolution Methods for Flow in Porous Media

Mohamed Sadok Lamine

Submitted to the University of Wales Swansea
in fulfilment of the requirements for the Degree of Doctor of Philosophy

March 31^{th} 2009

Civil and Computational Engineering Centre
School of Engineering
Swansea University
Singleton Park, Swansea SA2 8PP
Wales, United Kingdom

Summary

Currently standard first order single-point upstream weighting methods are employed in reservoir simulation for integrating the essentially hyperbolic system components. These methods introduce both coordinate-line numerical diffusion (even in 1-D) and cross-wind diffusion into the solution that is grid and geometry dependent. These effects are particularly important when steep fronts and shocks are present and for cases where flow is across grid coordinate lines.

In this thesis, families of novel edge-based and cell-based truly multidimensional upwind formulations that upwind in the direction of the wave paths in order to minimise crosswind diffusion are presented for hyperbolic conservation laws on structured and unstructured triangular and quadrilateral grids in two dimensions. Higher resolution as well as higher order multidimensional formulations are also developed for general structured and unstructured grids.

The schemes are coupled with existing consistent and efficient continuous CVD (MPFA) Darcy flux approximations. They are formulated using an IMPES (Implicit in Pressure Explicit in Saturation) strategy for solving the coupled elliptic (pressure) and hyperbolic (saturation) system of equations governing the multi-phase multi-component flow in porous media.

The new methods are compared with single point upstream weighting for two-phase and three-component two-phase flow problems. The tests are conducted on both structured and unstructured grids and involve full-tensor coefficient velocity fields in homogeneous and heterogeneous domains. The comparisons demonstrate the benefits of multidimensional and higher order multidimensional schemes in terms of improved front resolution together with significant reduction in cross-wind diffusion.

Declaration and Statements

Declaration

This work has not been previously accepted in substance for any degree and is not being currently submitted in candidature for any degree.

Signed_____.(Candidate)
Date_____01/08/09_____.

Statement 1

This dissertation is being submitted in partial fulfilment of the requirements for the degree of doctor of philosophy.

Signed_____.(Candidate)
Date_____01/08/09_____.

Statement 2

This dissertation is the result of my own independent work/investigation, excepts where otherwise stated. Other sources are acknowledged by footnotes giving explicit references. References are appended.

Signed_____.(Candidate)
Date_____01/08/09_____.

Statement 3

I hereby give consent for my dissertation, if accepted, to be available for photocopying and for inter-library loan, and for the title and summary to be made available to outside organisations.

Signed_____.(Candidate)
Date_____01/08/09_____.

Multi-Dimensional Higher Resolution Methods for Flow in Porous Media

Contents

Acknowledgements

I would like to express my deep and sincere gratitude to my supervisor, Professor Michael G. Edwards for his support, encouragement and guidance at all stages of my research.

My sincere thanks are due to the official referees Professor Michael J. Baines and Professor Perumal Nithiarasu for their review and constructive criticism.

I wish to extend my warmest thanks to all my friends who have supported me and made my stay at Swansea a very pleasant one.

My deepest gratitude goes to all my family for their help and moral support during my studies. My parents, Habib and Najet have inspired me to work hard and aim for the best. Thankyou for being there for me in times of need and advice, thankyou also for sharing with me in times of joy and celebration.

Finally, I thank God who gave me the strength in order to accomplish this work.

The financial support of EPSRC is gratefully acknowledged.

List of Figures

List of Tables

Chapter 1

Introduction and Background

Petroleum reservoir simulation involves the use of numerical methods to obtain the solution of mass, momentum and energy conservation equations (in integral or partial differential form) governing fluid flow in petroleum reservoirs. The need for accurate and realistic reservoir simulation has always driven the field of research and development of efficient and robust numerical discretisation techniques for reservoir simulation. There exists a number of different numerical discretisation approaches which are used in reservoir simulation. One such approach is the *finite volume method* (FVM). Most of the existing numerical reservoir simulators employ a *single point upstream weighting* (SPU) first order scheme for the fluid transport equations that suffers both excessive smearing at saturation and concentration fronts as well as a grid dependency introducing a cross diffusion error into the numerical solution. The main focus of this thesis is to investigate and develop novel higher resolution finite-volume numerical discretisation techniques for the reservoir simulation saturation equation.

1.1 Reservoir Simulation

1.1.1 Petroleum Reservoirs and Recovery processes

A subsurface reservoir is a geological formation in which fluids have accumulated over millions of years by migration from source rocks. The reservoir rock is typically sedimentary in nature subject to forces including fluid pressure, viscous, capillary and gravity. Naturally occurring hydrocarbon systems found in petroleum reservoirs are mixtures of organic compounds which exhibit multi-phase behavior over wide ranges of pressures and

temperatures. These hydrocarbon accumulations may occur in the gaseous state, the liquid state, the solid state, or in various combinations of gas, liquid, and solid.
In order to recover oil and gas wells are drilled into the reservoir, some of which produce (*producer*) oil and others are used to inject (*injector*) water or gas to provide pressure support. The recovery of oil by any of the natural drive mechanisms is called **primary recovery**. This term refers to the production of hydrocarbons from a reservoir without the use of any process (such as fluid injection) to supplement the natural energy of the reservoir. **Secondary recovery** aims at increasing the efficiency of oil displacement towards the production wells and uses techniques such as *water flooding*. Usually, **tertiary production** methods also referred to as **enhanced oil recovery** processes are necessary in order to attain efficient levels of oil recovery. These techniques include *polymer flooding* and *miscible displacement*. Polymer flooding involves the addition of polymer substances to injected water in order to increase the viscosity of the water and displace the trapped oil in the rock pores. Miscible displacement consists of mixing gaseous fluids with oil to form a single phase. The single flow regime between the oil and gas phase reduces interfacial tensions and can result in more effective displacement.
In the oil industry the goal is to maximise hydrocarbon recovery under different conditions. This depends on deriving mathematical and physical models for the processes that occur in the reservoir. The models should incorporate as much geology and physics as necessary to describe the essential phenomena and lead to coupled systems of nonlinear partial differential equations. Discretised numerical models are then derived that has the required properties of accuracy and stability and which must produce solutions representing the basic features without introducing spurious non physical phenomena.

1.1.2 Reservoir Simulation and Numerical Discretization

Reservoir simulation is that process whereby the behavior of a hydrocarbon reservoir is inferred from the behavior of a mathematical model which describes it [128, 13]. The degree to which the model duplicates the actual reservoir is a function primarily of the input data used, and secondly the adequacy of the model to simulate the physical system. The current state of the art in reservoir simulation is directly related to high speed computers, accurate geological models for reservoir description and robust numerical techniques. With increased computer power, numerical simulation has become an efficient reservoir management tool for all stages in the life of a reservoir, as larger amounts of data are

incorporated in more geologically realistic models that describe the complex behaviour of multi-phase flow in real reservoirs. Reservoir simulation has become very advanced over the past decades. Simulation grids may be very large, and the level of details can be very high. One of the reasons for the high level of details is the considerable effort which is put into seismic measuring and other techniques prior to drilling exploration wells. Also, the history may be well known for a reservoir that have been producing hydrocarbons for many years through logging and measured production etc. This may be used to verify or history match geophysical data. Parameter estimation is an important area in its own, and production data is essential to recalculate/calibrate a model with respect to porosity and permeability. Because the geology may be estimated at such a detailed level, one may be required to model flow on grids incorporating general complex geometry.

Three basic problem areas have dominated much of the recent research in reservoir simulation. First, the need for an effective model to describe the complex fluid and rock interactions that control recovery processes. Simulators are severely hampered by the lack of knowledge of reservoir properties, heterogeneities, and relevant length scales and of important mechanisms such as diffusion, dispersion, and viscous instabilities. Russell and Wheeler [145] and Young [167] present excellent surveys of the influence of dispersion and attempts to incorporate it in present reservoir simulators. Since the mixing and velocity variations are influenced at all relevant length scales by the heterogeneous properties of the reservoir, there is a need for volume averaging of porosity and permeability. Recently, developments have been made in homogenization [85, 96], renormalisation [98, 51], scaled averaging [97], upscaling [20, 47], multi-scale methods [87, 27, 95, 12], and statistical methods have also been explored to obtain effective permeability [14, 72]. A review of different upscaling techniques used in petroleum reservoir simulation is also presented in [70]. Also, simulators are now used as an experimental tool to develop methods to model the interrelations between localized and large scale media effects.

Next, the need to develop accurate discretisation techniques that retain the important physical properties of the continuous models. Recently, a variety of new discretisation techniques have been developed for both the pressure and transport equations. Discontinuous Galerkin (DG) [135, 137], Mixed finite elements (MFEM) and related methods [145, 67, 66, 44, 45, 69, 48, 11, 90], and finite volume methods (FVM) [61, 50, 62, 53, 2, 161, 3, 4, 5, 1] are being used to yield accurate mass-conservative approximations to the pressure and Darcy velocity of the fluid. Eulerian-Lagrangian techniques [25, 42, 146]

have also been developed that not only conserve mass but also take advantages of the computed flow of the fluids to accurately model the transport phenomena. Adaptive local grid refinement in space and time [65, 51] can be controlled by A posteriori error estimators. Then multi-grid or multilevel iterative techniques [68, 84] can be used to efficiently solve the discrete systems.

Finally, the need to develop efficient numerical solution algorithms that utilize the potential of the emerging computing architectures. Major potential advantages in computing lie in emerging parallel computer architectures and use of parallel computation for Large-Scale Reservoir Simulation [168]. Techniques such as domain decomposition e.g. [165, 120] that naturally split a large problem into smaller pieces to be addressed separately on distinct processors, which also allows modularized local grid refinement and can play a significant role in developing effective and robust simulation codes.

1.2 Scope of Work and Research Contribution

The work documented in this thesis presents a number of developments in numerical discretisation techniques for the subsurface reservoir simulation saturation equation. The advantages and limitations of some of these formulations are discussed and analysed in this work with the help of numerical tests. The major objective of this thesis is to address the important aspects of higher resolution methods for flow in porous media on unstructured grids in two space dimensions.

1.2.1 Summary of Major Work

The main objective of this thesis is to develop higher resolution multidimensional and higher order cell vertex finite volume methods for convective flow in porous media on structured and unstructured grids. The schemes are coupled with existing control volume distributed full tensor Darcy flux approximations. The principal accomplishments of this work are listed below:

(i) A study of a family of novel truly multidimensional schemes for convective flow in porous media on structured and unstructured quadrilateral and triangular grids in 2D. Details of the formulation are documented in [107, 102, 105, 103, 104].

(ii) An extension of a class of higher order methods to unstructured highly distorted

grids. A sequence of higher resolution non-uniform limiters are introduced and tested for classical two phase flow problems in porous media on a range of unstructured grids. The outcome of this research is documented in [109, 108, 106].

(iii) The implementation of a novel class of higher order multidimensional schemes for flow in porous media on unstructured meshes [101].

(iv) Applications of the above schemes to two phase flow and three component two-phase flow systems driven by viscous and gravity forces in homogeneous and heterogeneous domains.

The research outputs in this study are listed in the bibliography of this thesis.

1.2.2 Organization of the Thesis

The thesis is subdivided into eleven chapters, including an introduction and conclusion. The synopsis of each chapter is as follows.

The flow equations of mass and momentum conservation for fluid flow in porous media are introduced in **Chapter 2**. Description of the problem to be solved with specified boundary and initial conditions is also presented in this chapter.

Chapter 3 presents a literature review of previous work on higher resolution and higher dimensional upwind finite volume discretisation schemes employed in petroleum reservoir simulation. Limitations of standard single point upstream weighing finite volume schemes are discussed.

Chapter 4 is devoted to the details of the discretisation of the coupled system of hyperbolic and elliptic equations. Formulations of edge-based and cell-based vertex-centered upwind finite volume approximations for the saturation equation are considered. Also, a review of multi-point control-volume distributed CVD (MPFA) approximations of the Darcy flux are presented. The solution strategy and time stepping algorithm are then proposed. Finally, an overview of discrete local maximum principles for hyperbolic equations is presented.

Higher-order upwind schemes on highly distorted unstructured triangular grids in 2D, are the subject of **chapter 5**. The schemes are coupled with consistent Darcy flux approximations. Non-uniform grid limiters are presented and the schemes are tested on a series of test cases for two phase flow in porous media.

Chapter 6 is devoted to a class of novel locally conservative edge based truly multidimensional schemes, for structured and unstructured quadrilateral grids. Extensions to triangular and hybrid meshes is proposed in **chapter 7**. Two phase flow results are tested on a range of grids with variations in spacing and orientation. Numerical cases involve both diagonal and full homogeneous permeability tensors for high mobility ratios.
Applications of the edge based schemes to gravity driven flows and to compositional flow systems using different combinations of upwind and tracing formulations are investigated throughout numerical case studies in **chapter 8**.
Chapter 9 presents novel families of cell-based multidimensional schemes for convective flow in porous media on unstructured grids. A stability analysis is performed for linear flux and a class of weighting factors is derived on triangular and quadrilateral elements.
Chapter 10 introduces novel families of higher order multidimensional schemes for convective flow in porous media. The formulation of these methods is established using both edge based and cell based finite volume approximations. Different versions of the schemes are compared with the standard methods with the help of numerical tests on homogeneous and heterogeneous permeability fields for different types of structured and unstructured grids.
Finally, the last chapter summarizes the novel research contributions of this work and recommendations are made for continuation of this work through future research.

Chapter 2

Flow Equations

The purpose of this chapter is to introduce the principal equations governing the flow in porous media, which are modelled in this thesis. Fluid flow in porous media is governed by the fundamental laws of conservation of mass, momentum and energy. Additionally, several empirical relations comprising PVT-relations, rock and fluid properties and multi-phase flow behaviour are necessary to build a mathematical representation of the physical problem that is as realistic as possible. For reference, textbooks including Peaceman [128], Aziz and Settari [13], Bear [19] give further details on the subject. This chapter is organised as follows. In section 2.1 we will briefly cover the primary physical and geological parameters influencing the flow. Section 2.2 presents the Darcy's Law and the flow equations governing single and multi-phase flow. Throughout the dissertation, we consider two different models for flow in porous media namely:

- a *two-phase immiscible flow* model and
- a *three-component two-phase immiscible flow* model,

The above models are discussed in more detail in section 2.3.

2.1 Model Parameters

2.1.1 Rock Parameters

Porous media are made up of pore spaces and a solid matrix. The distribution and volume fraction of such pores in the rock determine the rock properties, which in turn are the parameters governing the hydrocarbon flow in the reservoir.

Porosity

The rock porosity, referred to as Ψ, is a scalar dimensionless *static* entity which corresponds to the void volume fraction of the medium, that is, $0 \leq \Psi \leq 1$. The porosity usually depends on the pressure. In simplified models, it is customary to assume that Ψ only depends on the spatial coordinate. We assume, without loss of generality with respect to the numerical methods presented, that the porosity is equal to unity.

Permeability

The absolute permeability, denoted by $\mathbf{K}$, is a measure of the rock's ability to transmit a single fluid at certain conditions. In general, for flow in higher dimensions, the permeability is modelled via a spatially varying *full tensor* $\mathbf{K}$, which means that the permeability in the different directions depends on the permeability in the other directions. In 2D, the permeability tensor takes the form:

$$\mathbf{K} = \begin{bmatrix} K_{11} & K_{12} \\ K_{12} & K_{22} \end{bmatrix}.$$

This tensor must be symmetric and positive definite to ensure a physically consistent conductivity.

In the case where $\mathbf{K}$ is diagonal, the medium is said to be *isotropic* if $K_{11} = K_{22}$, as opposed to *anisotropic* corresponding to $K_{11} \neq K_{22}$.

Moreover, due to rock formations, the permeability may vary rapidly over several orders of magnitude across the porous medium. Under the influence of insitu stress, fractures may open or close at depth and therefore affect drastically the bulk permeability.

Furthermore, since the definition of permeability involves a certain fluid, different fluids will experience different permeability in the same rock sample. This is usually modeled through relative permeabilities discussed below.

2.1.2 Fluid properties

Saturation and Concentration

The void in the porous medium is assumed to be filled with different *phases*. The volume fraction occupied by each phase p is the saturation S_p. By definition,

$$\sum_p S_p = 1. \tag{2.1.1}$$

For practical reservoir purposes, usually only three phases are considered namely aqueous (w), oleic (o) and gaseous (g) phase. Each phase contains one or more *components*. A hydrocarbon component is a unique chemical species. The mass fraction of a component l in a phase p is denoted by C_{lp}. In each of the phases, the mass fractions should add up to unity, so that for N different components, we have:

$$\sum_{l=1}^{N} C_{lp} = 1, \text{ for each phase } p. \tag{2.1.2}$$

Density and Viscosity

Next, we assign a *density* ρ_p and a *viscosity* μ_p to each phase p. In general, these are functions of *phase pressure* ϕ_p and the composition of each phase. In this work, compressibility effects are neglected. Also the phase densities are assumed to be constant for the models considered.

Capillary Pressure

Due to interfacial tensions, the phase pressures are different, defining the capillary pressure as:

$$\phi_{cij} = \phi_i - \phi_j,$$

for the phases i, j. It is usually assumed that the capillary pressure is a function of the saturation only. In the rest of the dissertation, capillary effects will be neglected.

Relative Permeabilities

The relative permeability, k_{rp} of phase p is introduced to account for the reduced permeability of each phase due to the presence of the other phases. Typically, this parameter is chosen to be an empirical function of the phase saturation. For two phase flow problems, Brooks and Corey [24], Corey [37] and Van Genuchen [158] have suggested analytical expressions for the relative phase permeabilities. Here, we use the following simplified model:

$$k_{rp} = S_p^{\zeta}, \tag{2.1.3}$$

where S_p denotes the normalised saturation variable of phase p and ζ denotes the order of mobility.

Phase Mobilities

Fluid phase mobility is defined as the ratio of the relative permeability to phase viscosity [39]. The p^{th} phase mobility is written as:

$$\lambda_p = k_{rp}/\mu_p. \tag{2.1.4}$$

2.2 Constitutive Equations: Conservation Laws

2.2.1 Continuity Equations: Mass Conservation Laws

For multiphase flow, the mass conservation equation (continuity equation) takes the form:

$$\frac{\partial \rho_p \Psi S_p}{\partial t} + \nabla \cdot (\rho_p V_p) = \rho_p q, \tag{2.2.1}$$

where V_p denotes the p^{th} phase velocity and q refers to the source or sink term. We assume throughout this thesis that:

- the flow is incompressible. Consequently, ρ_p is constant.
- Also, the porosity Ψ is set to unity.

Then Equation (2.2.1) simplifies to :

$$\frac{\partial S_p}{\partial t} + \nabla \cdot V_p = q. \tag{2.2.2}$$

2.2.2 Equation of Motion: Darcy's Law

The movement of water, oil and natural gas through the subsurface is a very complex phenomenon because of the involved microscopic scale and heterogeneity of the medium. Usually the velocity of the flow is so small ($Re << 1$) and the flow passages are so narrow that laminar flow may be assumed. Rigorous analysis of the flow is not possible because of complexity of the shape of the individual flow passages. Although, several theories have been formulated, credit is attributed to the French engineer *Henry Darcy* [40], who published his famous work on the public fountain of the French city of *Dijon*. Darcy's law models the effective velocity across a representative elementary volume (REV).

Phase Velocity Formulation

For single phase flow, the compact differential form of Darcy's law is written as:

$$\mathbf{V} = -\frac{\mathbf{K}}{\mu}(\nabla\phi + \rho g \nabla h). \tag{2.2.3}$$

Here, μ is the fluid viscosity, g is the gravitational constant, h is the spatial coordinate in the upward direction and ϕ is the pressure. When several phases or components are present in porous media, Darcy's law may be extended to describe simultaneous flow of more than one phase:

$$\mathbf{V}_p = -\lambda_p \mathbf{K}\left(\nabla\phi + \rho_p g \nabla h\right). \tag{2.2.4}$$

Total Velocity Formulation

The total Darcy velocity, which is the sum of the phase velocities, is defined as: Define the total Darcy velocity as:

$$\mathbf{V}_T = -\Lambda \mathbf{K}(\nabla\phi + \overline{\rho} g \Delta h), \tag{2.2.5}$$

where

$$\Lambda = \sum_{p=1}^{N_p} \lambda_p, \tag{2.2.6}$$

is the total mobility. Let

$$\overline{\rho} = \sum_{p=1}^{N_p} \rho_p \lambda_p / \Lambda \tag{2.2.7}$$

is the mean density and

$$\Delta\rho(S) = \rho_p - \overline{\rho}. \tag{2.2.8}$$

The p^{th} phase velocity is then defined by

$$\mathbf{V}_p = f_p(\mathbf{V}_T - \Delta\rho(S) g \mathbf{K} \nabla h), \tag{2.2.9}$$

where f_p is the fractional flow of phase p, i.e.

$$f_p(S) = \frac{\lambda_p}{\Lambda}. \tag{2.2.10}$$

2.3 Governing Equations

2.3.1 Immiscible Two Phase Flow

The Buckley-Leverett model for flow of two immiscible incompressible phases in a porous medium is important to models of oil reservoirs and contaminated aquifers. In this model, we assume that the fluid consists of two distinct phases. It is assumed that the molecules forming the two phases do not interact or move from one phase to the other. In the following, a water-oil system is considered, phase quantities bear suffices w for the aqueous phase (water) and o for the oleic phase. Recall that the saturations of the phases S_o and S_w are the ratios of the phase volumes to fluid volume. By definition,

$$S_w + S_o = 1.$$

Typically, water is the wetting phase, meaning that it prefers to move along the surface of the rock pores. Oil is the non-wetting phase, and prefers to sit as disconnected droplets in the centre of cell pores, or move as ganglia when the droplets can connect. Thus the presence of both oil and water reduces the flow of the other. In the absence of capillary forces, the Darcy velocities of the phases act so as to reduce the flow of each other and take the form:

$$\begin{aligned} \mathbf{V}_w &= -\lambda_w \mathbf{K}(\nabla\phi + \rho_w g \nabla h), \\ \mathbf{V}_o &= -\lambda_o \mathbf{K}(\nabla\phi + \rho_o g \nabla h). \end{aligned} \tag{2.3.1}$$

The Buckley Leverett flow model of two incompressible fluids is described, using the fractional approach, by an elliptic equation for the pressure ϕ:

$$-\nabla\Lambda \cdot \mathbf{K}\nabla\phi = \tilde{M}, \tag{2.3.2}$$

and a hyperbolic equation for the saturation, neglecting the capillary pressure and dispersion. The saturation equation is written as:

$$\Psi\frac{\partial S}{\partial t} + \nabla \cdot \mathbf{V}_w(S) = m, \tag{2.3.3}$$

where S is the water saturation, m is the distributed source term, the porosity $\Psi = 1$ and $\mathbf{V}_w$ takes the form:

$$\mathbf{V}_w(S) = f(S)(\mathbf{V}_T - \lambda_o g \Delta\rho \mathbf{K}\nabla h), \tag{2.3.4}$$

where $\mathbf{V}_T = \mathbf{V}_w + \mathbf{V}_o$ is the total velocity. Here, $\Delta\rho = \rho_w - \rho_o$.

Buckley-Leverett Model in 1D

In one dimension, in the absence of source and sink terms, the conservation equation (2.3.3) reduces to:

$$\frac{\partial S}{\partial t} + \frac{\partial V_w}{\partial x} = 0, \tag{2.3.5}$$

and Equation (2.3.1) takes the form

$$V_w = -\lambda_w K(\frac{\partial \phi}{\partial x} + \rho_w g \frac{\partial h}{\partial x}). \tag{2.3.6}$$

The phase velocity is expressed in terms of total velocity $V_T = V_w + V_o$ as

$$V_w = f(S)(V_T - \lambda_o \Delta\rho g \frac{\partial h}{\partial x}), \tag{2.3.7}$$

where f is the fractional flow.
Then, the incompressible flow condition, in 1-D, reduces to

$$\frac{\partial V_T}{\partial x} = 0, \tag{2.3.8}$$

from which it follows that the total velocity is spatially constant in 1-D for an incompressible flow. Equations (2.3.7) and (2.3.8) are used to determine pressure and velocity subject to initial and boundary conditions for the pressure and saturation. The saturation of the oil phase is deduced from the volume balance equation, where saturations sum to one. Dimensionless parameters that influence the Buckley-Leverett models considered here are the gravity number:

$$\gamma = \frac{Kg(\rho_w - \rho_o)}{\mu_o V_T}, \tag{2.3.9}$$

and the mobility ratio

$$M = \frac{\mu_o}{\mu_w}. \tag{2.3.10}$$

The gravity number is the ratio of gravity to viscous forces. The mobility ratio is one of the factors that determine the physical stability regime of the flow. In the case of mobility ratios larger than unity, small instabilities (typically due to heterogeneities in the medium) in the flow will grow and the displacement is destabilized [119, 43]. This leads to the development of patterns at the interface between the two fluids. These phenomena are referred to as *viscous fingering*. Gravity may act to stabilize or destabilize the flow. The Buckley-Leverett flux function is neither convex nor concave. This model is especially

interesting when both the total fluid velocity and gravity are nonzero. In the cases presented in this work, we use fractional flow functions of the form,

$$f = \frac{MS^{\zeta}}{MS^{\zeta} + (1-S)^{\zeta}},$$

where ζ is the order of mobility, S denotes the normalised water saturation and M is the mobility ratio defined above. Typical profiles of the Buckley-Leverett flux function for different gravity numbers are depicted in Figure 2.1. Solutions of the Buckley-Leverett equations exhibit sharp travelling wave fronts in oil and water saturations, followed by smooth expansion regions.

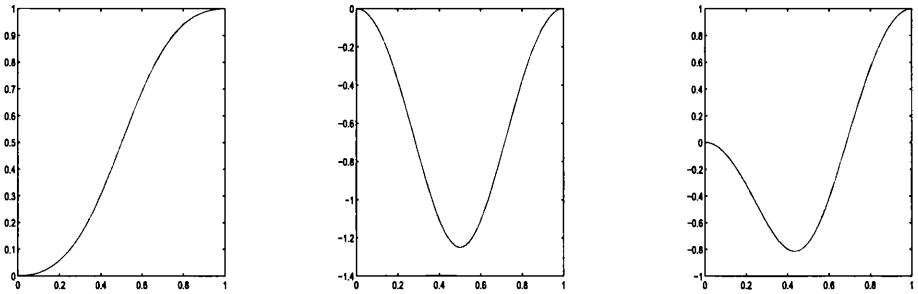

(a) $V_T = 1$, $g = 0$ (b) $V_T = 0$, $g = 10$ (c) $V_T = 1$, $g = 10$

Figure 2.1: Buckley-Leverett flux function: $V_w = f(S)(V_T - g(1-S)^2)$ with $f(S) = \frac{S^2}{S^2+(1-S)^2}$ for $\zeta = 2$.

2.3.2 Polymer Flood System: Three Component Two Phase Flow

The hyperbolic system considered here is comprised of a miscible aqueous phase (water and polymer concentration) together with an oil phase. Throughout the thesis, the concentration of a polymer solute is denoted by C; by definition C is the volume fraction of the polymer solute in the miscible phase. In one space dimension, the conservation equation in the absence of source and sink terms takes the form:

$$\frac{\partial \mathbf{S}}{\partial t} + \frac{\partial \mathbf{F(S)}}{\partial x} = \mathbf{0}, \tag{2.3.11}$$

where

$$\mathbf{S} = \begin{bmatrix} S \\ SC \end{bmatrix} \tag{2.3.12}$$

denote the vector of conservative variables and

$$\mathbf{F} = \begin{bmatrix} V_w \\ CV_w \end{bmatrix} \tag{2.3.13}$$

is the nonlinear flux vector. Let

$$\mathbf{C} = \begin{bmatrix} S \\ C \end{bmatrix} \tag{2.3.14}$$

denote the vector primitive variables. The phase velocity is defined by equations (2.3.6) and (2.3.7). Here, the oil saturation is $(1-S)$ and aqueous viscosity μ_w is now a function of polymer concentration C.

Characteristic Decomposition

The decomposition matrices of system Equations (2.3.11) are presented in [21, 51] and derived here for completeness.

Equation (2.3.11) can be expanded into the "quasilinear form":

$$\frac{\partial \mathbf{S}}{\partial \mathbf{C}}\frac{\partial \mathbf{C}}{\partial t} + \frac{\partial \mathbf{F}}{\partial \mathbf{C}}\frac{\partial \mathbf{C}}{\partial x} = 0 \tag{2.3.15}$$

where

$$\mathbf{T} = \frac{\partial \mathbf{S}}{\partial \mathbf{C}} = \begin{bmatrix} 1 & 0 \\ C & S \end{bmatrix},$$

and

$$J = \frac{\partial \mathbf{F}}{\partial \mathbf{C}} = \begin{bmatrix} \frac{\partial V_w}{\partial S} & \frac{\partial V_w}{\partial C} \\ \\ C\frac{\partial V_w}{\partial S} & V_w + C\frac{\partial V_w}{\partial C} \end{bmatrix}$$

is the local jacobian of the system with respect to primitive variables.

Assume $S \neq 0$, then multiplying Equation (2.3.15) by $(\frac{\partial \mathbf{S}}{\partial \mathbf{C}})^{-1}$ gives:

$$\frac{\partial \mathbf{C}}{\partial t} + \mathbf{T}^{-1}\mathbf{J}\frac{\partial \mathbf{C}}{\partial x} = 0, \tag{2.3.16}$$

with

$$\mathbf{T}^{-1}\mathbf{J} = \begin{bmatrix} \frac{\partial V_w}{\partial S} & \frac{\partial V_w}{\partial C} \\ \\ 0 & \frac{V_w}{S} \end{bmatrix}.$$

In the form Equation (2.3.16), characteristic speeds are the diagonal entries (also corresponding with the eigenvalues) of the matrix $\mathbf{T}^{-1}\mathbf{J}$, namely

$$\frac{\partial V_w}{\partial S} \text{ and } \frac{V_w}{S},$$

corresponding respectively with the eigenvectors

$$\begin{bmatrix} 1 \\ 0 \end{bmatrix} \text{ and } \begin{bmatrix} \frac{\partial V_w}{\partial C} \\ \frac{V_w}{S} - C\frac{\partial V_w}{\partial S} \end{bmatrix},$$

and the transformation matrix from conservative variables to characteristic variables $\mathbf{W}$ is given by:

$$\mathbf{R} = \begin{bmatrix} 1 & \frac{\partial V_w}{\partial C} \\ C & C\frac{\partial V_w}{\partial C} + S(\frac{V_w}{S} - \frac{\partial V_w}{\partial S}) \end{bmatrix}. \tag{2.3.17}$$

The matrix $\mathbf{R}$ can become singular if the eigenvalues $\frac{\partial V_w}{\partial S}$ and $\frac{V_w}{S}$ are equal.

2.4 Initial and Boundary Conditions

2.4.1 Hyperbolic Equation

For the initial value problem (IVP) field data is prescribed. For initial boundary value problems (IBVP), considered here in two-dimensions, an initial flow field is prescribed together with boundary values which are assigned according to the number of inward pointing characteristics [13]. Zero normal flow is imposed on solid walls.

2.4.2 Elliptic Equation

The two most common kinds of boundary conditions used in reservoir simulators with respect to the elliptic pressure equation are:

Dirichlet

This boundary condition requires the specification of pressure at the reservoir boundaries or wells. Typically, this involves specifying flowing bottom hole pressure at a well and a constant pressure at physical boundaries of reservoir.

Neumann

This boundary condition requires the specification of flow rates at reservoir boundaries. Typically, it involves specifying flow rates at wells and no-flow across physical solid boundaries of reservoir. Flow rates are specified or the pressure is specified at the boundary.

Chapter 3

Previous Work

In this chapter, some background work related to the topic of this thesis is described. A brief overview of the development of higher resolution methods is presented in section 3.1 and recent advances in modern multidimensional schemes for the transport equations are presented in section 3.2. Finally, section 3.3 presents state of the art of consistent Darcy flux continuous approximations based on control volume distributed (CVD) schemes for the pressure equation.

3.1 Motivation for the Development of Higher Resolution Schemes in Reservoir Simulation

One of the most important tasks in the numerical simulation of fluid flow problems is the reduction of numerical diffusion in the solution. Numerical diffusion is caused by the use of first order interpolation schemes in the approximation of the convective terms in the momentum equations introduced in chapter 2, Equation (2.2.4). First order upwind single-point upstream weighting schemes are still commonly employed in reservoir simulation for integrating the essentially hyperbolic components of the system, due to its simplicity and robustness of the resulting algorithm. However, these methods are known to introduce false coordinate-line numerical diffusion (even in 1-D) also referred to as *longitudinal* or *streamline diffusion.*

Also, as standard first order schemes rely upon upwind information that is determined according to the grid geometry; directional diffusion is introduced into the solution that is grid and geometry dependent. The effect can be particularly important for cases where

steep fronts and shocks are present and for cases where flow streamlines are not closely aligned with the grid coordinate lines and is known as *transverse* or *cross-wind diffusion* [132, 21, 36, 141, 142, 88, 6, 152].

Higher order convection schemes continue to be developed for the essentially hyperbolic systems of reservoir simulation [57, 51, 58, 56, 59, 21, 23, 48, 62, 157, 55]. These schemes require an extended support to obtain higher order accuracy and are constructed such that the solution remains free of spurious oscillations. These methods yield benefits in terms of improved front resolution and have been successfully demonstrated for a variety of multi-phase flow problems in reservoir simulation.

A more robust solution algorithm that is free of both cross-wind diffusion and spurious oscillations remains an area of research for reservoir simulation and is the target of this thesis.

Towards this goal, higher resolution schemes are presented for convective flow approximation on non-uniform distorted unstructured grids. This work continues with the development of the higher order unstructured grid schemes presented in [58, 56]. The convection schemes are coupled with continuous Darcy fluxes for approximation of the pressure equation and applied to multi-phase flow problems. The schemes are tested on unstructured grids with variable grid spacing and benefits of the resulting schemes in terms of improved front resolution are demonstrated for two-phase flow and three component two-phase flow test cases in two dimensions.

3.2 Higher Resolution Methods for Hyperbolic Conservation Laws

3.2.1 One Dimensional Case

In the case of one space dimension, upwind finite volume schemes have reached a degree of maturity where they can be considered as reliable tools for producing accurate numerical approximations of hyperbolic systems of partial differential equations.

Among the popular schemes that preserve the monotonicity of the solution are the upwind schemes introduced by Godunov [74], Engquist and Osher [64] and Roe [140]. These schemes are based on the solution of local or approximate Riemann problems. Central schemes including Lax Friedrichs are also used. These schemes are the basis of devel-

opment of higher order methods initiated by VanLeer [160] that provide second order accuracy in smooth regions and prevent the development of nonphysical oscillations near discontinuities.

High resolution schemes for conservation laws in one dimension are usually constructed using some form of TVD (total variation diminishing) limiter [156] so that high order accuracy can be achieved while avoiding spurious oscillations in the solution. Of interest here is the slope limiting (MUSCL) approach of van Leer , in which the limiter is applied in a geometric manner, to the gradients of a piecewise linear reconstruction of the solution, to create a monotonicity preserving scheme. At a given accuracy, the higher order schemes allow much coarser grids than the SPU scheme and hence require fewer calculations to produce accurate solutions. The computational time saved on the calculations outweighs the costs associated with higher order reconstructions. The details of such schemes is the subject of chapter 4.

TVD based methods have been used in the petroleum literature by several authors e.g. [143, 23]. The extension of higher order methods to compositional flow systems is nontrivial due to the strong, nonlinear coupling of the advection equation. Thiele and Edwards [157] developed novel TVD schemes for compositional streamline simulation in 1D.

Extensions to very high order methods include the piecewise parabolic method of Woodward and Collela [166] as well as the essentially non-oscillatory (ENO) type schemes of Osher-Shu [117] and weighted-ENO (WENO) schemes [116]. Harten *et al.* [77] introduced the ENO reconstruction that uses an adaptive stencil to achieve third and higher orders of accuracy.

In addition, the Runge-Kutta Discontinuous Galerkin (DG) methods [31, 35, 34, 32, 33, 29, 30], provide an attractive alternative to classical methods that have been employed in several applications. There has been an increasing interest in such methods in reservoir simulation due to its high accuracy and adaptability to general meshes. Riviere [135, 137, 136] applied the DG methods to solve the hyperbolic transport equations for miscible flow problems. More recently Hoteit and Firoozabadi [86] combined the DG methods with the mixed finite element methods to solve compositional flow problems.

3.2.2 Higher Order Schemes in Higher Dimensions

Extensions of one dimensional higher resolution methods to multi-dimensions were first constructed using serial techniques such as operator splitting [154, 113]. Neverthe-

less, the generalisation of these schemes on unstructured meshes rules out the use of the TVD condition which proves to be prohibitively restrictive on Cartesian meshes because the resulting scheme can be no more than first order accurate [74, 75], also monotonicity has limited meaning in multi-dimensions and is a one dimensional concept. Early TVD based extensions to higher dimensions in reservoir simulation include [143, 144, 26]. Spekreijse [153] proposed a new positivity criteria for unstructured grids, based on positivity of coefficients of the discrete form in a scalar conservation law. This resulted in a solid framework for the development of modern truly multidimensional higher resolution methods for conservation laws. The stability of the higher resolution formulations on general unstructured grids is based on ensuring that some form of discrete local maximum principle (DMP) is satisfied.

Work has been conducted by Jameson [91, 92] concerning limiting reconstructed solutions. This lead to the introduction of the local extremum diminishing (LED) schemes on unstructured triangular meshes in an edge-based finite volume framework. Unlike the TVD interpolation, the LED interpolation can be extended to an unstructured mesh while maintaining the positive coefficients of the discrete form for a scalar conservation law. This can be performed by calculating gradients of appropriate neighbouring triangles or edges and applying a discrete maximum principle [15].

Similar approaches have been carried out by Barth and Jesperson [16], Durlofsky et al. [46], Liu [114] and Batten et al. [18] employing slope limiting procedures for multidimensional cell-centered finite volume schemes for unstructured triangular meshes. More specifically, the limiting procedure involves the construction of an appropriate linear representation of the solution within a triangular element before it is limited in a manner that enforces the positivity constraint.

In the field of reservoir simulation, higher order Godunov schemes have been tailored to the equations of flow in a porous medium by Bell et al. [21] including application to black oil and compositional flow systems. The authors used a characteristic decomposition of the essentially hyperbolic system and adopted an Engquist-Osher (monotone) flux at the sonic points in order to ensure entropy satisfaction for expansion shocks.

This method was extended by Edwards [51] who introduced a higher-order Godunov scheme on non-uniform quadrilateral grids method with local dynamic grid adaptivity, where grid blocks are inserted in highly active regions of the flow field and removed from regions of inactivity. The new method was applied for two phase flow and three component

two phase flow problems. The quality of results computed by the adaptive higher-order scheme are comparable with those computed by the higher-order scheme on a uniform grid, globally refined to the level of the finest adaptive grid zones, while great savings in computer time are obtained (up to 64 times in two space dimensions) in comparison with standard upstream weighting methods. The adaptive higher order scheme is shown to be vastly superior compared to the first-order scheme on a uniform or adaptive grid.
Edwards [57] also presented higher order finite volume schemes based on the LED formalism for the hyperbolic equations coupled with the general tensor flux-continuous CVD (MPFA) approximation in 2D where both explicit and implicit time discretisations have been implemented. The comparison between higher order schemes for multi-phase flow in porous media coupled with CVD (MPFA) versus CVFE approximations for the pressure equations and demonstrate the benefits of the CVD coupled with higher order convection for heterogenous permeability fields in the resolution of the saturation fronts. The schemes have been formulated in a edge-based framework on general grids. Extensions of the formulations on arbitrary 3D grids of any cell type have been presented in [58].
One of the aims of this work concerns the extension of the above schemes to highly distorted unstructured grids and definition of the optimal non-uniform grid limiter. A sequence of non-uniform mesh limiters are also introduced and tested in application to multi-phase flow problems [106]. More details are given in chapter 5.

3.3 Modern truly Multi-dimensional Schemes for Hyperbolic Conservation Laws

3.3.1 Literature Review of Positive Multidimensional Schemes

While the use of higher order methods has been shown to be efficient in reducing the dependency of the numerical solution on the grid geometry [21], these schemes focus on reducing coordinate diffusion and require wide stencils.
An alternative approach, introduced in the literature in order to overcome cross-wind diffusion effects is known as truly multidimensional upwinding [142, 88]. The term truly or genuinely multidimensional schemes refers to schemes that consider the truly higher dimensional wave vector structure of the problem in higher dimensions unlike the dimensional splitting methods.

Multidimensional upwind schemes were developed initially for the approximation of steady state solutions of the two-dimensional Euler equations on unstructured triangular grids [142, 129, 83, 127].

More recently, several positive multidimensional advection schemes have been proposed in the CFD (Computational Fluid Dynamics) literature. These methods include the corner transport upwinding (CTU) [36], the N-scheme [138, 151] and the rotated grid H-box methods [22, 81] for Cartesian grids. These methods use characteristic information to determine the numerical fluxes via the tracing of pseudo-control volumes. They are designed to monitor the average time evolution of the approximation to the solution within a complete grid cell rather than concentrating on the activity at the interfaces.

Straightforward application of the above techniques to general non-uniform velocity fields, that occur in heterogeneous media for example, does not guarantee positive solutions. Also, the formulation of the schemes is closely related to the uniform structure of the grid which require further consideration in taking them into general unstructured grids.

Skew Upstream Differencing Scheme

The early developments of multi-dimensional schemes date back to the 1970's with Raithby [132] who proposed the Skew Upstream Differencing Scheme (SUD) as an alternative to the conventional upstream difference scheme, in order to reduce false diffusion errors in the region of flow where the computational grid coordinate line and flow streamlines are not closely aligned. The benefits of the scheme have been shown using numerical results for uniform flows and for a non uniform rotational velocity field on a Cartesian grid. The scheme was formulated with a finite difference technique and it formed the basis for subsequent developments.

CVFEM Skew Upwind

In the control volume finite element (CVFEM) context, Schneider and Raw [147] proposed an upwind procedure that accounts for the directionality of the flow field through a skewed approach, while simultaneously precluding the possibility of negative coefficients. The schemes were originally devised to solve the Navier Stokes equations. They recommended both nodal and integration point values in the approximation of the convected value at the integration point, in order to avoid negative coefficients, especially in a highly non-uniform flow field. The 2-D work was formulated with *bilinear* quadrilateral elements

and requires the inversion of 4x4 local matrices.
Although its 3-D extension appears straightforward, to perform inversion of 12x12 local elemental matrices may become prohibitively expensive, especially if a more cost-effective procedure could offer the same or comparable accuracy and stability. Local inversion is required when convection upwind variables include both integration point and nodal variables, since each integration point variable must be written explicitly in terms of nodal variables alone.

Optimal Linear Multidimensional Schemes

In 1992, Roe and Sidilkover [138] investigated the theory of optimal linear, positive schemes for constant-coefficient advection in two and three dimensions. The schemes were introduced as a single parameter family and were presented in a conservative form. They observed that the optimum schemes have much lower numerical diffusion, and permit larger time-steps. Quantitatively, the optimum scheme has about four times less dissipation than the dimensionally split scheme and allows stable time-steps that are greater by a factor two.
In order to derive the optimum oscillation free, constant coefficient schemes, the authors establish the residual formula, on Cartesian grids, that has the smallest possible truncation error and propose a quantification of the cross-wind diffusivity of the scheme following the work of Hirsch et al. [82, 83]. The optimum linear scheme, referred to as the "N-scheme" - where N stands for narrow - uses a linear interpolation in the upwind triangle forming the cell and depends on narrow three node stencil in two dimensions. As shown by Roe and Sidilkover who gave its name, it is identical to the upwind scheme of Rice and Schnipke [134] on regular quadrilateral grids, provided that the latter are triangulated using the optimal choice for diagonals. Further details are presented in chapter 6, section 6.2.3.

Corner transport Upwind CTU scheme

The Corner Transport scheme introduced by Collela [36] uses a bilinear interpolation on the cell as a first step to building a second order multidimensional scheme. The scheme uses corner point data in order to enhance the stability of the upwind approximations.
In the same paper, explicit second-order time-dependent Godunov-type methods have been derived in two space variables by using the wave propagation properties for mul-

tidimensional hyperbolic equations and by limiting some of the second-order terms to suppress oscillations. The algorithm coincides with the multidimensional upwind method for hyperbolic conservation laws independently developed by van Leer [159] for the advection equation. However, unlike van Leer's algorithm, the extension to systems is based on a two step predictor corrector formalism on structured quadrilateral grids. Comparisons with second-order operator split methods have been established for gas dynamics applications on rectangular grids.

Residual distribution schemes

Another approach towards the construction of genuinely two dimensional upwind advection schemes are the fluctuation (or residual) distribution schemes, which have been developed in the last decade [141, 9, 6, 7, 10, 133, 88].
A review of fluctuations distribution methods is given in [155, 41].
These methods were originally developed for the scalar advection equations on triangular meshes in the steady state [139]. Extensions to these methods to systems and unsteady flows has followed due to the work of Abgrall and Barth [7] and more recently the work of Ricchuito [133]. For the approximation of steady state flows on unstructured triangular grids, these methods have reached a degree of maturity whereby the multidimensional schemes reproduce most of the advantages of upwind schemes in one dimension: second order approximation of smooth solutions, satisfying a discrete maximum principle in the presence of discontinuities, and rapid convergence to the steady state without the necessity for additional artificial viscosity. A distinctive and attractive feature of these schemes is that they are computationally compact.
They can be written as loops over elements and when processing an element no reference is made to data outside that element. This makes the methods efficient for parallelisation. Extensions to quadrilateral meshes of the residual distribution methods has been proposed by Abgrall [8].
Unfortunately, most of the upwind distribution schemes developed for steady state problems are only first order accurate for time dependent flows. Also, these schemes use average velocities over the elements and the generalisation to nonlinear fluxes requires special treatment. In addition, the schemes are not formulated in a locally conservative framework when applied to unsteady nonlinear hyperbolic problems on unstructured grids.

3.3.2 Recent developments of Multi-D schemes in Reservoir Simulation

Positive multidimensional upwind schemes for multi-phase flow transport equations is an active area of research in reservoir simulation. A two parameter family of wave oriented upwind schemes is presented by Edwards [54] on uniform quadrilateral grids. The formulation of the schemes was given in a locally conservative finite volume framework and formed the basis of the developments herein (chapters 6-10). Like the CTU scheme, the scheme uses the corner point and uses characteristic tracing. The scheme uses a nine point stencil instead of a five point stencil (as in SPU), and is based on a bilinear interpolation of the saturation on the quadrilateral grid cell. In the same paper, positivity analysis was conducted for linear advection on Cartesian grids and a generalisation to non-linear fluxes was also proposed. The schemes are coupled with a consistent CVD (MPFA) Darcy flow approximation and are identical to the N-scheme for the linear advection equation on a Cartesian grid. The stability and benefits of these schemes were shown through numerical cases involving full tensor permeability fields and high mobility ratios for two-phase flow systems.

Extension of this work to unstructured quadrilateral and triangular grids is presented in [107, 102] using an edge-based formulation and [101] using a cell-based formulation. A complete description is given in this thesis.

The CVFEM approach has also been adopted in reservoir simulation by Kozdon et al. [100] for simulating adverse mobility ratio displacements in for miscible gas injection into homogeneous and heterogeneous porous media on Cartesian grids. The approximation of the advection transport equation was also coupled with the MPFA method on Cartesian grids. An IMPEC strategy (implicit pressure, explicit concentration) was used in order to solve the coupled system of equations. In the same paper, the authors introduced the Flat scheme that provides minimal constant diffusion at the cross-wind diffusion at the expense of adding extra transverse diffusion in comparison with the optimal multidimensional scheme on Cartesian meshes for linear advection.

3.4 Flux-Continuous Finite-Volume Schemes

Rapid variation in permeability is common in oil reservoirs where permeability coefficients can jump by several orders of magnitude. Continuity of normal flux and pressure

at local physical interfaces between grid blocks with strong discontinuities in permeability are fundamental laws that must be built into the discrete approximation of the pressure equation.

Flux-continuous finite volume methods (FVM) [61, 2, 60, 161, 3, 62, 4, 53, 1, 122, 63] have been developed for mass-conservative approximations to the pressure and Darcy velocity of the fluid. Locally conservative flux-continuous full-tensor finite-volume schemes have been developed for the essentially elliptic component of the reservoir simulation system. These schemes are control-volume distributed (CVD) MPFA where flow variables and rock properties are assigned to the control-volumes of the grid and provide a consistent discretization of the porous medium pressure equation applicable to general geometry and permeability tensors on structured and unstructured grids.

In this work the higher resolution convection schemes are coupled with existing continuous Darcy-flux CVD approximations. Details of these schemes are presented in chapter 4, section 4.2.1.

Chapter 4

Numerical Discretisations

Numerical methods are necessary for the discretisation of reservoir simulation equations due to the complexity of the permeability and geometry of petroleum reservoirs as well as the non-linearity and coupling involved. In this chapter, the focus is on the formulation of state of the art finite volume methods for reservoir simulation. Section 4.1 includes a brief description of the finite volume method. Control volume cell vertex approximations are introduced in section 4.2 and are applied to the pressure and hyperbolic equations for multi-phase flow. Edge based and cell based formulations are considered for discretising the hyperbolic conservation form. Important distinctions between the formulations will be highlighted in the subsections 4.2.2 and 4.2.3 as well as in chapter 9. Solution strategy and time discretisation techniques are also discussed in this section. Finally, an overview of the discrete maximum principles for the hyperbolic equation is presented in 4.3.

4.1 Finite Volume Methods

The finite volume methods (FVM) are related to the original integral equations, and are derived from conservation of physical quantities over cell volumes. Fundamental to FVM is the introduction of control-volume cell average. Godunov [74] pursued this interpretation in the discretisation of the gas dynamics equations where the discrete solution has a piecewise constant representation in each control-volume defined by the cell average value. The finite volume form is suitable for discontinuity capturing and has been used in obtaining solutions to nonlinear hyperbolic conservations laws [110, 111, 76, 112, 113]. When compared to other discretisation methods such as finite differences or finite ele-

ments, the primary attraction of finite volume methods is numerical robustness by enforcing a ***discrete maximum principle***, applicability to ***general unstructured meshes*** and the intrinsic ***local conservation*** properties of the resulting schemes [93, 89, 164, 17] as the flux entering a given control volume is identical to that leaving the adjacent control volume.

4.1.1 Integral Forms for Multi-phase Flow

The integral form of the flow equations is given, as the first step of the finite volume discretisation. After integrating over a control volume Ω_{cv} with surface $\partial\Omega_{cv}$ via the Gauss divergence theorem, the continuity equations for phases $p = 1, N_p$ are written as

$$\int_{\Omega_{cv}} \frac{\partial S_p}{\partial t} d\Omega + \oint_{\partial\Omega_{cv}} \mathbf{V}_p \cdot \hat{\mathbf{n}} ds = m_p \tag{4.1.1}$$

where the integral is taken over the control volume Ω_{cv}, $\hat{\mathbf{n}}$ is the outward unit normal vector to the surface, $\partial\Omega_{cv}$, bounding the control volume Ω_{cv} and where S_p, $\mathbf{V}_p$ and m_p are the p^{th} phase saturation, Darcy velocity and specified phase flow rate respectively. Since the pore volume must always be filled by the fluids present, this gives rise to the volume balance where saturations sum to unity. Neumann boundary conditions apply on solid walls with zero normal flux. Inflow-outflow conditions apply at wells where fluxes/pressures are prescribed. Initial data in terms of saturation and pressure fields are also prescribed [13]. Without loss of generality with respect to the numerical schemes presented here, gravity and dispersion effects will be neglected in this chapter and will be treated in chapter 8.

4.1.2 Finite Volume Formulation

In its most simple setting the steps involved in devising a finite volume approximation for a system of conservation laws in integral form are the following [6]:

1. Decompose the domain in non-overlapping cells referred to as finite volumes or control volumes, over which the discrete solution is defined by its cell averages.

2. Evaluate the numerical fluxes through the boundaries of the control volume. This numerical flux is computed by means of a numerical flux function, with the two solution states at the interface as arguments, either given by the cell average itself or by a suitable reconstruction involving neighbouring cell averages.

3. Use the computed flux balance for each finite volume to evolve the cell averages in time by means of a suitable time integration scheme.

Finite volume methods are developed such that a close relationship to the physics of the underlying conservation law is maintained, aiming to capture as much as possible of the important properties of the weak solution. In its most sophisticated form in one dimension, the nonlinear physics of the conservation law is included by applying the flux function derived from the exact solution of the 1D Riemann problem associated with the two adjacent states [94, 74, 140].

4.1.3 Gridding and Unstructured Meshes in Reservoir Simulation

The simulation of fluid flow in petroleum reservoirs is performed by discretising the actual domain into a number of sub-domains or grid blocks and locally approximating the conservation law for each fluid component in the system via a finite volume scheme. Although the actual physical processes are independent of discretisation of the domain, the outcome of any flow simulation depends on the grid geometry and the discretisation scheme.

While it is still common in the practice of petroleum reservoir simulation to use Cartesian grids, development and use of general grid methods is emerging increasingly in the literature. The theory, implementation and application of unstructured grids has been extensively discussed in literature since the late 1980's. Heinemann and Brand [79] were the first to introduce Voronoi type grids to petroleum engineering naming them PeBi (Perpendicular Bisector) grids. Later, several researchers contributed to the development of unstructured grids, Heinemann [80], Palagi [125, 126], Verma and Aziz [163], Fung et al. [71] among others. Use of all elements in 3-D is presented in [122]. Here the focus is on 2-D elements.

In general, unstructured gridding in 2D is a spatial discretisation that consists of polygons, which locally vary in shape and size [162]. The use of unstructured grids provide a flexible framework that enables more accurate and detailed representation of complex geologic features. In many cases, the methodology of unstructured grid facilitates the modelling of different geometries and enhances the accuracy of the solution with comparison to Cartesian grids [163].

Control Volumes

Schemes which use the cells of the mesh as control volumes are called *cell centered* schemes. *Vertex centered* schemes on the other hand, use mesh duals as control volumes where control volumes are formed by joining cell centers to cell edge midpoints for all cells sharing common nodes as a geometric dual to the primal grid cells and flow solution unknowns and rock properties are stored on a per cell vertex basis. In this work, a vertex centered finite volume approximation is used. Control volume tessellation is flexible in the finite volume method. Edges and faces about the central vertex are shown in Figure 4.1 for duals formed from median segments or centroid segments among others. These geometric duals arise naturally for two dimensional finite-volume schemes. The dual cells or polygons serve as control volumes with the solution unknowns (degrees of freedom) stored on a per vertex basis with cell-wise assembly.

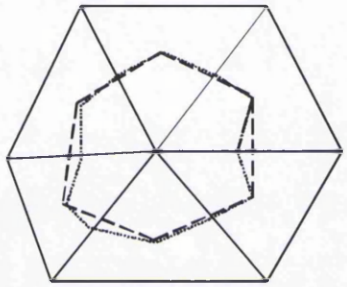

Figure 4.1: Triangulation duals: median (dashed), centroid (dotted).

4.2 Cell Vertex Finite volume Approximations

4.2.1 Flux Continuous Control Volume Distributed (CVD) Approximations

The main focus of this subsection is on the families of flux-continuous, locally conservative, control-volume distributed (CVD) finite volume schemes and the discretisation issues related to these schemes.

In reservoir simulation flow variables and rock variables are assigned to control-volumes so that they are control-volume distributed (CVD). Unstructured CVD multi-point flux approximations CVD (MPFA) are presented in [163, 4, 52, 53]. The formulation presented

here follows [52]. In this formulation flow and rock variables are vertex centered, i.e. distributed to the cell-vertex polygonal control-volumes, which are defined with respect to a given grid vertex by the contour constructed by connecting cell-edge mid-points to cell centres, for all cells sharing the common vertex.

The finite volume formulation is derived from the integral form of the flow equations (4.1.1). A unique discrete flux is then constructed for each control-volume sub-face and the closed integral of flux approximated by the sum of the discrete outward normal fluxes. The fluxes are constructed in a cell-wise assembly process, for a triangular cell there are three subcell fluxes, F_a, F_b, F_c, Figure 4.2. The subcell fluxes are accumulated with re-

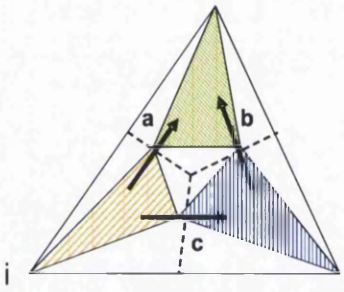

Figure 4.2: Sub-cell flux basis (dashed triangles).

spect to their triangle cell edges within an assembly process. The edge index $e(i,j)$ refers to the j^{th} edge attached to vertex i. The net edge based single phase flux $F_{e(i,j)}(\phi)$ associated with edge $e(i,j)$ is comprised of the sum of adjacent sub-cell fluxes that belong to the primal grid cells with common edge $e(i,j)$. In the domain interior two adjacent sub-cell fluxes are assembled for each cell edge, with reference to vertex i and local edge e of Figure 4.3(a) and the local fluxes of Figure 4.3(c), the net edge based flux is given by

$$F_{e(i,j)} = F_{a_1} + F_{b_2}. \tag{4.2.1}$$

Control-Volume Flux and Continuity

Here, flow variables are assigned to grid vertices and rock properties are piecewise constant with respect to the control-volumes. A consistent normal flux approximation is constructed for the three fluxes that respect the physical constraints of continuity of pressure and flux across the control-volume interfaces separating different permeability

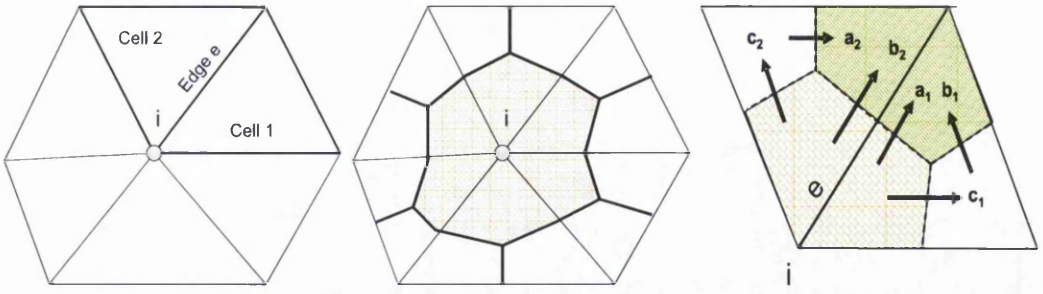

(a) (b) (c)

Figure 4.3: (a) Segment of primal grid; (b) control-volume; (c) dual grid (bold) and fluxes in cells sharing the edge e.

values within each primal grid cell.

Referring to the triangular cell, the locally numbered vertices have pressures

$$\mathbf{\Phi}_v = (\phi_1, \phi_2, \phi_3).$$

Three continuous interface pressures

$$\mathbf{\Phi}_f = (\phi_a, \phi_b, \phi_c)$$

are introduced at points (a, b, c) on the control-volume sub-faces, Figure 4.2. Subcell triangular basis functions are then formed by joining each cell-vertex to the two adjacent interface points. The pressure field now assumes a piecewise linear variation over each subcell triangle as shown in Figure 4.3. Consequently approximations of the derivatives ϕ_ξ, ϕ_η are linear functions of $\mathbf{\Phi}_f$ and $\mathbf{\Phi}_v$. A piecewise constant gradient is then formed over each subcell triangle and is used in turn to define local piecewise constant Darcy fluxes. The general tensor T defined by the Piola transformation is formed locally by resolving physical full-tensor fluxes with respect to the subcell geometry and control-volume permeability. Three flux continuity conditions are imposed within each triangle and are expressed as

$$\begin{aligned} F_A &= -(T_{12}\phi_\xi + T_{22}\phi_\eta)|_A^1 = -(T_{11}\phi_\xi + T_{12}\phi_\eta)|_A^3, \\ F_B &= -(T_{11}\phi_\xi + T_{12}\phi_\eta)|_B^1 = -(T_{11}\phi_\xi + T_{12}\phi_\eta)|_B^2, \\ F_C &= -(T_{12}\phi_\xi + T_{22}\phi_\eta)|_C^2 = -(T_{12}\phi_\xi + T_{22}\phi_\eta)|_C^3, \end{aligned} \tag{4.2.2}$$

where (ξ, η) is a local dimensionless coordinate system in each subcell. Here $\Gamma\,|_{\sigma}^{j}$ denotes interface flux Γ at location σ and state of volume j. The actual position of σ along each subcell face defines both the point of continuous pressure and the flux quadrature (Figure 4.3(c)), and in turn leads to a family of unstructured schemes [52, 53, 124].

The system of Equations (4.2.2) is rearranged into the form

$$\mathbf{F} = A_L \Phi_f + B_L \Phi_v = A_R \Phi_f + B_R \Phi_v, \tag{4.2.3}$$

and thus the interface pressures can be expressed *locally* in terms of the cell vertex pressures. After elimination of the Φ_f from Equation (4.2.3) it follows that

$$\mathbf{F} = (A_L(A_L - A_R)^{-1}(B_R - B_L) + B_L)\Phi_v. \tag{4.2.4}$$

The fluxes of Equation (4.2.4) can also be written as a linear combination of cell edge potential differences [53], demonstrating the consistency condition that flux is zero for constant potential and each component of flux takes the form

$$F_\sigma(\phi) = -\sum_{j=1}^{NedC} \alpha_j^\sigma \Delta_j \phi \tag{4.2.5}$$

where $NedC$ is the number edges of the primal grid cell. The effect of quadrature point upon accuracy and convergence is explored in [124].

The closed surface integral of phase velocity can now be expressed as the sum of outward normal phase fluxes F_{p_i} over each of the surface increments of the control-volume Ω_{cv}, viz

$$\oint_{\partial\Omega_{cv}} \mathbf{V}_p \cdot \hat{\mathbf{n}} ds = \sum_{i=1}^{N_S} \mathrm{F}_{p_i} \tag{4.2.6}$$

where N_S is the number of surface increments that enclose the volume Ω_{cv}. The outward normal phase flux in the i^{th} normal direction is written in terms of the general tensor $\mathbf{T}$ as

$$\mathrm{F}_{p_i} = -\int_{\partial\Omega_{cv}} \mathrm{f}_p \Lambda \sum_{j=1}^{2} T_{ij} \phi_{\xi_j} \mathrm{d}\Gamma_i \tag{4.2.7}$$

where ξ_i are local curvilinear parametric coordinates, Γ_i is the parametric coordinate surface increment and ϕ_{ξ_j} is the derivative of ϕ with respect to ξ_j and $\mathbf{T} = J\mathbf{J}^{-1}\mathbf{K}\mathbf{J}^{-T}$ is the general tensor defined via the Piola transformation which is a function of the Cartesian permeability tensor and geometry, where $J_{ij} = \partial x_i / \partial \xi_j$ is the Jacobian of the local curvilinear coordinate transformation, and $J = x_\xi y_\eta - y_\xi x_\eta$ is the Jacobian

determinant. The actual approximation of the transmissibility tensor T naturally arises by normal resolution of Darcy flux across an interface [123]. The grids considered here generally give rise to non-zero cross terms with $T_{ij} \neq 0$ for $i \neq j$ in the general tensor. For incompressible flow, Equation (4.1.1) is summed over the N_p phases and using the sum of saturations is unity, yields the pressure equation

$$\sum_{i=1}^{N_S} \mathrm{F}_{T_i} = 0 \tag{4.2.8}$$

away from sources and sinks (or wells) where the total flux F_{T_i} involves a product of total mobility and single phase flow flux and is given by

$$\mathrm{F}_{T_i} = -\int_{\partial\Omega_{cv}} \Lambda \sum_{j=1}^{2} T_{ij}\phi_{\xi_j} \mathrm{d}\Gamma_i. \tag{4.2.9}$$

4.2.2 Edge Based Cell Vertex Multi-phase Flow Approximation

Consider the control volume corresponding to the node i Figure 4.3(b). Let N_{edV} be the total number of constitutive edges connected to vertex i and τ_i the i^{th} control-volume area. Define the control volume cell average as

$$\mathbf{S}_{p_i} = \frac{1}{\tau_i}\int_{\Omega_i} S_p d\Omega$$

for the p^{th} phase. The finite volume approximation of Equation (4.1.1) can be interpreted as producing an evolution equation for control volume averages

$$\frac{\partial}{\partial t}\int_{\Omega_i} S_p d\Omega = \tau_i \frac{d}{dt}\mathbf{S}_{p_i}.$$

The flux integral appearing in Equation (4.1.1) is approximated by

$$\oint_{\partial\Omega_{cv}} \mathbf{V}_p \cdot \hat{\mathbf{n}} ds = \sum_{j=1}^{N_{edV}} \mathrm{f}_p(\mathbf{S}_L^n, \mathbf{S}_R^n) F_{T_{e(i,j)}}(\phi^{n+1}). \tag{4.2.10}$$

for the p^{th} phase continuity equation, where $\mathbf{S}_L^n, \mathbf{S}_R^n$ are the left and right hand values of the phase saturation vectors with respect to edge $e(i,j)$ and n denotes the time level of the scheme. Here $F_{T_{e(i,j)}} = \Lambda F_{e(i,j)}(\phi)$, where $F_{e(i,j)}(\phi)$ is the single phase Darcy flux and M_{p_i} denotes the p^{th} phase flow rate, which is prescribed at wells and is zero otherwise.

The semi-discrete finite volume form of Equation (4.1.1) for multiphase flow on unstructured grids is then written as

$$\tau_i \frac{d}{dt}\mathbf{S}_{p_i} + \sum_{j=1}^{N_{edV}} \mathrm{f}_p(\mathbf{S}_L^n, \mathbf{S}_R^n) F_{T_{e(i,j)}}(\phi^{n+1}) = M_{p_i}, \tag{4.2.11}$$

The phase continuity equations are coupled through the discrete pressure equation

$$\sum_{j=1}^{N_{edV}} \Lambda(\mathbf{S}_L^n, \mathbf{S}_R^n) F_{e(i,j)}(\phi^{n+1}) = M_i, \tag{4.2.12}$$

which is obtained by summing Equation (4.2.11) over the phases and using the volume balance constraint. Equivalently Equation (4.2.12) can be expressed as

$$\sum_{e=1}^{N_{edV}} \sum_{q=1}^{N_q} F_{T_q} = M_i, \tag{4.2.13}$$

where i_q sums over the flux quadrature points (one per sub-face), $N_q = 1$ at boundaries (one subcell), $N_q = 2$ in the field where two subcell faces join at the edge midpoint

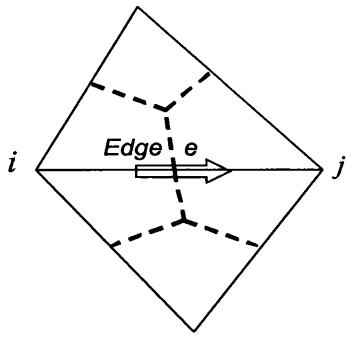

Figure 4.4: Left and Right convention.

4.2.3 Cell Based Cell Vertex Multi-phase Flow Approximation

In the absence of source terms, the cell based finite volume semi-discrete equation is written as:

$$\tau_i \frac{d}{dt} \mathbf{S}_{p_i} + \sum_{e=1}^{N_{edV}} \sum_{i_q=1}^{N_q} \mathrm{f}_p(\mathbf{S}_{L_q}^n, \mathbf{S}_{R_q}^n) F_{T_q} = M_{pi}, \tag{4.2.14}$$

for each phase p. The total Darcy-flux is computed from the pressure equation at a single quadrature point per subcell [53], here we evaluate the subcell flux on the control volume sub-face at the point of attachment to the cell edge e. Thus the quadrature points are chosen to coincide with the center of the cell edges.

4.2.4 Single Point Upstream Weighting Scheme

The approximate flux is defined according to the sign of the local wave direction w_p, evaluated here at the control volume sub-faces connected the edge e. Referring to Figure 4.4 with respect to a local frame of reference aligned with the direction i to j along the edge e, the standard reservoir simulation upwind scheme is written as

$$\mathrm{f}_p(\mathbf{S}_L^n, \mathbf{S}_R^n) = \begin{cases} f_p(\mathbf{S}_L^n) & w_p \geq 0 \\ f_p(\mathbf{S}_R^n) & w_p < 0 \end{cases} \tag{4.2.15}$$

and the first order upwind scheme, (known as single-point upstream weighting in the reservoir simulation literature [13]) is defined with $\mathbf{S}_L^n = \mathbf{S}_i^n$ and $\mathbf{S}_R^n = \mathbf{S}_j^n$.

Remark 4.2.1 *Note that the control volume cell based and edge based single-point upstream weighting formulations coincide on Cartesian meshes. This observation extends to unstructured grids in the case where the wave velocity at the quadrature points on each side of the cell edges are of the same sign.*

4.2.5 Solution strategy: Implicit Pressure Explicit Saturation (IMPES) Algorithm

In conventional compositional simulations either pressure is treated implicitly and the saturation variables are treated explicitly leading to implicit pressure explicit saturation (IMPES) algorithm [13, 21] or all variables are treated implicitly (Fully Implicit). In the first approach the time-step is restricted by the CFL condition and in the second approach the amount of work per time-step increases sharply as the number of components needed to describe the system increases. Here an IMPES formulation is adopted where pressure is the implicit variable, and the saturation and concentration variables are treated explicitly. This explicit treatment will reduce the number of unknowns we need to solve simultaneously.

The system of Equations (4.2.11) (Equations (4.2.14) respectively) and (4.2.12) are solved sequentially, Equation (4.2.12) is first solved implicitly for pressure while Equation (4.2.11) (Equation (4.2.14 respectively) is solved explicitly in this formulation. Fully implicit and semi-implicit formulations are presented in [57, 58].

4.2.6 Runge-Kutta Time Discretisation

A common strategy for explicit time integration of semi-discrete equations of the form in Equation (4.2.11) is to use Runge-Kutta (RK) methods. Here we have used the third order monotonicity preserving Runge-Kutta method proposed in [148]. Let $\mathfrak{L}$ denote the local discrete spatial approximation operator on the extended stencil and Δt be the local time step, which can vary from a time step to another. Writing Equation (4.2.11) (or Equation (4.2.14)) as

$$\frac{d}{dt}\mathbf{S}_{p_i} = \mathfrak{L}(\mathbf{S}_p),$$

the third order Runge-Kutta method is written as:

$$\begin{aligned}
\mathbf{S}_{p_i}^{(1)} &= \mathbf{S}_{p_i}^{n} + \Delta t \mathfrak{L}(\mathbf{S}_p^{n}), \\
\mathbf{S}_{p_i}^{(2)} &= \tfrac{3}{4}\mathbf{S}_{p_i}^{n} + \tfrac{1}{4}\mathfrak{L}(\mathbf{S}_p^{(1)}) + \tfrac{1}{4}\Delta t \mathfrak{L}(\mathbf{S}_p^{(1)}), \\
\mathbf{S}_{p_i}^{n+1} &= \tfrac{1}{3}\mathbf{S}_{p_i}^{n} + \tfrac{2}{3}\mathfrak{L}(\mathbf{S}_p^{(2)}) + \tfrac{2}{3}\Delta t \mathfrak{L}(\mathbf{S}_p^{(2)}).
\end{aligned}$$

Comparisons between numerical simulations using third order Runge-Kutta discretisation and forward Euler time stepping have indicated little difference in results. Consequently, the more efficient forward euler method is used for time integration unless stated otherwise.

Therefore, the edge based vertex centered finite volume discretisation of Equation (4.2.11) for multi-phase flow on unstructured grids now takes the form [57]:

$$(\mathbf{S}_{p_i}^{n+1} - \mathbf{S}_{p_i}^{n})\tau_i + \Delta t \sum_{j=1}^{N_{edV}} \mathrm{f}_p(\mathbf{S}_L^{n}, \mathbf{S}_R^{n}) F_{T_{e(i,j)}}(\phi^{n+1}) = \Delta t M_{p_i}, \tag{4.2.16}$$

and the cell-based vertex centered finite volume discretisation of Equation (4.2.14) is written as:

$$(\mathbf{S}_{p_i}^{n+1} - \mathbf{S}_{p_i}^{n})\tau_i + \Delta t \sum_{e=1}^{N_{edV}} \sum_{i_q=1}^{N_q} \mathrm{f}(\mathbf{S}_{L_q}^{n}, \mathbf{S}_{R_q}^{n}) F_{T_q}(\phi^{n+1}) = \Delta t M_{p_i}. \tag{4.2.17}$$

4.3 Local Discrete Maximum Principles for the hyperbolic equation

Discrete maximum principle analysis plays a central role in the design and analysis of finite volume schemes suitable for non-oscillatory discontinuity capturing schemes. A systematic analysis of the conditions required by a scheme to satisfy these requirements

was given by Godunov [74] who introduced the concept of *monotonicity.* There is an extensive literature on this very important topic and many definitions and criteria can be found [38, 130]. Bounded total variation motivated the development of *total variation diminishing* (TVD) schemes, introduced by Harten [76] as a general concept to ensure that unwanted spurious oscillations are not generated by a numerical scheme. Spekreijse [153] expressed monotonicity as a positivity condition. More recent general analysis has been developed by Jameson [91] based on the definition of *local extrema diminishing* (LED) schemes. In this section we present a review of different formulations of *discrete maximum principles* following Barth [15].

4.3.1 One Dimensional Non Linear Scalar Conservation Laws

In this section we examine discrete total variation and maximum principles for scalar conservation laws. Consider the nonlinear conservation law:

$$S_t + (f(S))_x = 0; \tag{4.3.1}$$

subject to the initial condition:

$$S(x,0) = S_0(x). \tag{4.3.2}$$

Equation (4.3.1) is discretised in the conservation form:

$$S_j^{n+1} = S_j^n - \frac{\Delta t}{\Delta x}(\mathrm{f}_{j+1/2} - \mathrm{f}_{j-1/2}) \tag{4.3.3}$$

where $\mathrm{f}_{j+1/2}$ is a consistent numerical flux i.e. $\mathrm{f}_{j+1/2} = H(S_{j-l+1}, .., S_{j+l})$ and $H(S, .., S) = f(S)$.
We shall first define the monotonic data and total variations.

Definition 4.3.1 ***Monotonic Data.*** *A grid function S is called* monotone *if for all i, if*

$$\min(S_{i-1}, S_{i+1}) \leq S_i \leq \max(S_{i-1}, S_{i+1}). \tag{4.3.4}$$

Definition 4.3.2 ***Total variation.*** *Define the total variation in one dimension:*

$$TV(S) = \sum_{-\infty}^{\infty} \mid S_i - S_{i-1} \mid . \tag{4.3.5}$$

According to Lax [111],

"the total increasing and decreasing variations of a differentiable solution between any pair of characteristics is conserved."

Furthermore, in the presence of shock wave discontinuities, information is lost and the total variation decreases.

Strong Monotonicity HHL

A finite difference scheme Equation (4.3.3) is said to be *monotone* in the sense of Harten, Hyman and Lax [78] if H is a monotone increasing function of each of its arguments with

$$\frac{\partial H}{\partial S_i}(S_{-k}, .., Sk) \geq 0, \forall -k \leq i \leq k. \tag{4.3.6}$$

This is a strong definition of *monotonicity.* In [78], it is proven that schemes satisfying this condition also satisfy the entropy inequality which distinguishes the physically relevant discontinuities. Unfortunately, they also prove that HHL monotone schemes in conservation form are at most first order spatially accurate.

Weak Monotonicity: Monotonicity Preserving Schemes

To allow higher order accuracy, Harten [76] introduced a weaker concept of monotonicity. A numerical scheme is called *monotonicity preserving* if monotonicity of S^{n+1} follows from the monotonicity of S^n.
It follows immediately from the definition of monotonicity preservation that

- local maxima are non-increasing, and
- local minima are non-decreasing;

which is a property of the conservation law equation. VanLeer [160] interpreted the monotonicity preserving condition using geometric considerations.

Total Variation Diminishing (TVD)

Harten [76] introduced the notion of total variation diminishing schemes using a weaker form of monotonicity than the monotonicity preserving criteria. The total variation measures the total amount of oscillations in the function. A scheme is said to be total variation diminishing (TVD) if

$$TV(S^{n+1}) \leq TV(S^n). \tag{4.3.7}$$

Harten has proven that schemes which are HHL monotone are TVD and schemes that are TVD are monotonicity preserving. Furthermore, it can be shown that all linear monotonicity preserving schemes (i.e. the coefficients of the discrete form are independent of S) are at most first order accurate. Thus high order accurate TVD schemes must necessarily be nonlinear with solution dependent coefficients.

4.3.2 Discrete Maximum Principles on Unstructured Meshes

Monotonicity concept is restricted to one dimensional data. Here, a review of different positivity criteria for hyperbolic conservation laws in higher dimensions is presented. Consider the Cauchy initial value problem (ivp) on a closed domain Ω:

$$\begin{aligned} S_t + \nabla \cdot \mathfrak{F}(S) &= 0, \text{ in } \Omega; \\ S(\mathbf{x}, 0) &= S_0(\mathbf{x}), \text{ in } \partial\Omega, \end{aligned} \tag{4.3.8}$$

where $\mathfrak{F}(S)$ denotes the flux function. Then, the semi discrete finite volume scheme Equation (4.2.11) for each control volume $\Omega_j \in \Omega$ is written as:

$$\frac{d}{dt} S_j + \frac{1}{\tau_j} \sum_{e(j,k) \in \partial\Omega_j} f_{jk}(S_{Le}, S_{Re}) = 0, \tag{4.3.9}$$

where τ_j is the control volume area, f_{jk} is the discrete numerical flux at the center of the edge $e(j,k)$, which is a function of the left and right states S_{Le} and S_{Re}.

Entropy Satisfying Schemes and Monotonicity

In order to guarantee convergence to entropy satisfying weak solutions, we choose the flux to be **monotone** or an **E-flux** [15]. Monotone fluxes include Godunov flux defined as

$$f^G(S_L, S_R) = \begin{cases} \min_{S \in [S_L, S_R]} \mathrm{f}(S) & S_L \leq S_R \\ \max_{S \in [S_R, S_L]} \mathrm{f}(S) & S_R \leq S_L \end{cases} \tag{4.3.10}$$

that relies on flux functions that are strictly convex, and the Local Lax Friedrichs (LLF) flux defined as

$$f^{LF}(S_L, S_R) = \frac{1}{2}(\mathrm{f}(S_L) + \mathrm{f}(S_R)) - \frac{1}{2} \sup_{S \in [S_L, S_R]} |\mathrm{f}'(S)|(S_R - S_L), \tag{4.3.11}$$

that involves the derivatives of the flux function [117].

E-fluxes were introduced by Osher [121]. The most prominent E-flux is the Enquist-Osher (EO) flux written as:

$$f_p^{EO}(S_L, S_R) = \frac{1}{2}(\mathrm{f}(S_L) + \mathrm{f}(S_R)) - \frac{1}{2}\int_{S_L}^{S_R} |\mathrm{f}'(S)| dS. \tag{4.3.12}$$

Further details on alternative numerical fluxes can be found in Godlewski and Raviart [73] and Leveque [113]. A compelling motivation for the use of monotone fluxes in the finite volume scheme Equations (4.3.9) is the obtention of discrete maximum principles in the resulting numerical solutions of nonlinear conservation laws. A standard analysis technique is to first construct local maximum principles which can then be applied successfully to obtain global maximum principles and stability results. The first result concerns the boundedness of local extrema in time for semi-discrete finite volume schemes that can be written in nonnegative coefficient form.

LED Property

The semi discrete scheme for each control volume Ω_j,

$$\frac{d}{dt}S_j = \frac{1}{\tau_j}\sum_{e(j,k)\in\partial\Omega_j} C_{jk}(S_h)(S_k - S_j), \tag{4.3.13}$$

where the right hand side involves the sum over all nodes connected to node j, is *local extremum diminishing* (LED) [91], i.e. local maxima are decreasing and local minima are nondecreasing **if**

$$C_{jk}(S_h) \geq 0 \text{ , for every } e(j,k) \in \partial\Omega_j.$$

Here $S_h(t)$ denotes a piecewise polynomial solution representation in space on each control volume such that

$$S_j(t) = \frac{1}{\tau_j}\int_{\Omega_j} S_h(x,t)dx, \tag{4.3.14}$$

and

$$C_{jk} = -\frac{f_{jk}(S_k, S_j) - \mathfrak{F}(S_j)\cdot\hat{\mathbf{n}}_{jk}}{S_k - S_j}, \tag{4.3.15}$$

where $\hat{\mathbf{n}}_{jk}$ is the weighted outward normal to the edge e_{jk}. Note here that by construction

$$\sum_{e(j,k)\in\partial\Omega_j} \mathfrak{F}(S_j)\cdot\hat{\mathbf{n}}_{jk} = 0.$$

Local Space-Time Discrete Maximum Principle

The fully discrete scheme for the time slab increment $[t^n, t^{n+1}]$ and each $\Omega_j \in \Omega$

$$S_j^{n+1} = S_j^n + \frac{\Delta t}{\tau_j} \sum_{e(j,k)\in\partial\Omega_j} C_{jk}(S_h)(S_k - S_j),$$

exhibits a local space-time discrete maximum principle

$$\min_{e(j,k)\in\partial\Omega_j} (S_j^n, S_k^n) \leq S_j^{n+1} \leq \max_{e(j,k)\in\partial\Omega_j} (S_k^n, S_j^n), \tag{4.3.16}$$

if

$$C_{jk}(S_h) \geq 0 \text{ , for every e(j,k)} \in \partial\Omega_j,$$

and satisfies the CFL-like condition

$$1 - \frac{\Delta t}{\tau_j} \sum_{e(j,k)\in\partial\Omega_j} C_{jk}(S_h) \geq 0, \text{ for every e(j,k)} \in \partial\Omega_j.$$

A global L^∞-stability bound is then obtained for a scalar initial boundary condition problem Equation (4.3.8).

Positivity Criteria

Definition 4.3.3 *A scheme is said to be* **positive** *if the value of the solution at the new time-step can be written as the convex sum of the values at the previous time-step,*

$$S_j^{n+1} = \sum_k \alpha_k S_k^n, \text{ with } \alpha_k \geq 0, \forall k, \tag{4.3.17}$$

together with the consistency condition

$$\sum_k \alpha_k = 1. \tag{4.3.18}$$

This ensures that no new extrema are created, since

$$\min_k(S_k^n) \leq S_i \leq \max_k(S_k^n). \tag{4.3.19}$$

As recalled by Roe in [139], the concept of positivity was initially introduced by Godunov [74] for the one-dimensional linear advection equation. Spekreijse [153] extended the concept to two dimensions for structured grids and a great many others e.g. [16, 141, 115, 6] have used it as a convenient criterion for the design of non-oscillatory schemes on unstructured meshes.

Local Positivity

A more restrictive property, referred to as ***local positivity*** is obtained by considering the contribution from each grid element, taken separately, and demanding that the scheme be positive for each contribution [6]:

$$S_j^{n+1} = \sum_{\text{cell c}} \sum_{k \in c} \alpha_k^c S_k^n, \text{ with } \forall c, \forall k \in c, \alpha_k^c \geq 0. \tag{4.3.20}$$

It follows that if a scheme is locally positive, it will also be positive for the global update scheme.

Chapter 5

Higher Order Schemes on Unstructured Triangular Meshes

5.1 Introduction

In this chapter, higher resolution schemes are presented for convective flow approximation on distorted unstructured grids. This work continues with the development of the higher order unstructured grid schemes presented in [57, 58, 56]. The convection schemes are coupled with continuous Darcy fluxes for approximation of the pressure equation and applied to multi-phase flow problems. Extension of the higher order schemes to general unstructured grids is presented in section 5.2. An edge-based vertex-centered finite volume approximation is adopted here. Also, we refer to section 2.3.1 for the flow equations and to section 4.2.2 for details on the discretisation. A sequence of higher resolution non-uniform limiters are presented in 5.3. The schemes are tested on a range of highly distorted structured and unstructured grids with variable grid spacing. Two-phase flow results are presented in section 5.4 that demonstrate the advantages of the new higher order flux-continuous formulation. Conclusions follow in section 5.5.

5.2 Higher Order Reconstructions

A higher order unstructured grid approximation is now presented with respect to the saturation variables. This formulation follows [57] with higher order reconstruction applied to the saturation field and relates to the Local Extrema Diminishing LED schemes of [91], [118]. For the remainder of this section superfix n is omitted and it is understood

that all saturations are computed at level n.

The scheme is expressed as a two-step process. The procedure involves calculating higher order left and right hand side states relative to the mid-point of each edge e (along which flux is to be defined) by expansions about the edge vertices at i and k, Figure 5.1. As in one dimension [160], the expansions are constrained with slope limiters to ensure that the higher order data satisfies a local maximum principle, preventing the introduction of spurious extrema.

First we define the difference in $\mathbf{S}$ over the edge e as shown in Figure 5.1, as

$$\Delta \mathbf{S}_{ki} = \mathbf{S}_k - \mathbf{S}_i \tag{5.2.1}$$

where it is now understood that $\Delta \mathbf{S}$ with a double suffix denotes a difference in $\mathbf{S}$. Referring to Figure 5.1 the left and right states $\mathbf{S_L}$ and $\mathbf{S_R}$ at the midpoint of the *key* edge e (joining vertices i and k) are expressed as

$$\mathbf{S_L} = \mathbf{S}_i + \frac{1}{2}\Phi^+ \Delta \mathbf{S}_{ki} \tag{5.2.2}$$

where Φ^+ is a function of

$$\mathbf{r}^+_{ki} = (\Delta \mathbf{S}_{iu} / \Delta \mathbf{S}_{ki}) \tag{5.2.3}$$

and

$$\mathbf{S_R} = \mathbf{S}_k - \frac{1}{2}\Phi^- \Delta \mathbf{S}_{ki} \tag{5.2.4}$$

where Φ^- is a function of

$$\mathbf{r}^-_{ki} = (\Delta \mathbf{S}_{dk} / \Delta \mathbf{S}_{ki}) \tag{5.2.5}$$

Extension to unstructured grids requires special construction of the differences $\Delta \mathbf{S}_{iu}$ and $\Delta \mathbf{S}_{dk}$. Directional differences are constructed by extrapolating along the *key* edge defined by vector $\Delta \mathbf{r}_{ki}$ in the respective upstream and downstream directions, see arrows in Figure 5.1. Extrapolation of the respective upstream and downstream data is constrained such that a local maximum principle is imposed. The upstream triangle $i, 1, 2$ is labelled T_U and the downstream triangle $k, 3, 4$ is labelled T_D. The space vector corresponding to edge e ($\Delta \mathbf{r}_{ki}$) is extrapolated into the respective triangles T_U, T_D, see arrows in Figure 5.1. This is illustrated further with respect to vertex i. The edge vector is extrapolated

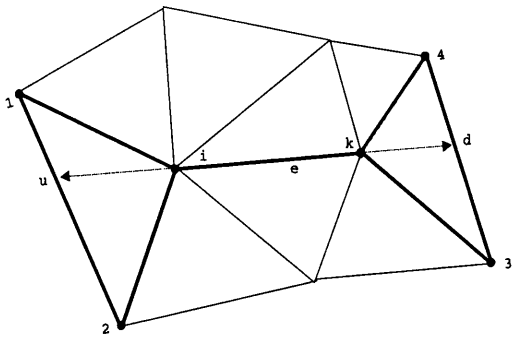

(a)

Figure 5.1: Higher Order Support.

to the point of intersection u, on the opposite edge of the triangle T_U, Figure 5.1. The *upwind* difference is equal to the convex average of triangle edge differences with

$$\Delta \mathbf{S}_{iu} = (1 - \xi)\Delta \mathbf{S}_{i1} + \xi \Delta \mathbf{S}_{i2} \tag{5.2.6}$$

where $1 - \xi \geq 0$ and $\xi \geq 0$ is the ratio of area of sub-triangle $i, 1, u$ to area of triangle T_U. In order to impose a maximum principle with respect to T_U and edge e, the limiter Φ^+ is defined so as to bound the higher order gradient approximation between the slopes on triangle edges $i1$ and $i2$ and slope of edge e. The limiter is defined by

$$\Phi^+ = \Phi(r_{ki}^+) \tag{5.2.7}$$

where r_{ki}^+ is defined by Equation (5.2.3) and $\Phi(r)$ can be any classical slope limiter [160] and [156]. The higher order reconstruction is then bounded between $\mathbf{S}_k$ and $\mathbf{S}_u$, which by convexity (Equation (5.2.6)), ensures that the bounds are such that

$$\min_{T_U \cup e}\{\mathbf{S}\} \leq \mathbf{S_L} \leq \max_{T_U \cup e}\{\mathbf{S}\} \tag{5.2.8}$$

over triangle T_U and edge e yielding a local maximum principle with reconstruction reducing to first order locally at two dimensional extrema.

In cases where coincidence or near coincidence is detected between the extrapolated edge and an upwind triangle edge the limiting is collapsed to be entirely edge based. A similar convex average interpolant is constructed for vertex k using the right hand bold triangle together with analogous limiter bounds that now depend on $\Phi(r_{ki}^-)$ and the edge slopes $\Delta \mathbf{S}_{ki}$, $\Delta \mathbf{S}_{3k}$ and $\Delta \mathbf{S}_{4k}$.

This completes the definition of the higher order states. The second step of the scheme uses the upwind flux where each higher order approximation of phase saturation is upwinded according to the direction of the phase wave speed, using Equations (5.2.2), (5.2.4) in Equation (4.2.15).
Here, while limiting is based on the van-Leer (Fromm) limiter

$$\Phi(r) = \max(0, \min(2r, 2, \frac{1+r}{2})) \tag{5.2.9}$$

where r is the ratio of neighbouring differences in solution, modifications for mesh distortion are considered below. Further details on limiters are presented in [156].
Three dimensional extensions of this scheme are presented in [58, 56]. In this work we consider possible extensions of the above schemes for arbitrary unstructured grid distortions.

5.3 Limiters on Non-Uniform Meshes

For application to non-uniform distorted meshes we require that gradients and limiters are modified according to mesh irregularity and non-uniformity. In this section, we introduce a sequence of possible limiters which take into account the irregularity of the grid.
On a non-uniform grid, the linear reconstruction is illustrated for the left hand state and expressed as

$$\mathbf{S_L} = \mathbf{S}_i + \frac{1}{2}\Phi^+ \nabla \mathbf{S}_i \cdot \Delta \mathbf{r}_{ki} \tag{5.3.1}$$

where $\nabla \mathbf{S}_i \cdot \Delta \mathbf{r}_{ki} = \Delta \mathbf{S}_{ki}$ denotes the constructed gradient defined with respect to node i. The van-Leer MUSCL constraints on a non-uniform (cell-vertex) grid require that

$$\mathbf{S}_i + \frac{1}{2}\Phi^+ \nabla \mathbf{S}_i \cdot \Delta \mathbf{r}_{ki} \leq \mathbf{S}_u \tag{5.3.2}$$

$$\mathbf{S}_i - \frac{1}{2}\Phi^+ \nabla \mathbf{S}_i \cdot \Delta \mathbf{r}_{iu} \geq \mathbf{S}_d \tag{5.3.3}$$

The inequalities of Equation (5.3.2) lead to the limiter upper bounds $\Phi^+ \leq \min(2, 2r^+_{ki})$ where r^+_{ki} is a non-uniform grid limiter ratio defined by

$$r^+_{ki} = \frac{\Delta \mathbf{S}_{iu}/\Delta r_{iu}}{\Delta \mathbf{S}_{ki}/\Delta r_{ki}}. \tag{5.3.4}$$

In this work the ratio of divided differences corresponds to the ratio of average gradients on the triangle T_U and on the edge e respectively. Possible non-uniform grid limiters are proposed below for defining Φ^+ in Equation (5.3.1). Here it is understood that when defining Φ^+ then $r = r_{ki}^+$ and an analogous definition is used for Φ^-.

A common procedure to approximate the gradient is to use a least square fit to the solution using the neighboring cells [15]. A least square fit of gradients at node i using the gradients on T_U and on the edge e is considered. The limiter in Equations (5.2.9) and (5.3.1) takes the form

$$\Phi_{LS}(r) = \max(0, \min(2r, 2, \frac{\Delta r_{iu}^2 + \Delta r_{ki}^2 r}{\Delta r_{iu}^2 + \Delta r_{ki}^2})). \tag{5.3.5}$$

A second order accurate gradient approximation on a non uniform mesh derived via Taylor series analysis is written as a linear combination of the adjacent gradients with weights proportional to local grid spacing ratios. The corresponding limiter is written as

$$\Phi_{TS}(r) = \max(0, \min(2r, 2, \frac{\Delta r_{iu} + \Delta r_{ki} r}{\Delta r_{iu} + \Delta r_{ki}})). \tag{5.3.6}$$

The Green-Gauss approximation [15] gives the limiter

$$\Phi_G(r) = \max(0, \min(2r, 2, \frac{\Delta r_{ki} + \Delta r_{iu} r}{\Delta r_{iu} + \Delta r_{ki}})). \tag{5.3.7}$$

Note that all the limiters introduced above are equivalent to the original Fromm limiter described by Equation (5.2.9) when the grid is uniform.

Finally, in an attempt to improve the accuracy of the solution we introduce a weighted limiter

$$\Phi_\theta(r) = \max(0, \min(2r, 2, 2\frac{(1-\theta)\Delta r_{iu} + \theta \Delta r_{ki} r}{\Delta r_{iu} + \Delta r_{ki}})), \tag{5.3.8}$$

where θ is a real parameter in $[0, 1]$. The case $\theta = \frac{1}{3}$ corresponds to a third order spatial approximation on a uniform grid. The case $\theta = \frac{1}{2}$ corresponds to the limiter defined by Equation (5.3.6).

5.4 Numerical Test Cases

The test cases involve two phase flow (oil-water) initial oil saturation is prescribed and water is injected. Water saturation contours are shown in each case. Solid wall (zero normal flow) boundary conditions are applied on all solid boundaries of each reservoir

domain. In all cases flow rate is specified at the (inflow) injector and pressure is prescribed at the (outflow) producer and a consistent Darcy flux approximation is used. The different grid types employed are shown below.

For all cases, unit mobility ratio is used and $M_p = 1$ for $p = w, o$. The primary unknown is the (normalized) water saturation S. In the first four cases, a linear flux is used for the relative permeability. The water and oil mobilities are respectively $\lambda_w(S) = S$ and $\lambda_o(S) = (1 - S)$.

5.4.1 Case 1: Linear Piston Flow

The first case is a study of a linear injection problem using perturbed and distorted triangular grids shown in Figure 5.2(a) and Figure 5.4(a) respectively. Injection and production wells are located along opposite sides of the rectangular domain. Total mobility is constant and the permeability tensor is assumed to be diagonal isotropic so that the pressure is solved exactly (in this particular case) using the consistent Darcy flux. Thus any error in the saturation field is entirely due to the convective flux approximation. Water saturation contours are shown at 0.7 pore volumes injected (PVI) for both unstructured grids.

The first results, Figure 5.2(b) and Figure 5.4(b), show the effect of employing the first order upwind scheme for the convective flux.

Contours of the analytical solution are projected on to the grid and shown in Figure 5.2(c) and Figure 5.4(c). In this case, the analytical solution corresponds to

$$S(x, y, PVI) = 1_{|x<=PVI}.$$

where 1_A denotes the characteristic function on the domain A.

Higher order results computed using respectively the Fromm limiter defined in Equation (5.2.9), the Taylor series limiter (Equation (5.3.6)) and the θ-weighted limiter (Equation (5.3.8)) with $\theta = \frac{1}{3}$ are shown for each grid, Figures 5.3 and 5.5. Results using the Green-Gauss limiter (Equation (5.3.7)) and Least Squares limiter (Equation (5.3.5)) are omitted here as they are qualitatively similar to the ones using the Taylor Series limiter.

The first order scheme results show excessive numerical diffusion in the scheme, in addition to a clear dependency on the grid structure. The contours of the projected analytical solution suggest a contouring effect which might introduce some irregularity in the actual appearance of the results.

Figures 5.3 and 5.5 show that on both grids, the higher order schemes provide considerable improvement in the resolution of the saturation front specially in the case of the random perturbed grid which presents a strong irregularity. The Taylor Series limiter produces similar results to the Fromm limiter without distance scaling in this case. Finally, the results from the θ-limiter for $\theta = \frac{1}{3}$, show similar resolution compared with the Taylor Series limiter.

5.4.2 Case 2: Grid Orientation Study

The second case is a study of local grid orientation. Results are computed on a distorted coarse grid and on a corresponding fine grid for different types of triangulation as shown in Figure 5.6 and Figure 5.10. The permeability tensor is assumed to be diagonal isotropic so that the pressure field is essentially Laplacian in this case. Injection and production wells are located half way along opposite sides of the rectangular domain, water saturation contours are shown at 0.2 PVI.

First order results for the coarse grid (14x15) in Figure 5.8 show that the direction of triangulation effectively introduces a full tensor effect due to the strong local grid orientation. The high order schemes improve front resolution but cannot completely remove the effect of grid orientation on the solution due to the coarse grid level, Figure 5.9. Similar results are obtained for all of the Fromm based non-uniform grid limiters in this case. From Figure 5.7, we note that the discrete pressure field, obtained with a consistent Darcy flux, also contributes a small bias in the numerical pressure field in this case.

For the finer grid (26x27), the first order results still retain a bias due to the direction of triangulation. In comparison, the high order schemes improve front resolution and reduce grid orientation effects, Figure 5.11.

5.4.3 Case 3: Full Tensor Point Source to Point Sink

The third case involves an anisotropic homogeneous tensor with principal axes oriented at 45 degrees to the reservoir domain. The domain principal permeability direction is parallel to $y = x$, creating a full tensor with respect to the uniform grid shown in Figure 5.13(a). The normalized tensors have components $K_{xx} = 1.0$, $K_{yy} = 1.0$, $K_{xy} = 0.82$. Boundary conditions are imposed as in *Case 2*. The results are shown at time 0.2 PVI. The effect of the full tensor is shown in Figure 5.13(b) for the first order scheme and Figure

5.13(c) for the higher order scheme. The strong cross flow effect due to the dominant angled permeability field is apparent from the elongated saturation front.
Results for a principal axis at -45 degrees are shown in Figure 5.14. In both cases, the higher order schemes capture the front with improved resolution. Note that the saturation profiles corresponding to the two full tensor fields are mirror images.

5.4.4 Case 4: Taylor Series Limiter on Distorted High Aspect Ratio Grid

In this case a classical quarter five-spot system is tested with water injection at the bottom left corner and oil produced at the top right corner. The exact evolving front is always symmetric about $y = x$. The nature of the grid (Figure 5.15(a)) used provides a severe test for the schemes. The higher order results in Figures 5.16(a) and 5.16(b) both provide significant improvement in front resolution compared to that of the first order scheme in Figure 5.15(b). Here we also note that some improvement in symmetry of the front is obtained with the spatial weighted Taylor series higher order Fromm limiter Figure 5.16(b), when compared to the standard higher order Fromm limiter Figure 5.16(a).

5.4.5 Case 5: Non Linear Buckley Leverett Problem on Delaunay Meshes

In this case a nonlinear Buckley-Leverett quarter five-spot problem is tested with water injection at the bottom left corner and oil produced at the top right corner. Here the water and oil mobilities are respectively $\lambda_w(S) = S^2$ and $\lambda_o(S) = (1 - S)^2$. A Delaunay triangulation is used to define the grid. The coarse grid has 108 nodes and the fine grid has 290 nodes, Figures 5.17(a) and 5.18(a). The Fromm based Taylor Series limiter (Equation (5.3.6)) is employed. Results are shown at time 0.3 PVI.
The higher order results in Figures 5.17(c) and 5.18(c) provide significant improvement in front resolution compared to that of the first order scheme in Figures 5.17(b) and 5.18(b).

5.4.6 Case 6: Piston Flow in a Heterogeneous Medium

The last case involves linear injection into a heterogeneous medium where injection and production wells are located along opposite sides of the rectangular domain. Results are obtained using a 55x15 uniform grid (Figure 5.20(a)). The permeability distribution

is from Layer 6 of Model 2 of the 10th SPE Comparative Solution Project [28]. This layer is characterised by a smoothly varying lognormal permeability field that spans six orders of magnitude. Logarithm of the upscaled permeability field is depicted in Figure 5.20(b). Figure 5.21 shows saturation profiles after 0.5 PVI computed with the standard single-point upwind (Figure 5.21(a)) method and the higher order method (Figure 5.21(b)). The higher order method increases resolution significantly compared to the first order single-point upwind method, the latter shows excessive numerical diffusion producing non-physical features in the numerical solution. The higher order scheme is able to capture the fingering front and provides much improved resolution of the solution.

5.5 Conclusions

Higher order convective flux approximations are presented for unstructured grids. The schemes are coupled with consistent continuous Darcy-flux approximations and applied to two-phase flow problems.

Two-phase flow comparisons between higher order and standard methods in reservoir simulation are presented for a range of distorted unstructured grids. A sequence of non-uniform mesh limiters are also presented and tested. The comparisons indicate that while the higher order schemes are similar in performance, the Fromm based Taylor Series limiter is more robust for distorted meshes. The results demonstrate the benefits of the higher order schemes both in terms of improved front resolution and significant reduction in unstructured local grid orientation for diagonal and full-tensor velocity fields.

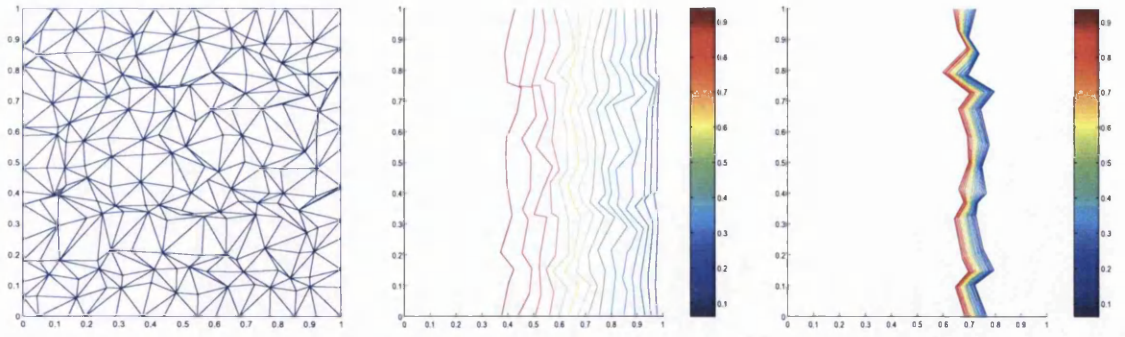

(a) (b) (c)

Figure 5.2: Case 1 - (a) Random perturbed Grid, (b) projection of the first order result, (c) projection of the analytical solution.

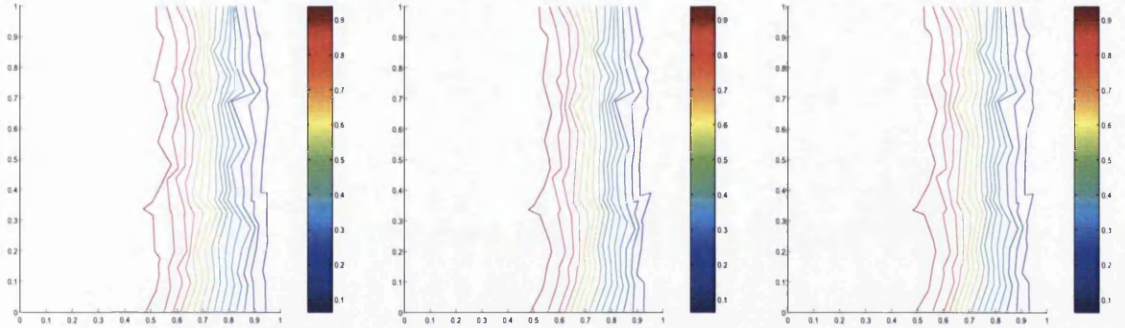

(a) (b) (c)

Figure 5.3: Case 1 - Projection of the higher-order results using the (a) non weighted Fromm, (b) Taylor Series limiter (c) weighted limiter with $\theta = \frac{1}{3}$ on the random perturbed grid.

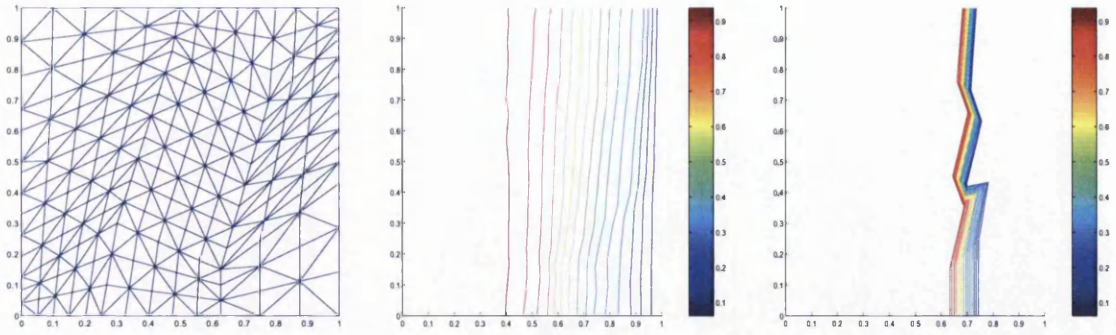

(a) (b) (c)

Figure 5.4: Case 1 - (a) Distorted Grid; projection of the (b) first order result and the (c) analytical solution.

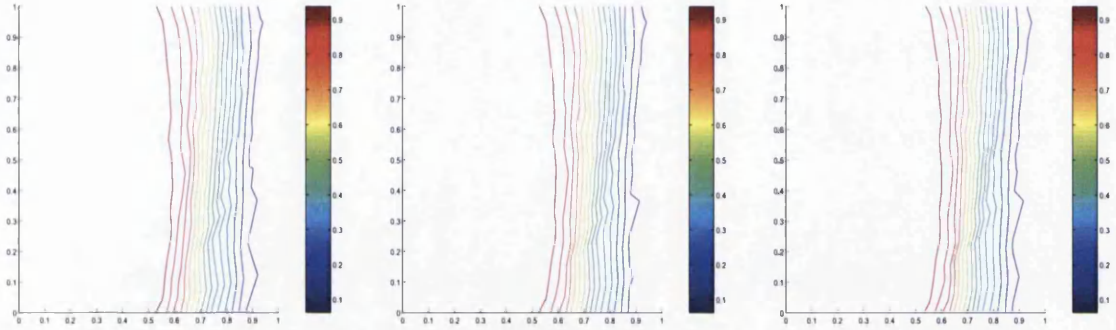

(a) (b) (c)

Figure 5.5: Case 1 - Projection of the higher order results using the (a) non weighted Fromm, the (b) Taylor Series limiter and the (c) weighted limiter with $\theta = \frac{1}{3}$ on the distorted grid.

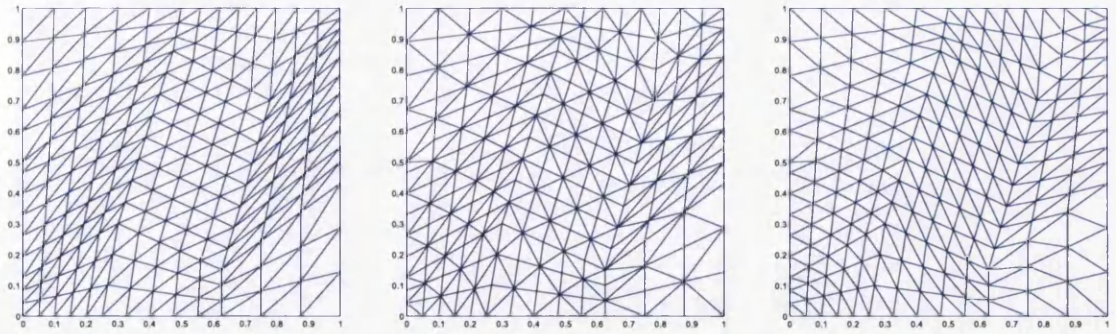

(a) (b) (c)

Figure 5.6: Case 2 - Coarse grids.

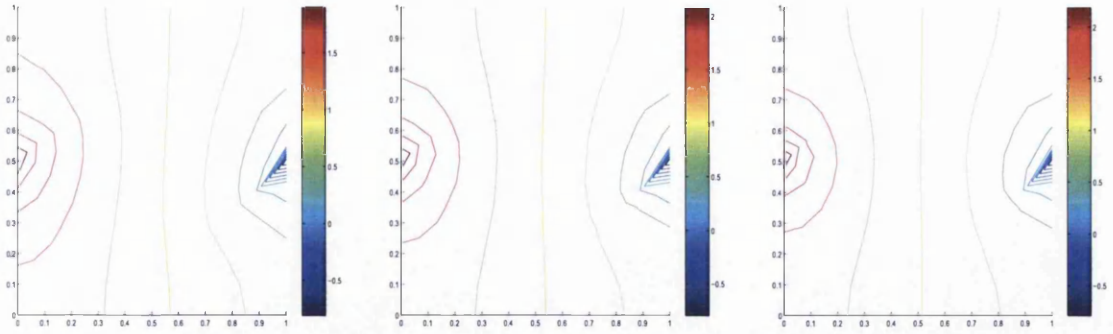

(a) (b) (c)

Figure 5.7: Case 2 - Pressure field on the coarse grids.

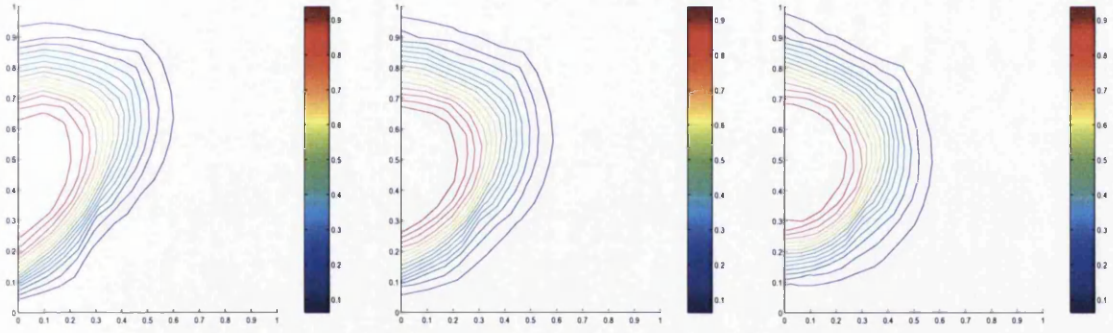

(a) (b) (c)

Figure 5.8: Case 2 - First order results on the coarse grids.

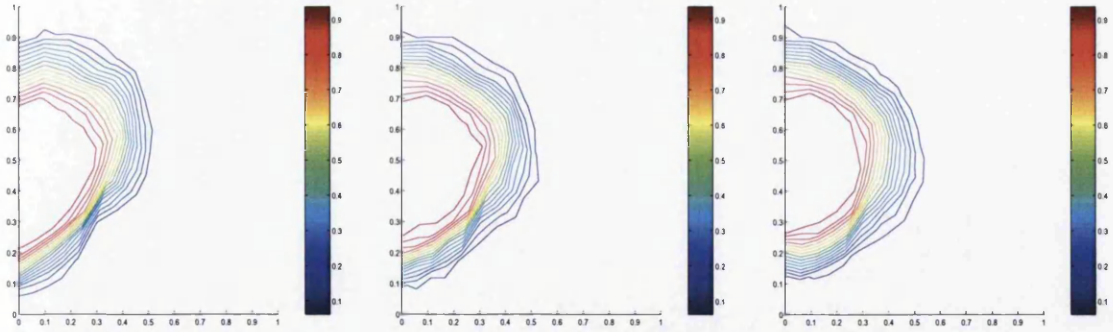

(a) (b) (c)

Figure 5.9: Case 2 - Higher order results on the coarse grids.

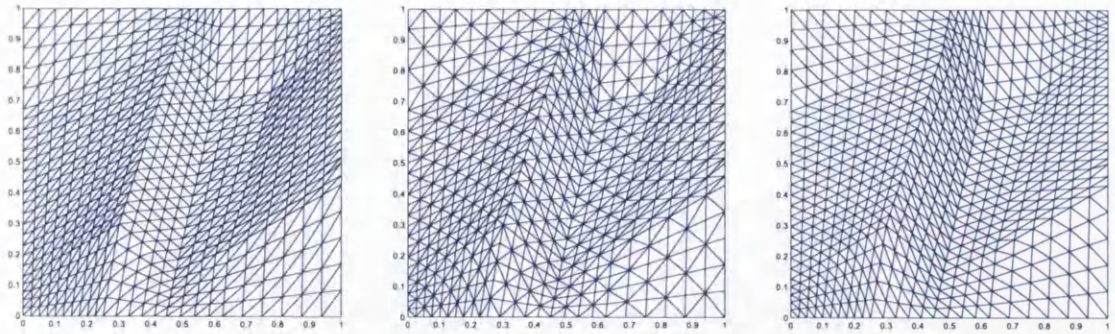

(a) (b) (c)

Figure 5.10: Case 2 - Fine grids.

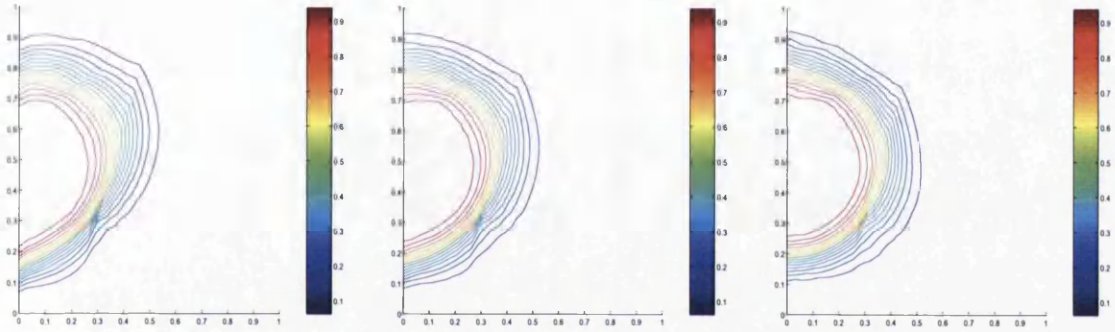

(a) (b) (c)

Figure 5.11: Case 2 - First order results on the fine grids

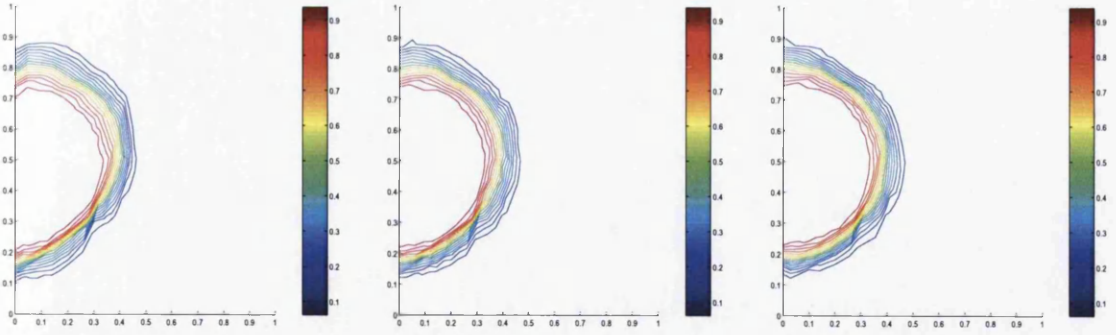

(a) (b) (c)

Figure 5.12: Case 2 - Higher order results on the fine grids.

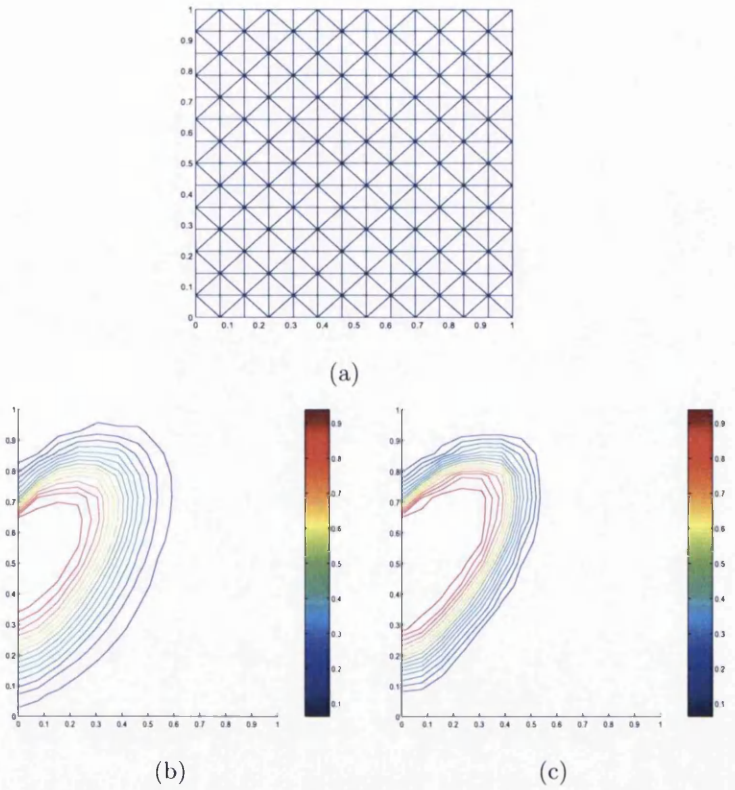

(a)

(b) (c)

Figure 5.13: Case 3 - Full tensor 45 degrees -(a) Uniform grid (b) first order results and (c) higher order results.

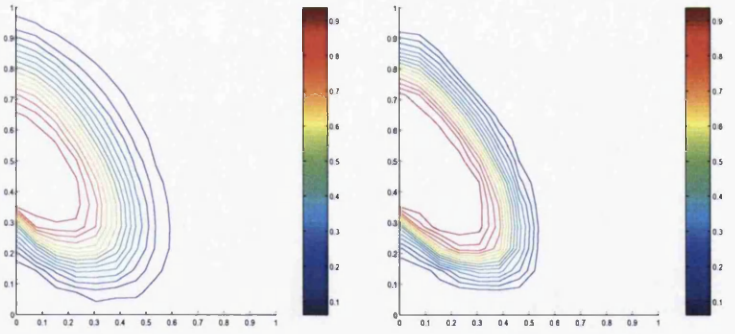

(a) (b)

Figure 5.14: Case 3 - Full tensor -45 degrees - (a) First order results and (b) higher order results.

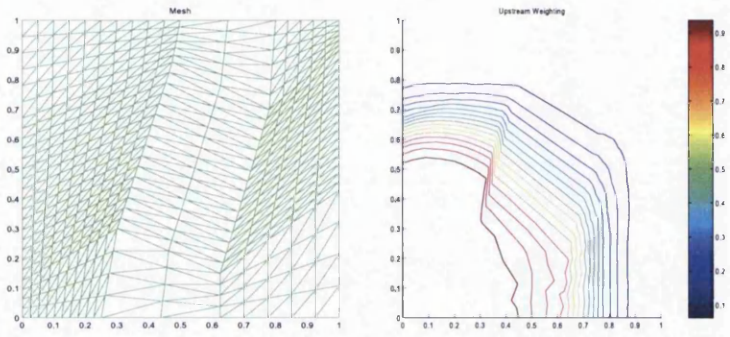

(a) (b)

Figure 5.15: Case 4 - (a) High aspect ratio grid and the (b) first order saturation profile.

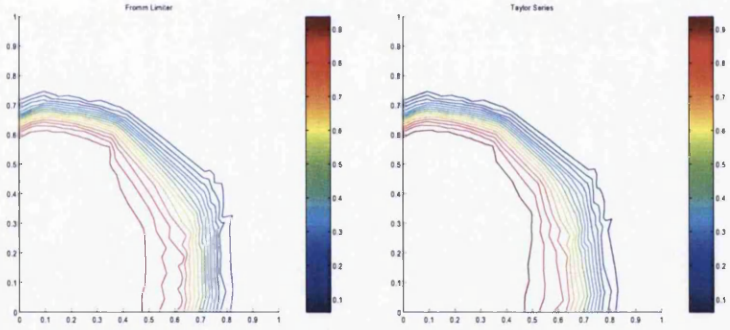

(a) (b)

Figure 5.16: Case 4 - Higher order using the (a) standard Fromm limiter and the (b) Taylor Series weighted limiter.

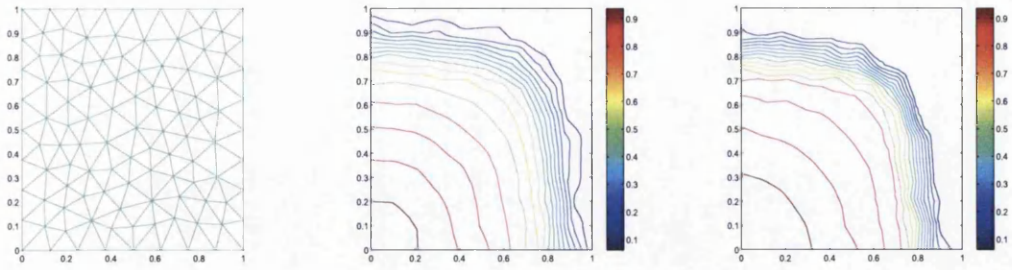

(a) (b) (c)

Figure 5.17: Case 5 - (a) Coarse grid, (b) first order result and (c) higher order result using Taylor Series Fromm based limiter.

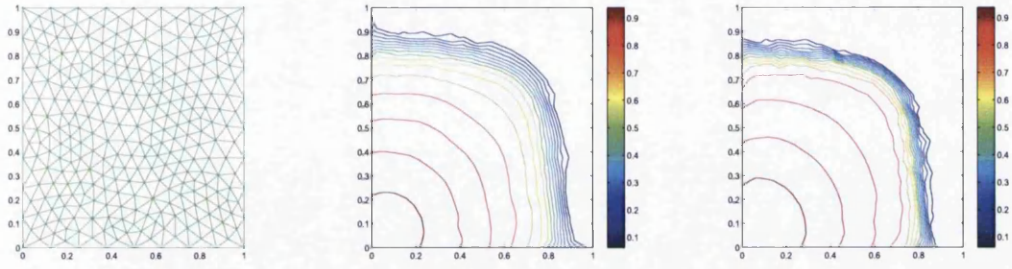

(a) (b) (c)

Figure 5.18: Case 5 - (a) Fine grid, (b) first order result and (c) higher order result using Taylor Series Fromm based limiter.

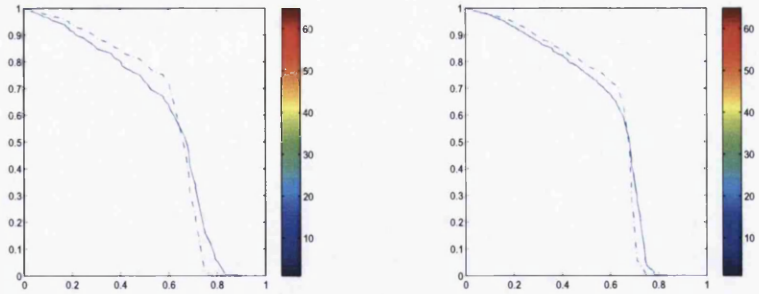

(a) (b)

Figure 5.19: Case 5 - 1D Profiles along the diagonal for first Order results (solid) and higher order results (dashed) on the (a) coarse grid and the (b) fine grid.

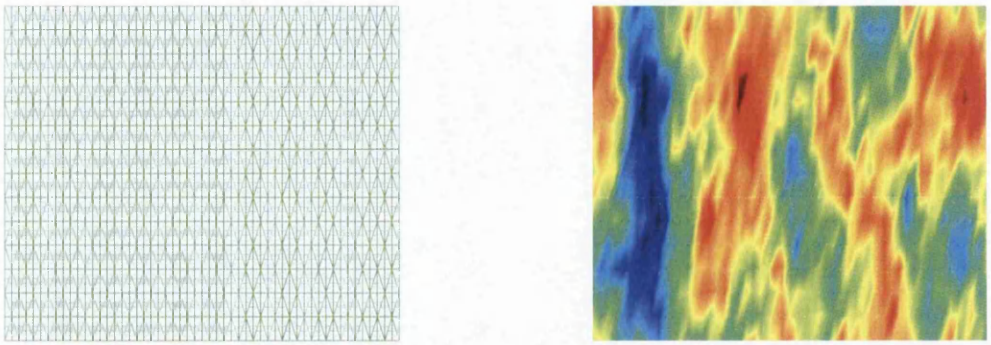

(a) (b)

Figure 5.20: Case 6 - (a) Grid and (b) logarithm of the permeability field.

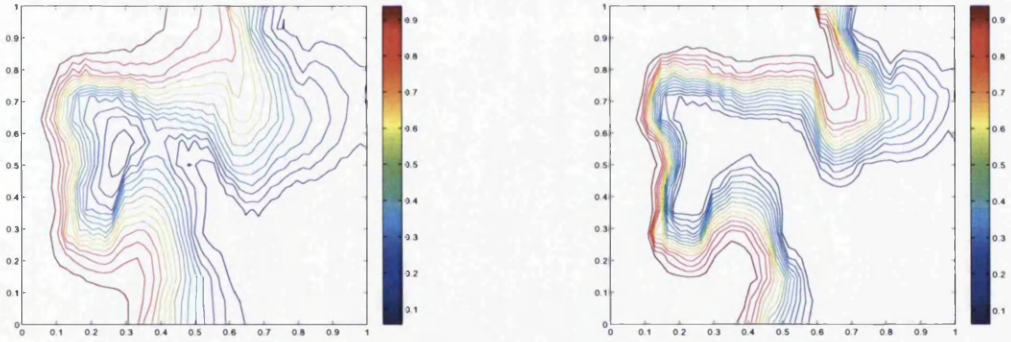

(a) (b)

Figure 5.21: Case 6 - (a) first order results and (b) higher order results using Taylor Series Fromm Limiter.

Chapter 6

Higher Dimensional Schemes on Quadrilateral Grids

6.1 Introduction

The standard upwind scheme in two dimensions suffers from many deficiencies as discussed in [132, 36, 141, 142, 88] and illustrated with linear advection.

By definition, single-point upstream weighting chooses to define the control volume face flux by using information that flows across the face. However, crucially when selecting this data, while the criteria is based on the sign of the wave velocity at the control volume face, the actual data is defined by the nearest neighbour coordinate value. In one dimension, this is sufficient to unambiguously define the scheme in terms of the incoming wave direction. However, in higher dimensions the wave direction can be at an angle according to the wave velocity vector direction. The deficiency of the standard scheme is its failure to recognize exactly from where the wave is coming and consequently fail to use the real upwind data.

The direct use of the standard scheme in multiple dimensions thus creates an additional source of numerical diffusion referred to as cross-wind diffusion. The focus here is on reducing cross wind-diffusion.

The actual physical wave direction which could be in any direction, not just along coordinate lines will require that the scheme has extra information available within a cell radius of each control-volume face. The main idea of the multidimensional scheme is to trace back along the two-dimensional characteristic to the point of intersection with the

upwind coordinated lines whenever possible.

In this chapter, higher dimensional convection schemes that minimize cross-wind diffusion are presented for convective flow approximation on quadrilateral structured and unstructured grids. The higher dimensional schemes are coupled with full-tensor Darcy flux approximations.

Formulation of the family of higher dimensional schemes on structured quadrilateral grids is presented in section 6.2.3. Formulations for unstructured quadrilateral grids are presented in section 6.3. Two-phase flow results are presented in section 6.4 that demonstrate the advantages of the new higher dimensional flux-continuous formulation.

Benefits of the resulting schemes are demonstrated for classical test problems in reservoir simulation including cases with full tensor permeability fields. The test cases involve a range of structured and unstructured grids with variations in orientation and permeability that lead to flow fields that are poorly resolved by standard simulation methods.

The higher dimensional formulations are shown to effectively reduce numerical cross-wind diffusion effect, leading to improved resolution of concentration and saturation fronts. Gravity flow will be neglected in this chapter and will be considered in chapter 8.

6.2 Wave Oriented Upwind Schemes on Cartesian Grids

A family of genuinely multidimensional conservative schemes for the transport equation is first presented on structured quadrilateral grids. This formulation was first introduced by Edwards in reservoir simulation [54] and provides the basis of the developments herein. In this section, we restrict ourselves to the study of the linear advection equation with a uniform velocity field.

Consider a cartesian mesh with uniform spacing in the x and y directions, Δx and Δy, as shown in Figure 6.1, on which we wish to solve the scalar wave equation of the form:

$$S_t + F(S)_x + G(S)_y = 0. \tag{6.2.1}$$

The locally conservative form of the finite volume discretization is then written as:

$$S_{i,j}^{n+1} - S_{i,j}^{n+1} = -\frac{\Delta t}{\Delta x}(F_{i+1/2,j} - F_{i-1/2,j}) - \frac{\Delta t}{\Delta y}(G_{i,j+1/2} - G_{i,j-1/2}). \tag{6.2.2}$$

6.2.1 Study of a Constant Velocity Case

We shall first consider the case of linear advection where

$$S_t + aS_x + bS_y = 0. \tag{6.2.3}$$

We assume that both a and b are positive treating the other cases by symmetry. The exact solution to Equation (6.2.3) subject to the initial condition $S(x, y, t = 0) = S_0(x, y)$ is given by:

$$S(x, y, t) = S_0(x - ta, y - tb). \tag{6.2.4}$$

The locally conservative form of the finite volume discretization is then written as:

$$S_{i,j}^{n+1} - S_{i,j}^n = -\nu^x(S_{i+1/2,j}^n - S_{i-1/2,j}^n) - \nu^y(S_{i,j+1/2}^n - S_{i,j-1/2}^n). \tag{6.2.5}$$

where $\nu^x = a\Delta t/\Delta x$ and $\nu^y = b\Delta t/\Delta y$.
In this case, the standard first order accurate single point upwind scheme reduces to:

$$S_{i,j}^{n+1} - S_{i,j}^n = -\nu^x(S_{i,j}^n - S_{i-1,j}^n) - \nu^y(S_{i,j}^n - S_{i,j-1}^n). \tag{6.2.6}$$

The scheme is defined on a five point stencil. It is positive and stable under the restrictive CFL condition:

$$\nu^x + \nu^y \leq 1. \tag{6.2.7}$$

The stability condition of Equation (6.2.7) indicates a reduction in the time step compared to one dimension due to the higher dimensional contribution. In order to account for the genuine two dimensional wave direction within the upwind scheme, it is necessary to include more information to resolve the wave direction and assign the corresponding upwind data. For a cartesian grid, the natural extension of scheme is to extend the stencil from a total of five possible nodes to a nine nodes including the corner point data [54, 36].

Family of Conservative Characteristic Tracing Schemes

A family of positive upwind schemes was introduced for flow in porous media in [54]. The method was presented on structured grids and applied to two phase flow problems with strong cross-flow. Upwind data is interpolated on to the characteristics where the upwind data is written as:

$$\begin{aligned} S_{i+1/2,j} &= (1-\eta)S_{i,j}^n + \eta S_{i,j-1} \\ S_{i,j+1/2} &= (1-\xi)S_{i,j}^n + \xi S_{i-1,j} \end{aligned} \tag{6.2.8}$$

where ξ and η are the weighting factors with $0 \leq \xi \leq 1$ and $0 \leq \eta \leq 1$. Assuming that ξ and η are constant on each grid cell, this formulation could be interpreted as a bilinear variation of the saturation over the cell [54]. The wave tracing and interpolant points are illustrated in Figure 6.1. The approximation gives rise to a family of generalized upwind

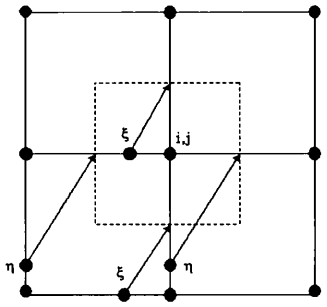

Figure 6.1: Characteristics.

difference approximations of the form.

$$\begin{aligned} S_{i,j}^{n+1} &= (1-\nu^x(1-\eta)-\nu^y(1-\xi))S_{i,j}^n \\ &+ (\nu^x(1-\eta)-\nu^y\xi)S_{i-1,j}^n \\ &+ (\nu^y(1-\xi)-\nu^x\eta)S_{i,j-1}^n \\ &+ (\nu^x\eta+\nu^y\xi)S_{i-1,j-1}^n. \end{aligned} \tag{6.2.9}$$

Positivity Monotonicity and Stability

First note that the coefficients of the explicit values of $S_{i,j}^n$ in Equation (6.2.9) sum to unity. The scheme is positive and stable if the updated value $S_{i,j}$ is a convex average of the previous data, preventing the occurrence of any spurious oscillations. Note that in this case the contribution of the corner node $S_{i-1,j-1}^n$ is always positive by definition. Thus the positivity conditions reduce to:

$$\begin{aligned} (\nu^x+\nu^y) &\leq 1+(\eta\nu^x+\nu^y\xi) \\ \nu^x\eta+\nu^y\xi &\leq \min(\nu^y,\nu^x). \end{aligned} \tag{6.2.10}$$

The first inequality is clearly positive for larger CFL numbers than the upstream weighting scheme, provided non zero values of (ξ,η) are used. This implies that the use of the corner

data points will enhance the stability of the standard method.

Multidimensional Schemes on Cartesian Grids

The class of schemes discussed above turns out to be identical to the one presented by Roe and Sidilkover in [138] for linear advection on regular grids. The authors focused on a class of schemes described by a single parameter family. Extension to three dimensional regular grids was also presented.

On a regular Cartesian grid where $\Delta x = \Delta y$, the single parameter κ family of consistent schemes can be written in the form:

$$\begin{aligned} S_{i,j}^{n+1} = S_{i,j}^{n} + \frac{\Delta t}{2\Delta x} \quad [\quad & (-a-b-\kappa)S_{i,j}^{n} \\ + \quad & (a-b+\kappa)S_{i-1,j}^{n} \\ + \quad & (-a+b+\kappa)S_{i,j-1}^{n} \\ + \quad & (a+b-\kappa)S_{i-1,j-1}^{n}], \end{aligned} \tag{6.2.11}$$

where the κ is a function of a and b and can be understood as defining an interpolation scheme of the four upwind nodes at the location $(x_{i,j} - \Delta t \cdot a, y_{i,j} - \Delta t \cdot b)$. It can also be shown that $\kappa = (a+b) - 2(\xi b + \eta a)$.

Positivity requires that

$$|a-b| \leq \kappa \leq a+b, \tag{6.2.12}$$

$$\Delta t \leq \frac{2\Delta x}{a+b+\kappa}. \tag{6.2.13}$$

Table 6.1 shows the expression for κ for three common multidimensional numerical discretisations in the literature namely the N-scheme of Roe and Sidilkover [138], Koren's scheme [99] and the CTU scheme of Collela [36] compared with the single point upstream weighting scheme. The N-scheme (Narrow Scheme) [142, 150] uses a linear interpolation

Scheme	κ	Time step
Single Point Upwind	$a+b$	$\Delta t \leq \frac{\Delta x}{a+b}$
Koren's scheme	$\frac{a^2+b^2}{a+b}$	$\Delta t \leq \Delta x \frac{a+b}{a^2+ab+b^2}$
CTU	$a+b-2\frac{\Delta t}{\Delta x}ab$	$\Delta t \leq \frac{\Delta x}{\max(a,b)}$
N scheme	$\lvert a-b \rvert$	$\Delta t \leq \frac{\Delta x}{\max(a,b)}$

Table 6.1: Comparison of different values of κ for classical Multidimensional schemes [100].

in the upwind triangle and depends on a "narrow" three node stencil whereas the CTU scheme introduced by Collela [36] uses a bilinear interpolation on the quadrilateral cell. For this scheme, κ depends on the time step unlike the other presented methods. Note that both the N scheme and the CTU scheme allow the largest time step according to Equation (6.2.12) and single point upwinding scheme the most restrictive.

Diffusion Errors and Optimal Linear Schemes

The quest for an optimal linear scheme requires a better definition of the optimality condition with regards to the numerical diffusion errors introduced by the the family of discretisation on a Cartesian grid.

In a rigourous discussion, Shubin and Bell [149] derived, for miscible displacement, the form of the truncation error terms up to second order, for a general discretisation stencil. They used a modified equation analysis to examine the dependence of truncation error on the angle between the flow direction and the grid lines.

Here, we adopt a slightly different approach to discuss the directional dependence of the numerical diffusion for immiscible incompressible linear two phase flow in porous media assuming a constant uniform total velocity field neglecting gravity and capillary effects.

In order to interpret the numerical diffusion, it is convenient to write the truncation error of the scheme Equation (6.2.11) in the streamline coordinates (x', y') [149, 150, 82, 99, 54], where x' is aligned with the flow direction.

Let

$$\theta = \arctan(\frac{b}{a})$$

define the angle of the flow velocity to the grid $x-$coordinate. Then the velocity vector $\mathbf{V}$ can be expressed as

$$\mathbf{V} = |\mathbf{V}| \begin{bmatrix} \cos(\theta) \\ \sin(\theta) \end{bmatrix}$$

where $|\mathbf{V}| = \sqrt{a^2 + b^2}$ denotes the velocity modulus. The transformed coordinates (x', y') are obtained via :

$$\begin{bmatrix} x' \\ y' \end{bmatrix} = \begin{bmatrix} \cos(\theta) & \sin(\theta) \\ -\sin(\theta) & \cos(\theta) \end{bmatrix} \begin{bmatrix} x \\ y \end{bmatrix}. \tag{6.2.14}$$

First note that expanding the Taylor series approximation of Equation (6.2.11) in the original Cartesian grid coordinates (x, y) yields:

$$\begin{aligned} S_t + aS_x + bS_y &= \frac{\Delta_x}{2}(a - \gamma\cos^2(\theta))S_{xx} \\ &+ \frac{\Delta_x}{2}(b - \gamma\sin^2(\theta))S_{yy} \\ &+ \frac{\Delta_x}{2}(a + b - \kappa - 2\gamma\sin(\theta)\cos(\theta))S_{xy} + O(\Delta x^2), \end{aligned} \tag{6.2.15}$$

where $\gamma = \frac{\Delta t|\mathbf{V}|}{\Delta x}$ is the CFL number.

Thus, using Equation (6.2.14), the Taylor expansion of Equation (6.2.3) in the streamline coordinates (x', y') takes the form [138, 82]:

$$\begin{aligned} S_t + |\mathbf{V}|S_{x'} &= D_{x'x'}\ S_{x'x'} \\ &+ D_{y'y'}\ S_{y'y'} \\ &+ D_{x'y'}\ S_{x'y'} + \text{ HO terms}, \end{aligned} \tag{6.2.16}$$

where

$$\begin{aligned} D_{x'x'} &= |\mathbf{V}|\frac{\Delta x}{2}[\sin(\theta) + \cos(\theta) - \frac{\kappa}{|\mathbf{V}|}\sin(\theta)\cos(\theta) - \frac{\Delta t}{\Delta x}|\mathbf{V}|], \\ D_{y'y'} &= \frac{\Delta x}{2}[\kappa\sin(\theta)\cos(\theta)], \\ D_{x'y'} &= |\mathbf{V}|\frac{\Delta x}{2}[\cos(\theta) - \sin(\theta) + \frac{\kappa}{|\mathbf{V}|}(\sin^2(\theta) - \cos^2(\theta))] \end{aligned} \tag{6.2.17}$$

and κ is defined in table 6.1.

Note that the first order truncation error shows three different diffusion terms: longitudinal (corresponding to $D_{x'x'}$), cross-wind (corresponding to $D_{y'y'}$) and cross-term or rotational ($D_{x'y'}$ coefficient) diffusions.

Equation (6.2.16) implies that when κ is independent of the Δt, only the longitudinal diffusion is affected by the time stepping. Zero-cross wind diffusion (dissipation) is obtained for the case $\kappa = 0$, which results in a non-positive scheme. The optimal positive linear scheme which minimizes cross-wind diffusion corresponds with the N scheme (Narrow Scheme) [142, 138]. As shown by Roe and Sidilkover who gave its name, it is identical to the upwind scheme of Rice and Schnipke [134] on regular quadrilateral grids, provided that the latter are triangulated using the optimal choice for diagonals.

Figure 6.3 illustrates the magnitude of the directional diffusion coefficients versus the angle of the constant flow vector to the grid for the SPU, N-scheme and Koren's scheme.

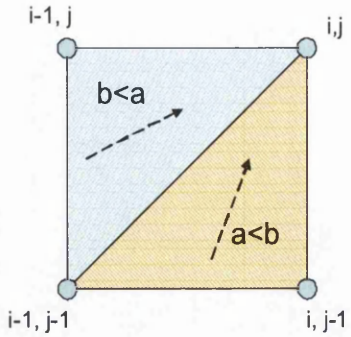

(a)

Figure 6.2: Stencil of the optimal linear positive scheme on Cartesian grids [138].

Since κ depends on Δt for the CTU scheme, the behaviour of other schemes can be reproduced for different time step sizes and therefore will be omitted in this analysis. In particular, setting $\Delta t = \frac{\Delta x}{\max(a,b)}$, the CTU scheme is identical to the N-scheme and corresponds to the SPU scheme for $\Delta t = 0$.
Figure 6.3(b) shows that the N-scheme has minimal cross-wind diffusion for the family of positive schemes, and standard single point upwind has maximal transverse diffusion.
The plots clearly show that all schemes have zero cross-term diffusion for flow that is aligned with the grid and the N-scheme has zero cross-wind diffusion at $\theta = \pi/4$ where Equation (6.2.11) reduces to:

$$S_{i,j}^{n+1} = S_{i,j}^{n} - \frac{a\Delta t}{\Delta x}[S_{i,j}^{n} - S_{i-1,j-1}^{n}], \tag{6.2.18}$$

involving only corner nodes and the scheme behaves as a 1-D first order approximation on the diagonal nodes.

Also, the diffusion tensor of Koren's scheme is flow aligned since the cross-term diffusion is zero for all θ and the standard upstream weighting scheme has the largest cross-term diffusion in modulus (Figure 6.3(c)).
Figure 6.3(a) shows the part of the longitudinal diffusion error that is independent of the time step size Δt. It is clear that for a fixed time step, SPU provides the smallest amount of longitudinal smearing of the solution whereas N-scheme proves to be the most diffuse in the direction of the flow.

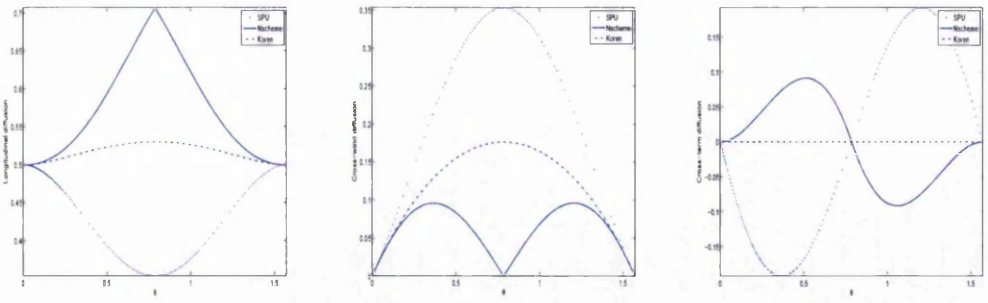

(a) Longitudinal diffusion (b) Cross-wind Diffusion (c) Cross-term Diffusion

Figure 6.3: Cross-wind and cross-term diffusion as a function of the angle of the flow to the grid [138] for $|\mathbf{V}| = 1$ and $\Delta x = 1$. The SPU scheme is illustrated in dotted line, the solid line represents the N-scheme and the dashed line corresponds to the Koren's scheme.

Optimal Linear Schemes on Non Uniform Quadrilateral Grids

In the case of regular non-uniform quadrilateral grids, the optimality condition for Equation (6.2.10) is equivalent to the following equality

$$(\nu^x \eta + \nu^y \xi) = \min(\nu^y, \nu^x). \tag{6.2.19}$$

Note that this choice will make the coefficient of either $S^n_{i-1,j}$ or $S^n_{i,j-1}$ equal to zero, so that the stencil is always one of the two triangles shown in Figure 6.2 which makes the stencil the smallest possible for the optimal positive scheme. Substituting the Equation (6.2.19) in the first inequality of Equation (6.2.10) yields the CFL condition

$$\max(\nu_x, \nu_y) \leq 1. \tag{6.2.20}$$

By choosing $\xi = 0$ and $\eta = 0$, the standard upwind scheme is recovered. The scheme reduces to the first order CTU scheme introduced by Collela in [36] for $\xi = \nu^x$ and $\eta = \nu^y$ [54].

A symmetric choice of the parameters ξ and η that satisfies the optimality condition Equation (6.2.19) corresponds with:

$$\begin{aligned} \xi &= \frac{1}{2}\min(1, \frac{\nu^x}{\nu^y}) \\ \eta &= \frac{1}{2}\min(1, \frac{\nu^y}{\nu^x}). \end{aligned} \tag{6.2.21}$$

Note that in this condition, the parameters ξ and η are chosen to be independent of the time stepping. Also, the geometric aspect ratio of the grid is incorporated into these

parameters. This choice gives zero cross diffusion schemes for the cases $a = b$, $a = 0, b = 1$ and $a = 1, b = 0$ on a Cartesian grid. Other choices of the weighting parameters within the positivity limits are:

$$\begin{aligned} \xi &= \frac{1}{2}\min(1, \frac{\nu^x}{\nu^x + \nu^y}) \\ \eta &= \frac{1}{2}\min(1, \frac{\nu^y}{\nu^x + \nu^y}). \end{aligned} \tag{6.2.22}$$

This choice corresponds with Koren's scheme on Cartesian grids [99].

6.2.2 Study of a Variable Coefficient Case

Data Based Scheme Formulation

We now account for the variability of the velocity field and the impact on the formulation of the scheme. This step is key to generalisation to unstructured quadrilaterals.

$$S_t + (a(x,y)S)_x + (b(x,y)S)_y = 0. \tag{6.2.23}$$

The locally conservative form of the finite volume discretization is then written as:

$$S^{n+1}_{i,j} - S^n_{i,j} = -(\nu^x_{i+1/2,j} S^n_{i+1/2,j} - \nu^x_{i-1/2,j} S^n_{i-1/2,j}) - (\nu^y_{i,j+1/2} S^n_{i,j+1/2} - \nu^y_{i,j-1/2} S^n_{i,j-1/2}), \tag{6.2.24}$$

where $\nu^x_{i+1/2,j} = a_{i+1/2,j}\Delta t/\Delta x$ and $\nu^y_{i,j+1/2} = b_{i,j+1/2}\Delta t/\Delta y$ are the resolved velocities at the center of the cell edges.
Upwind data in first order upstream weighting is computed using the directional wave speed and written as:

$$\begin{aligned} S^n_{i+1/2,j} &= S^n_{i,j} \text{ if } a_{i+1/2,j} \geq 0, \\ S^n_{i+1/2,j} &= S^n_{i+1,j} \text{ if } a_{i+1/2,j} < 0; \end{aligned} \tag{6.2.25}$$

and

$$\begin{aligned} S^n_{i,j+1/2} &= S^n_{i,j} \text{ if } b_{i+1/2,j} \geq 0, \\ S^n_{i,j+1/2} &= S^n_{i,j+1} \text{ if } b_{i+1/2,j} < 0. \end{aligned} \tag{6.2.26}$$

Family of Conservative Characteristic Tracing Schemes

Accounting for the multidimensional nature of the wave speed, the left and right states at the center of the edge connecting the nodes (i, j) and $(i+1, j)$ are calculated in a locally

conservative form via [54]:

$$S_{L_{i+1/2,j}} = (1-\xi_{i+1/2,j})S^n_{i,j} + \xi_{i+1/2,j}[\chi_{i+1/2,j}S_{i,j-1} + (1-\chi_{i+1/2,j})S_{i,j+1}]; \quad (6.2.27)$$
$$S_{R_{i+1/2,j}} = (1-\eta_{i+1/2,j})S^n_{i+1,j} + \eta_{i+1/2,j}[\chi_{i+1/2,j}S_{i+1,j+1} + (1-\chi_{i+1/2,j})S_{i+1,j-1}],$$

and equivalent reconstructions on the edge connecting the nodes (i,j) and $(i,j+1)$ take the form:

$$S_{L_{i,j+1/2}} = (1-\xi_{i,j+1/2})S^n_{i,j} + \xi_{i,j+1/2}[\chi_{i,j+1/2}S_{i-1,j} + (1-\chi_{i,j+1/2})S_{i+1,j}]; \quad (6.2.28)$$
$$S_{R_{i,j+1/2}} = (1-\eta_{i,j+1/2})S^n_{i,j+1} + \eta_{i,j+1/2}[\chi_{i,j+1/2}S_{i+1,j+1} + (1-\chi_{i,j+1/2})S_{i-1,j+1}],$$

where $0 \leq \xi_{i+1/2,j} \leq 1$, $0 \leq \eta_{i+1/2,j} \leq 1$, $0 \leq \xi_{i,j+1/2} \leq 1$ and $0 \leq \eta_{i,j+1/2} \leq 1$ denote the weighting factors used to interpolate the left state as a linear combination of the grid nodes depending on the direction of the wave speed. Note here that the weighting factors can vary spatially according to local wave speed. Here $\chi_{i+1/2,j}$ (respectively $\chi_{i,j+1/2}$) is a boolean parameter which accounts for the normal direction of the wave velocity with respect to the cell edge and takes 0 or 1 depending on the direction of the flow.

Positivity Analysis

First, we introduce the following notation which will be used for the remainder of this work. Let $x^+ = (x+|x|)/2$ and $x^- = (x-|x|)/2$ denote the positive and negative part of a real x. The convention of a positive (respectively negative) flux contribution entering (respectively leaving) the control volume (i,j) is adopted here.
The contribution to the scheme from node (i,j) to the control volume $(i+1,j)$ can be explicitly written as:

$$(1-\xi_{i+1/2,j})(\nu^x_{i+1/2,j})^+ + \eta_{i+1,j+1/2}(\nu^y_{i+1,j+1/2})^- + \eta_{i+1,j-1/2}(\nu^y_{i+1,j-1/2})^- S_{i,j}. \quad (6.2.29)$$

Hence, the positivity condition takes the form:

$$\xi_{i+1/2,j}(\nu^x_{i+1/2,j})^+ - \eta_{i+1,j+1/2}(\nu^y_{i+1,j+1/2})^- - \eta_{i+1,j-1/2}(\nu^y_{i+1,j-1/2})^- \leq (\nu^x_{i+1/2,j})^+. \quad (6.2.30)$$

In order to satisfy this condition, the weights are chosen to correspond with:

$$\xi_{i+1/2,j} = \frac{1}{3}\min(1, \frac{\max((\nu^y_{i,j+1/2})^+, (\nu^y_{i,j-1/2})^+)}{(\nu^x_{i+1/2,j})^+}), \text{ for } (\nu^x_{i+1/2,j})^+ > 0; \quad (6.2.31)$$
$$\eta_{i+1/2,j} = \frac{1}{3}\min(1, \frac{\max((\nu^y_{i+1,j+1/2})^+, (\nu^y_{i+1,j-1/2})^+)}{|\,(\nu^x_{i+1/2,j})^-\,|}), \text{ for } (\nu^x_{i+1/2,j})^- < 0.$$

Note here that the factor of a half 1/2 introduced in Equation (6.2.21) reduces to a 1/3, in order to preserve positive contributions to the saturation update for all flow conditions. Also, the weights are chosen to maximise the CFL number. The choice of weighting factors will be discussed in the next section 6.3.2.

6.2.3 Nonlinear Flux Formulation

For the general case, where the flux is nonlinear in saturation, we compare two formulations following [54].

Nonlinear Flux of Multi-dimensional Data

The first formulation involves the multi-dimensional upwind data reconstruction where we define the generalized flux by:

$$\begin{aligned} f(S_{L_{i+1/2,j}}) &= f\big((1-\xi_{i+1/2,j})S^n_{i,j} + \xi_{i+1/2,j}[\chi_{i+1/2,j}S^n_{i,j-1} + (1-\chi_{i+1/2,j})S^n_{i,j+1}]\big), \quad (6.2.32)\\ f(S_{R_{i+1/2,j}}) &= f\big((1-\eta_{i+1/2,j})S^n_{i+1,j} + \eta_{i+1/2,j}[\chi_{i+1/2,j}S^n_{i+1,j+1} + (1-\chi_{i+1/2,j})S^n_{i+1,j-1}]\big). \end{aligned}$$

An analogous definition is adopted for $S_{L_{i,j+1/2}}$ and $S_{R_{i,j+1/2}}$.

Nonlinear Multi-dimensional Flux

The second formulation, the multi-dimensional upwind flux reconstruction is written as:

$$\begin{aligned} f(S_{L_{i+1/2,j}}) &= (1-\xi_{i+1/2,j})f(S^n_{i,j}) + \xi_{i+1/2,j}[\chi_{i+1/2,j}f(S^n_{i,j-1}) + (1-\chi_{i+1/2,j})f(S^n_{i,j+1})], \quad (6.2.33)\\ f(S_{R_{i+1/2,j}}) &= (1-\eta_{i+1/2,j})f(S^n_{i+1,j}) + \eta_{i+1/2,j}[\chi_{i+1/2,j}f(S^n_{i+1,j+1}) + (1-\chi_{i+1/2,j})f(S^n_{i+1,j-1})]. \end{aligned}$$

Definition of $S_{L_{i,j+1/2}}$ and $S_{R_{i,j+1/2}}$ are defined analogously.
The weighting factors ξ and η used in Equations (6.2.32) and (6.2.33) are defined by Equation (6.2.31) for stability where a consistent definition of the local wave velocity components ν^x and ν^y is used. More specifically, in the case where the flux is of the form:

$$\begin{aligned} F(S) &= f(S)V^x_T, \quad (6.2.34)\\ G(S) &= f(S)V^y_T; \end{aligned}$$

which models multi-phase flow in the absence of gravity (see chapter 2, section 2.2.2), we choose:

$$\nu^x = \frac{\Delta t}{\Delta x} V_T^x, \qquad \nu^y = \frac{\Delta t}{\Delta y} V_T^y. \tag{6.2.35}$$

Another alternative for the definition of the tracing wave speed for the same nonlinear flux is to choose the Rankine-Hugoniot wave speed [49], where for example,

$$\nu^x_{i+1/2,j} = \frac{\Delta t}{\Delta x} V^x_{T_{i+1/2,j}} \frac{F_{i+1,j} - F_{i,j}}{S_{i+1,j} - S_{i,j}},$$

which includes spatial variation due to velocity field as well as non-linear flux variations. Finally, note that for constant wave speed, the schemes resulting from Equations (6.2.32) and (6.2.33) reduce to Equation (6.2.8).

6.3 Wave Oriented Upwind Schemes on Unstructured Quadrilateral Grids

In this section, two key issues are addressed when dealing with unstructured grids, namely:

1. the definition of the upwind direction based on the local wave velocity defined over the subcells and
2. the choice of the weighting coefficients to minimize the cross-wind diffusion while preserving positivity.

6.3.1 A Family of Wave Oriented Conservative Upwind Schemes

Edge based and cell based formulations are presented in this thesis. In this chapter, the focus is on the edge based approximation. The cell-based reconstructions are treated in chapter 9. First, recall the edge based finite volume approximation as in Equation (4.2.16):

$$\tau_j \frac{S_j^{n+1} - S_j^n}{\Delta t} + \sum_{e=1}^{N_{edV}} \mathrm{f}(S_{L_e}, S_{R_e}) \sum_{i_q=1}^{N_q} F_{T_q} = 0, \tag{6.3.1}$$

where i_q sums over the flux quadrature points (one per sub-face). Here we evaluate the subcell flux F_{T_q} on the control volume sub-face (dashed in Figure 6.4(a)) at the point of attachment to the cell edge e. The sub-face fluxes are represented by the arrows in Figure 6.5(a) and the quadrature points are chosen to coincide with the center of the cell edges. The upwind tracing procedure is comprised of two steps.

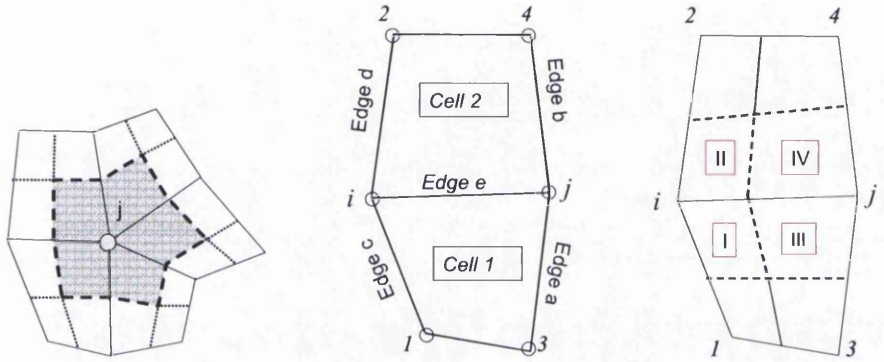

(a) (b) (c)

Figure 6.4: (a) Control volume (dashed line) (b) compact stencil (b) subcells.

Step I

The first step is to establish the global flux direction relative to the adjoining subcells. An edge-based upwind formulation is then written as:

$$\tau_j \frac{S_j^{n+1} - S_j^n}{\Delta t} = \sum_{e=1}^{N_{edV}} \{f(S_{L_e}) F_{T_e}^+ + f(S_{R_e}) F_{T_e}^-\}, \tag{6.3.2}$$

where F_{Te} is the resultant total Darcy flux at the center of the edge e. The arrows in Figure 6.5(b) illustrate the resultant fluxes at the centre of the edges a, b, c, d and e. Here, we adopt the convention of fluxes entering (respectively leaving) the j^{th} control volume bear a positive (respectively negative) superfix.

Step II

We consider how to use the subcell velocity to improve the accuracy of the tracing vector. In the case of Cartesian grids with wave velocities having a uniform direction, the determination of the wind direction parameter (defined in the next section as χ) which

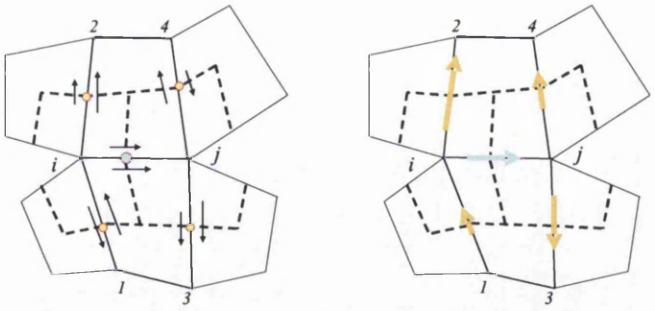

Figure 6.5: Total fluxes at the centre of edges.

dictates the upstream subcell is straightforward. However, the question of specifying a unique wave direction at the centre of the edge in the edge-based formulation arises when the flow involves variable velocity fields and/or it is resolved on unstructured grids. Two views are considered. The first approach involves using a suitable mean of the velocities

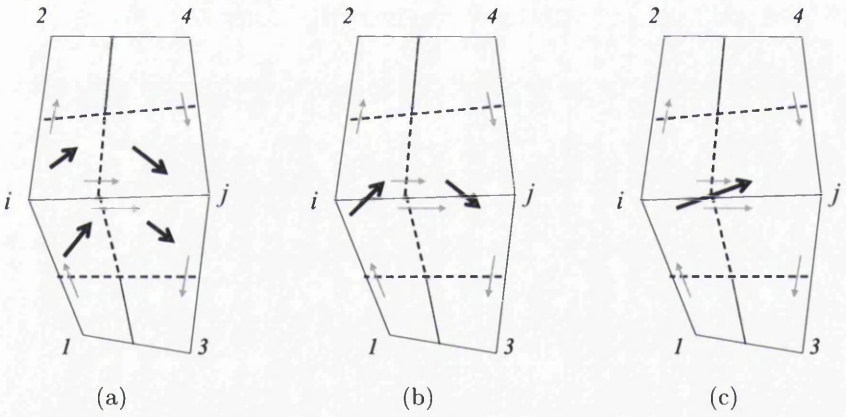

Figure 6.6: (a) Wave velocities on the subcell (black arrows) uniquely defined by the local subcell fluxes (grey arrows); (b) upstream and downstream velocity averages (black arrows) and (c) upwind velocity average.

defined on the subcells I, II, III and IV, shown in Figure 6.6(a) and define the upstream information relative to the resolving local edge subcell mean velocity as shown in Figure 6.6(c).

The second approach involves defining both the upstream velocity direction (by averaging subcell velocities I and II) and the downstream velocity direction (by averaging subcell velocities III and IV) in order to decide upon the upwind direction that provides a unique

upwind value as depicted in Figure 6.6(b).

Although practical, both approaches have been tested and shown numerically to produce spurious oscillations for cases involving strong variations in the velocity field on highly distorted grids. A stability and positivity analysis for a linear flux with variable velocity field presented below, leads to a more robust upwind formulation.

6.3.2 Formulation using Data

First, we present a family of genuinely multidimensional edge-based finite-volume schemes on unstructured quadrilateral grids using a Data based formulation. We generalize Equation (6.2.27) with respect to the key edge e and the adjacent cells sharing the edge as shown in Figure 6.4(b). The left and right multidimensional data reconstructions at the integration point on the edge $e(i,j)$ oriented from i to j are calculated as:

$$\begin{aligned} \mathbf{S}^n_{L_e} &= (1-\xi_e)\mathbf{S}^n_i + \xi_e[\chi_e \mathbf{S}^n_1 + (1-\chi_e)\mathbf{S}^n_2] \\ \mathbf{S}^n_{R_e} &= (1-\eta_e)\mathbf{S}^n_j + \eta_e[\chi_e \mathbf{S}^n_4 + (1-\chi_e)\mathbf{S}^n_3] \end{aligned} \tag{6.3.3}$$

where

$$\chi_e = \begin{cases} 1 \text{ if the wave velocity is pointing from subcell I to subcell IV,} \\ 0 \text{ if the wave velocity is pointing from subcell II to subcell III.} \end{cases} \tag{6.3.4}$$

and ξ and η denote the weighting factors where ξ (respectively η) is used to interpolate the left (respectively right) state as a linear combination of S_i (respectively S_j) and S_1 (respectively S_3) or S_2 (respectively S_4) depending on the direction of the wave speed.

Positive Linear Schemes

We will analyze the stability and consistency of the family of schemes 6.3.3 on an arbitrary unstructured quadrilateral grid for linear advection. Let N_V denote the net number of supporting vertices. Expanding Equation (6.3.2) with respect to the data yields:

$$S^{n+1}_j = \alpha_j S^n_j + \sum_{k=1, i(k)\neq j}^{N_V} \alpha_{i(k)} S^n_{i(k)}. \tag{6.3.5}$$

where α_j are the vertex support coefficients of S_j. In particular, the contributions from $cell_1$ and $cell_2$ to the control volume j essentially involve the connecting edges $e(i,j)$,

$a(3,j)$ and $b(4,j)$ (thick lines in Figure 6.7). The arrows in Figure 6.7(a) shows an illustration of the case $\chi = 1$ for the three edges. Then Equation (6.3.2) is written as:

$$\begin{aligned}\frac{\tau_j}{\Delta t}(S_j^{n+1} - S_j^n) &= F_{T_e}^+[(1-\xi_e)\mathbf{S}_i^n + \xi_e(\chi_e\mathbf{S}_1^n + (1-\chi_e)\mathbf{S}_2^n)] \\ &+ F_{T_e}^-[(1-\eta_e)\mathbf{S}_j^n + \eta_e(\chi_e\mathbf{S}_4^n + (1-\chi_e)\mathbf{S}_3^n)] \\ &+ F_{T_a}^+[(1-\xi_a)\mathbf{S}_3^n + \xi_a(1-\chi_a)\mathbf{S}_1^n] \\ &+ F_{T_a}^-[(1-\eta_a)\mathbf{S}_j^n + \eta_a\chi_a\mathbf{S}_i^n] \\ &+ F_{T_b}^+[(1-\xi_b)\mathbf{S}_4^n + \xi_b\chi_b\mathbf{S}_2^n] \\ &+ F_{T_b}^-[(1-\eta_b)\mathbf{S}_j^n + \eta_b(1-\chi_b)\mathbf{S}_i^n] + ET,\end{aligned} \tag{6.3.6}$$

where ET (extra terms) signifies any contributions coming from cells other than $cell_1$ and $cell_2$. Thus, the associated weights to the nodes i and j can be explicitly expressed as:

$$\alpha_i = \frac{\Delta t}{\tau_j}((1-\xi_e)F_{T_e}^+ + \eta_a\chi_a F_{T_a}^- + \eta_b(1-\chi_b)F_{T_b}^-), \tag{6.3.7}$$

and

$$\alpha_j = 1 + \frac{\Delta t}{\tau_j}\sum_{e=1}^{NedV}(1-\eta_e)F_{T_e}^-. \tag{6.3.8}$$

Consistency

The scheme is consistent by construction, where

$$\sum_{k=1}^{N_V}\alpha_k = 1. \tag{6.3.9}$$

Stability

The stability condition is derived from Equation (6.3.8) which shows that the scheme permits a larger CFL number than the standard upwind method if η_e are not all equal to zero.

$$\Delta t < -\frac{\tau_j}{(\sum_{e=1}^{NedV}(1-\eta_e)F_{T_e}^-)}. \tag{6.3.10}$$

This means that using directional information will enhance the stability of the method.

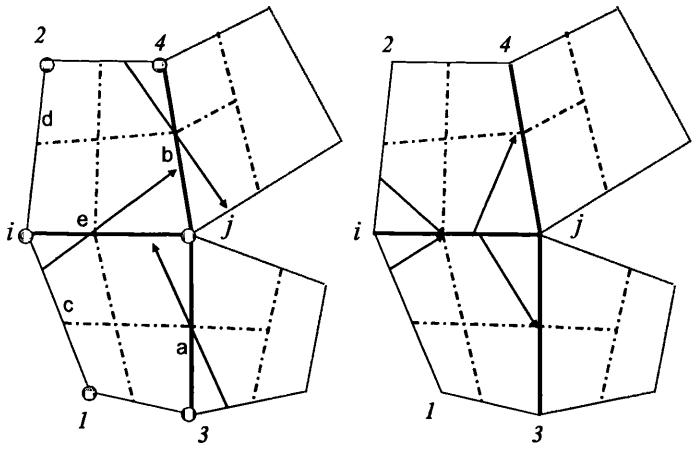

(a) (b)

Figure 6.7: (a) Wave direction orientation with respect to the key edges e, a and b (in bold) is illustrated by the arrows that correspond to $\chi_e = 1$, $\chi_a = 1$ and $\chi_b = 1$. (b) The arrows indicate possible contributions from the node i to the update of the solution control volume j.

Positivity

Recall the definition of the positivity criteria introduced in Definition 4.3.3 tailored here for the scheme Equation (6.3.5).

Definition 6.3.1 *If the scheme of Equation (6.3.5) is consistent such that Equation (6.3.9) is satisfied, stable such that the CFL condition of Equation (6.3.10) is satisfied, then the scheme of Equations (6.3.2), (6.3.3) is said to be* ***positive*** *if* $\alpha_k \geq 0$ *for all* k.

The consistency condition of Equation (6.3.9) together with positivity and the CFL condition of Equation (6.3.10) ensures that S_j^{n+1} is equal to a convex average of S_i^n for all i belonging to support of j, which leads to a positive scheme. Considering the contribution from node i in Equation (6.3.7), a necessary and sufficient condition for α_i to be positive is:

$$\xi_e F_{T_e}^+ - \chi_a \eta_a F_{T_a}^- - (1 - \chi_b)\eta_b F_{T_b}^- \leq F_{T_e}^+. \tag{6.3.11}$$

Stagnation point

This condition implies that in the case where $F_{T_e}^+ = 0$ i.e. the flux is oriented from j to i, the upwind information with respect to the edge a (respectively b) does not originate from $cell_1$ (respectively $cell_2$).

Theorem 6.3.1 *if* $F_{T_e} = F_{T_e}^+ \geq 0$ *with respect to* j, *and with respect to* i $F_{T_c} = F_{T_c}^- \leq 0$ *and* $F_{T_d} = F_{T_d}^- \leq 0$ *i.e.* F_{T_e} *is oriented from* i *to* j, F_{T_c} *is oriented from node* i *to the node* 1 *and* F_{T_d} *is oriented from node* i *to the node* 2 *as illustrated in Figure 6.8(a) then* $\xi_e = 0$.

It follows from theorem 6.3.1 that at a stagnation point the standard single-point upstream weighting scheme is recovered locally with respect to the edge $e(i,j)$.

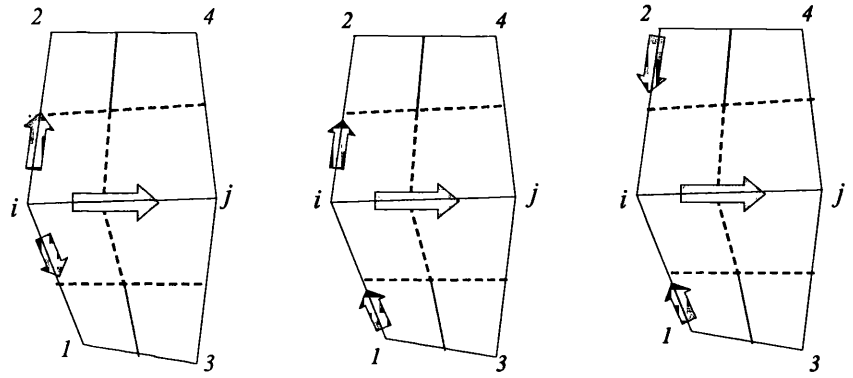

(a) Stagnation point ξ_e=0 (b) (c)

Figure 6.8: Different cases for the flow.

Proof Consider the key edge b and denote w the edge connecting j to the node u as shown in Figure 6.9 belonging to the cell adjacent to $cell_2$ and assume that the upwind information with respect to the edge b originates from this cell. Then, writing the contribution of the node u in the situation depicted in Figure 6.9 implies

$$\chi_b \eta_b F_{T_b}^- = 0. \tag{6.3.12}$$

On the other hand recall that from the expression Equation (6.3.11) related to the node i, the following condition holds:

$$(1 - \chi_b)\eta_b F_{T_b}^- = 0. \tag{6.3.13}$$

Equations (6.3.13) and (6.3.12) imply $\eta_b = 0$. In other words, at a stagnation point the standard single-point upstream weighting scheme is recovered locally with respect to the edge $b(u,j)$. Applying the same reasoning by symmetry, while considering the control volume i instead of j, this observation leads to the first constraint presented in the theorem 6.3.1, which completes the proof.

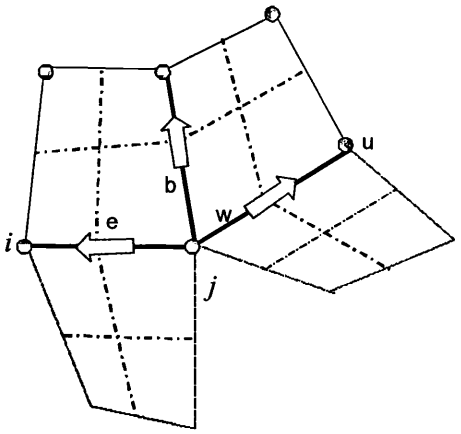

(a)

Figure 6.9: Stagnation point.

Weighting Factors

Case I In the case where $F_{T_e} > 0$, $F_{T_a} < 0$ and $F_{T_b} < 0$ i.e. F_{T_e} is oriented from i to j, F_{T_a} is oriented from node j to the node 3 and F_{T_b} is oriented from node j to the node 4 as shown in Figure 6.10(a), a sufficient condition for the inequality of Equation (6.3.11) to be satisfied is that

$$\xi_e|F_{T_e}| + \eta_a|F_{T_a}| + \eta_b|F_{T_b}| \leq |F_{T_e}|. \tag{6.3.14}$$

Setting the weights to be proportional to the ratio of the inward and outward fluxes, i.e.

$$\eta_a = \beta \min(\frac{F_{T_e}}{|F_{T_a}|}, 1), \eta_b = \beta \min(\frac{F_{T_e}}{|F_{T_b}|}, 1), \tag{6.3.15}$$

yields

$$\beta \leq \frac{1}{3} \text{ and } \xi_e \leq \frac{1}{3}. \tag{6.3.16}$$

Note here that the actual bound (of unity) on the flux ratio $\frac{F_{T_e}}{F_{T_a}}$ ($\frac{F_{T_e}}{F_{T_a}}$ respectively) is deduced from the tracing analysis limiting strategy below relative to edge a (b respectively).

Case II The condition of Equation (6.3.16) is relaxed when at least one of the fluxes F_{T_a} and F_{T_b} is non strictly negative as illustrate in Figure 6.10(b). Assume for instance that $F_{T_a} \geq 0$ i.e. F_{T_a} is pointing from node 3 to node j, thus the positivity condition of

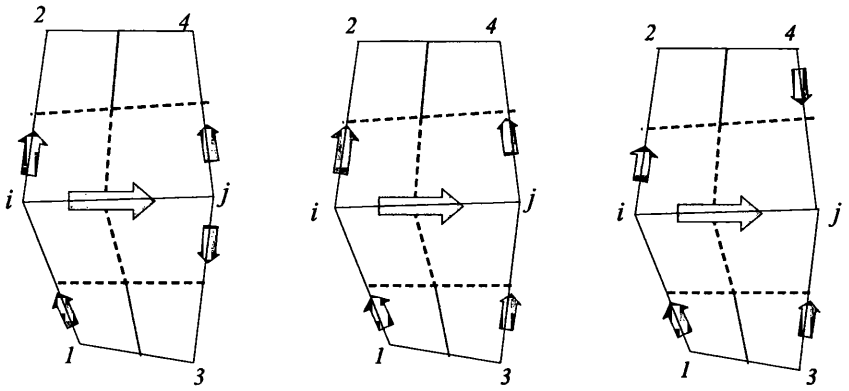

Figure 6.10: Weighting factor.

Equation (6.3.11) is satisfied for ξ_e and η_b satisfying the following inequality:

$$\xi_e + \eta_b \frac{|F_{T_b}|}{F_{T_e}} \leq 1. \tag{6.3.17}$$

A symmetric choice corresponds to

$$\xi_e \leq \frac{1}{2} \text{ and } \eta_b \leq \frac{1}{2} \min(\frac{|F_{T_e}|}{|F_{T_b}|}, 1). \tag{6.3.18}$$

Case III In the case where the fluxes $F_{T_a} \geq 0$ and $F_{T_b} \geq 0$, the positivity constraint Equation (6.3.11) is relaxed further and reduces to

$$\xi_e \leq 1. \tag{6.3.19}$$

Limiting Strategy Define the flux ratios R_{1e} and R_{2e} as:

$$R_{1e} = \frac{F_{T_c}}{F_{T_e}}, R_{2e} = \frac{F_{T_d}}{F_{T_e}}. \tag{6.3.20}$$

and let $R = \max(R_{1e}, R_{2e}, 0)$, then, the weighting factor takes the form:

$$\xi_e \leq \beta \min(1, R) \text{ with } \beta = \begin{cases} \frac{1}{3} & \text{if } F_{T_a} < 0 \text{ and } F_{T_b} < 0, \\ \frac{1}{2} & \text{otherwise} \end{cases} \tag{6.3.21}$$

Considering a positive uniform velocity field $V = (a, b)$ on Cartesian quadrilateral grid, a unit CFL condition (Equation (6.3.10)) is retrieved as the condition $\beta = \frac{1}{2}$ is always satisfied with $\xi_e = \frac{1}{2} \min(1, \frac{b}{a})$.

We also note that in case Figure 6.8(c), where both cross fluxes are entering the control volume i, the upwind subcell is selected with the edge that corresponds to a larger flux ratio in order to maximize the CFL condition of Equation (6.3.10), which may lead to a gain in accuracy. Other alternatives could be chosen such as an average between both fluxes. However, the main result of this subsection is the general limiter of Equation (6.3.21) on the angle of the characteristic/streamline to ensure positivity.

L_∞ Stability

An immediate corollary of positivity is that the scheme is stable in L_∞. Convergence follows from consistency and stability (Lax equivalence theorem for the linear case).

6.3.3 Nonlinear Formulation

For the general case, where the flux is nonlinear in saturation, we compare two formulations.

Nonlinear Flux of Multi-dimensional Data

The first formulation involves multi-dimensional upwind data correction where we define the generalized flux by:

$$\begin{aligned} f(S_L^n) &= f\big((1-\xi_e)S_i^n + \xi_e[\chi_e S_1^n + (1-\chi_e)S_2^n]\big), \\ f(S_R^n) &= f\big((1-\eta_e)S_j^n + \eta_e[\chi_e S_4^n + (1-\chi_e)S_3^n]\big). \end{aligned} \tag{6.3.22}$$

Nonlinear Multi-dimensional Flux

The second formulation involves the multi-dimensional upwind flux correction where we define the generalized flux by:

$$\begin{aligned} f(S_L^n) &= (1-\xi_e)f(S_i^n) + \xi_e[\chi_e f(S_1^n) + (1-\chi_e)f(S_2^n)], \\ f(S_R^n) &= (1-\eta_e)f(S_j^n) + \eta_e[\chi_e f(S_4^n) + (1-\chi_e)f(S_3^n)]. \end{aligned} \tag{6.3.23}$$

Here, we have used conditions Equations (6.3.4), (6.3.10) and (6.3.21) for stability in our calculations.

6.4 Numerical Test Cases

The test cases involve two phase flow (oil-water). Initial oil saturation is prescribed and water is injected. Water saturation contours are shown in each case. Solid wall (zero normal flow) boundary conditions are applied on all solid boundaries of each reservoir domain. In all cases, flow rate is specified at the (inflow) injector and pressure is prescribed at the (outflow) producer and a consistent Darcy flux approximation is used. Both distorted structured and unstructured quadrilateral grids are tested.

Results involve full tensor coefficient velocity fields, with strong cross terms that induce significant cross-flow across the cells which also adds to the full tensor effect due to the unstructured nature of the grid.

Two cases are presented. The first case is a study of a quarter five spot problem involving a linear flux whereas the second case is a study of a piston problem for nonlinear flux. The flow mobility ratio is set to $M = 1$. Both cases involve a linear or quadratic Buckley Leverett flux and a full homogeneous permeability tensor with principal axes oriented at 45 degrees to the reservoir domain with 10 to 1 anisotropy ratio. The normalized tensors have components $K_{xx} = 1.0$, $K_{yy} = 1.0$, $K_{xy} = 0.82$. The primary unknown is the (normalized) water saturation S.

6.4.1 Case 1: Linear Full Tensor Quarter Five Spot

The first case involves a linear flux, corresponding with linear relative permeabilities i.e. $k_{rw} = S$ for the water phase (w) and $k_{ro} = (1 - S)$ for the oil phase (o). Quarter five spot boundary conditions are imposed together with an anisotropic full tensor permeability field with principal axes oriented 45 degrees to the reservoir domain. The main feature of this case is the advection of the stable discontinuity across the grid. Water saturation contours are shown at 0.3 pore volumes injected (PVI) for the same CFL number equal to 0.4. The standard single-point upstream weighting results on distorted structured and unstructured quadrilateral grids are shown in Figures 6.11(b), 6.12(b) and 6.13(b). The multidimensional upwind results are shown in Figures 6.11(c), 6.12(c) and 6.13(c).

The standard scheme results show that the front is largely diffused. In contrast, the multidimensional scheme provides sharper resolution with improved symmetry of the problem, while predicting earlier breakthrough (as expected) with minimal cross-flow spread. We also note that the full-tensor effect due to the grid is noticeably attenuated in the multi-

dimensional wave oriented results.

6.4.2 Case 2: Nonlinear Full Tensor Piston Flow

The second case involves a nonlinear Buckley Leverett flow subject to fluid injection on the left hand boundary and specified pressure on the right hand boundary. The water and oil relative permeabilities are respectively $k_{rw} = S^2$ and $k_{ro} = (1 - S)^2$. The results obtained using standard single-point upstream weighting are shown in Figures 6.15(b) and 6.16(b) and those obtained using the data based multidimensional wave-oriented higher dimensional upwind scheme are shown in Figures 6.15(c) and 6.16(c). The multidimensional flux results are shown in Figures 6.15(d) and 6.16(d) on the coarse and finer unstructured grids.

The standard first order results indicate a strong grid orientation bias, whereas the results obtained with the multidimensional schemes show reduced grid dependence on the distorted unstructured meshes and provide improvement of front resolution with a clearer indication of the flow pattern, which is consistent with the problem, where the full tensor forces the flow across the domain. In addition, the multidimensional data based results show some signs of spurious oscillations on the unstructured grids in this nonlinear case, whereas the multidimensional flux results are essentially free of spurious oscillations.

6.5 Conclusions

A family of multidimensional upwind schemes is presented for hyperbolic conservation laws on structured and unstructured quadrilateral grids. The methods are locally conservative and are coupled with consistent and efficient continuous Darcy flux approximations and applied to two-phase flow problems. Positivity conditions are derived for linear convection including the CFL limits. The schemes permit higher CFL numbers than the standard upwind scheme.

Two-phase flow results are presented. Comparisons with single point upstream weighting scheme are made on a both distorted and unstructured quadrilateral grids for cases involving full tensor coefficient velocity fields. The comparisons demonstrate the benefits of the higher dimensional schemes both in terms of improved front resolution and significantly reduced cross-wind diffusion.

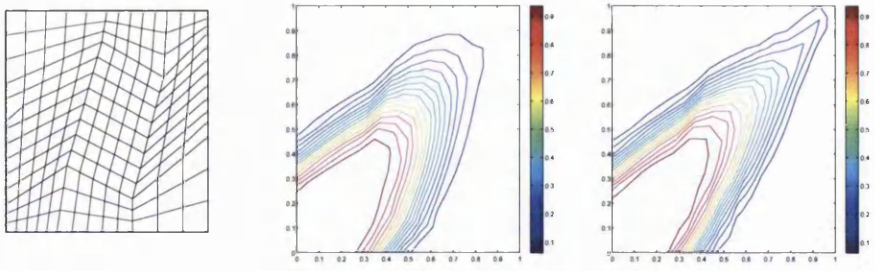

(a) (b) (c)

Figure 6.11: Case 1 - (a) Distorted coarse grid 14x15; saturation profile using (b) single-point upstream-weighting and (c) multidimensional scheme.

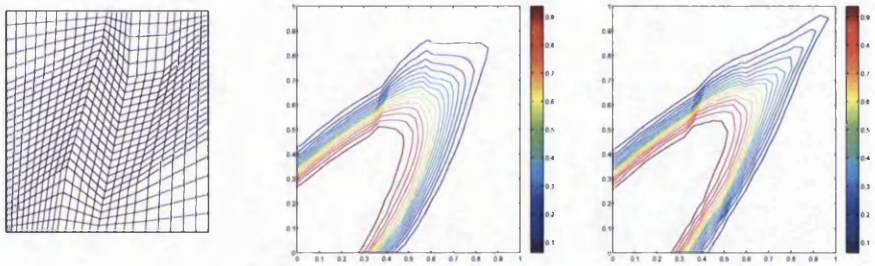

(a) (b) (c)

Figure 6.12: Case 1 - (a) Distorted finer grid 26x27; saturation profile using (b) single-point upstream-weighting and (c) multidimensional scheme.

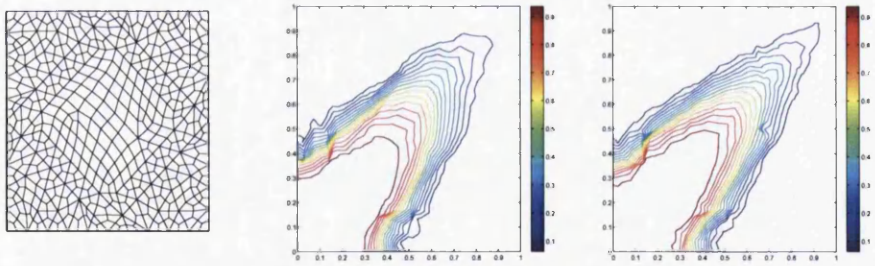

(a) (b) (c)

Figure 6.13: Case 1 - (a) Unstructured finer grid; saturation profile using (b) single-point upstream-weighting and (c) multidimensional scheme.

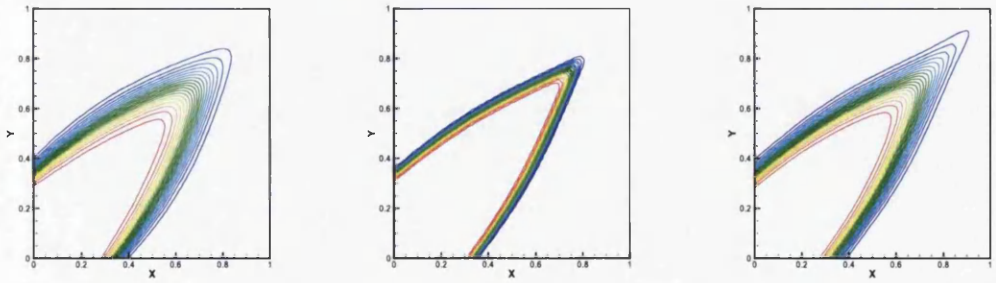

(a) (b) (c)

Figure 6.14: Case 1 - Reference solution on a 64x64 Cartesian grid using (a) single-point upstream-weighting; (b) higher-order and (c) multidimensional schemes.

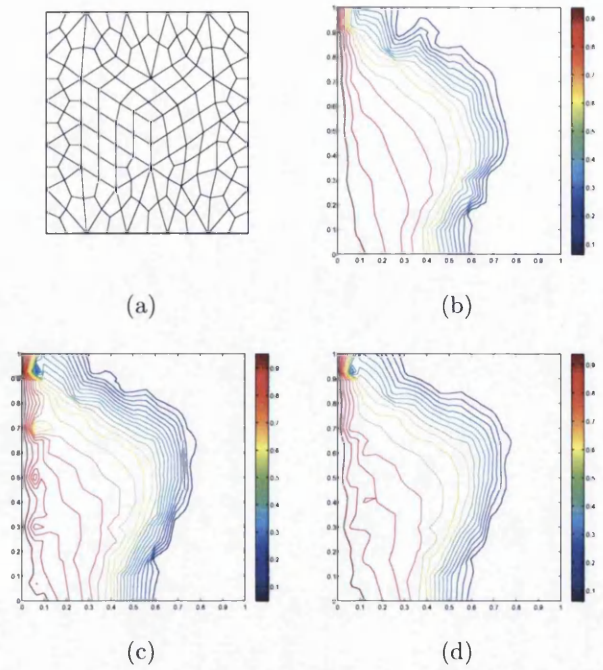

(a) (b)

(c) (d)

Figure 6.15: Case 2 - (a) Unstructured coarse grid; saturation profile using (b) single-point upstream-weighting, (c) multidimensional data based scheme and (d) multidimensional flux based scheme.

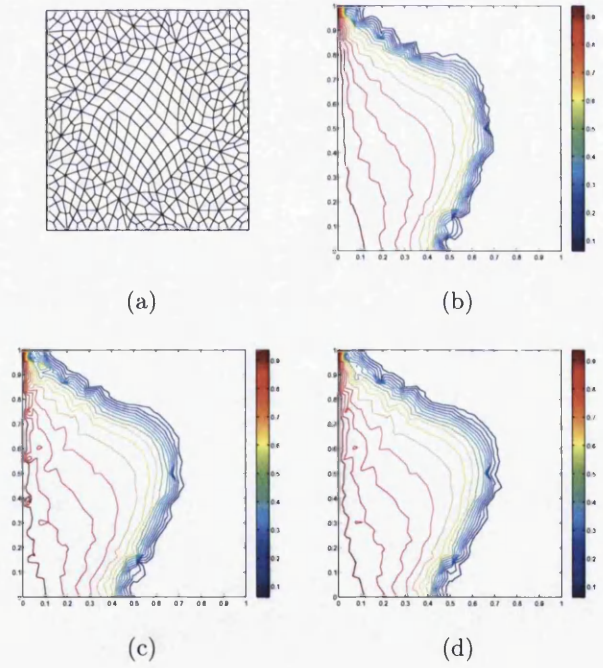

(a) (b)

(c) (d)

Figure 6.16: Case 2 - (a) Unstructured finer grid; saturation profile using (b) single-point upstream-weighting, (c) multidimensional data based scheme and (d) multidimensional flux based scheme.

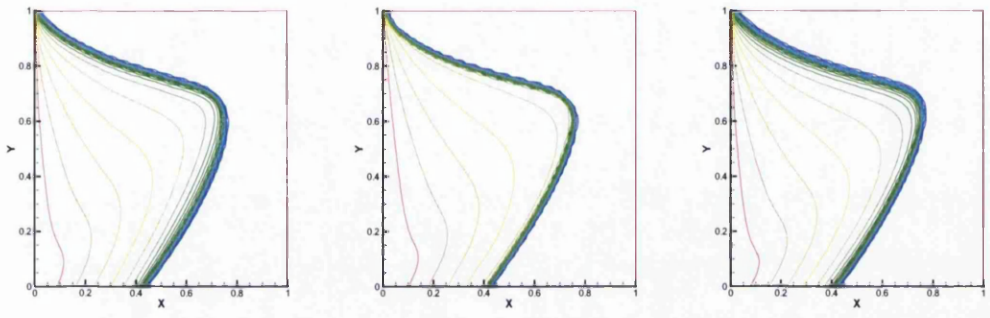

(a) (b) (c)

Figure 6.17: Case 2 - Reference solution on a 64x64 Cartesian grid using (a) single-point upstream-weighting; (b) higher-order and (c) multidimensional schemes.

Chapter 7

Multidimensional Schemes on Triangular and Hybrid Grids

In this chapter, formulation of the edge-based family of multi-dimensional schemes on unstructured triangular grids and hybrid grids consisting of triangles and quadrilaterals is presented. Two-phase flow results are presented in section 7.3 that demonstrate the advantages of the new higher dimensional flux-continuous formulations.

7.1 A Family of Edge-based Higher Dimensional Schemes on Triangular Grids

The focus here is on reducing cross-wind diffusion on triangular grids. The main idea of the multidimensional triangular scheme is to trace back along the two-dimensional characteristic to the point of intersection with the upwind co-ordinate lines whenever possible as with the quadrilateral multidimensional scheme. The formulation begins with the same two issues as for quadrilateral meshes (chapter 6, section 6.3) as the upwind direction is based on the local wave velocity which is defined over the subcells.
Discretisation of Equation (4.2.16) is expressed again as:

$$\tau_j \frac{S_j^{n+1} - S_j^n}{\Delta t} = - \sum_{e=1}^{N_{edV}} \mathrm{f}(S_{L_e}, S_{R_e}) \sum_{i_q=1}^{N_q} F_{T_q}, \tag{7.1.1}$$

as in the quadrilateral formulation c.f. section 6.3.1.

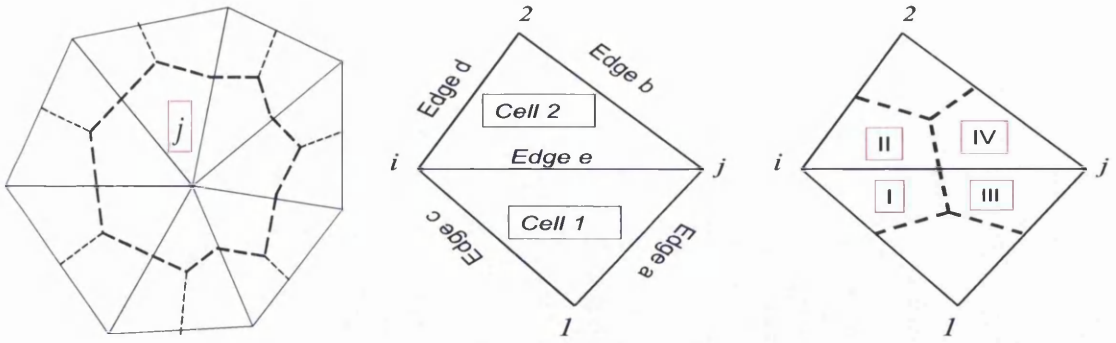

(a) (b) (c)

Figure 7.1: (a) Control volume (dashed line) (b) compact stencil (b) subcells.

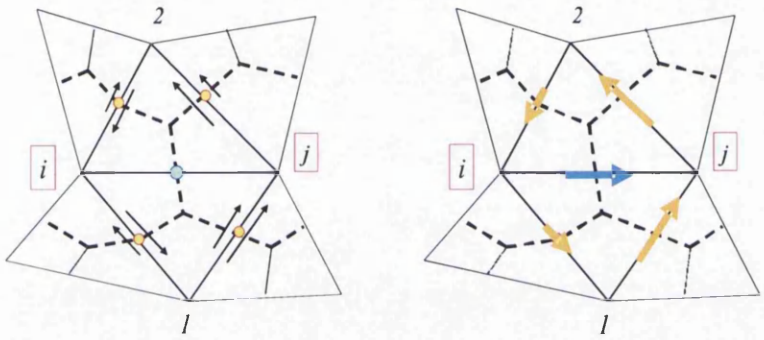

(a) (b)

Figure 7.2: Total fluxes at the centre of edges.

7.1.1 Formulation using Data

A family of genuinely multidimensional triangular edge-based finite-volume schemes using a data based formulation is first presented. As for the quadrilateral meshes, the key edge e and the adjacent cells sharing the edge as shown in Figure 7.1(b), then the left and right states at the integration point on the edge $e(i,j)$ oriented from i to j are computed as:

$$\begin{aligned} \mathbf{S}^n_{L_e} &= (1-\xi_e)\mathbf{S}^n_i + \xi_e[\chi_e \mathbf{S}^n_1 + (1-\chi_e)\mathbf{S}^n_2] \\ \mathbf{S}^n_{R_e} &= (1-\eta_e)\mathbf{S}^n_j + \eta_e[\chi_e \mathbf{S}^n_2 + (1-\chi_e)\mathbf{S}^n_1] \end{aligned} \tag{7.1.2}$$

where

$$\chi_e = \begin{cases} 1 \text{ if the wave velocity is pointing from subcell I to subcell IV,} \\ 0 \text{ if the wave velocity is pointing from subcell II to subcell III.} \end{cases} \quad (7.1.3)$$

and $0 \leq \xi \leq 1$ and $0 \leq \eta \leq 1$ denote the weighting factors where ξ (η respectively) is used to interpolate the left (right respectively) state as a linear combination of S_i (S_j respectively) and S_1 (S_2 respectively) or S_2 (S_1 respectively) depending on the direction of the wave speed.

Two Dimensional Analysis

We will first analyze the stability and consistency of the scheme on a uniform triangular grid as shown in Figure 7.3 for linear advection with constant wave velocity $\mathbf{V}$. In this example case $i = 2$, $j = 0$ and $\mathbf{S}_2^n$ is replaced by $\mathbf{S}_3^n$ in Equation (7.1.2). Define SL_{0i} for

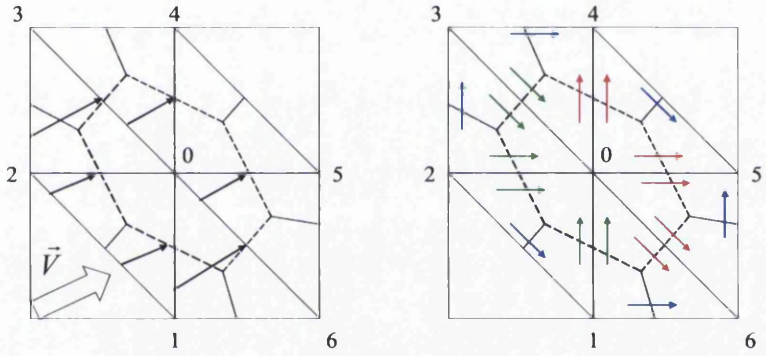

(a) (b)

Figure 7.3: Positivity analysis for a uniform velocity case (a) stencil and streamlines (b) Flux directions.

$i = 1, 2, 3$ and SL_{0i} for $i = 4, 5, 6$ as the left and right states at the edge $(i, 0)$ oriented from i to 0 and S_i is the saturation value at the node i. Therefore, the left and right

states are written as:

$$\begin{aligned} S_{L01} &= (1-\xi_{01})S_1 + \xi_{01}S_2, \\ S_{L02} &= (1-\xi_{02})S_2 + \xi_{02}S_1, \\ S_{L03} &= (1-\xi_{03})S_3 + \xi_{03}S_2, \\ S_{R04} &= (1-\eta_{04})S_0 + \eta_{04}S_3, \\ S_{R05} &= (1-\eta_{05})S_0 + \eta_{05}S_6, \\ S_{R06} &= (1-\eta_{06})S_0 + \eta_{06}S_1. \end{aligned} \tag{7.1.4}$$

Let $\mathbf{n_{0i}}$ denote the normal to the control volume face corresponding with the edge $e(0,i)$ for $i = 1..6$. Also let $F_{0i} = \mathbf{V}\cdot\mathbf{n_{0i}}$. Then, assembling the fluxes with regards to the control volume 0 yields:

$$\begin{aligned} S_0^{n+1} &= [1 - \frac{\Delta t}{\tau_0}((1-\eta_{04})|F_{04}| + (1-\eta_{05})|F_{05}| + (1-\eta_{06})|F_{06}|)]S_0^n \\ &+ \frac{\Delta t}{\tau_0}[(1-\xi_{01})|F_{01}| + \xi_{02}|F_{02}| - \eta_{06}|F_{06}|]S_1^n \\ &+ \frac{\Delta t}{\tau_0}[(1-\xi_{02})|F_{02}| + \xi_{01}|F_{01}| + \xi_{03}|F_{03}|]S_2^n \\ &+ \frac{\Delta t}{\tau_0}[(1-\xi_{03})|F_{03}| - \eta_{04}|F_{04}|]S_3^n \\ &- \frac{\Delta t}{\tau_0}\eta_{05}|F_{05}|S_6^n. \end{aligned} \tag{7.1.5}$$

From Equation (7.1.5), note that coefficients sum to unity. A necessary condition for the scheme to be positive is that all the coefficients are positive namely:

$$\begin{aligned} 1 - \frac{\Delta t}{\tau_0}((1-\eta_{04})|F_{04}| + (1-\eta_{05})|F_{05}| + (1-\eta_{06})|F_{06}|) &\geq 0, \\ (1-\xi_{01})|F_{01}| + \xi_{02}|F_{02}| - \eta_{06}|F_{06}| &\geq 0, \\ (1-\xi_{02})|F_{02}| + \xi_{01}|F_{01}| + \xi_{03}|F_{03}| &\geq 0, \\ (1-\xi_{03})|F_{03}| - \eta_{04}|F_{04}| &\geq 0, \\ -\frac{\Delta t}{\tau_0}\eta_{05}|F_{05}| &\geq 0. \end{aligned} \tag{7.1.6}$$

Note that the third inequality in Equations (7.1.6), is satisfied provided that ξ_{0i} and η_{0i} are such that the interpolation is convex between each pair of nodes 0 and i for $i = 1..6$. The last inequality implies

$$\eta_{05} = 0. \tag{7.1.7}$$

This motivated the analysis of stagnation points when unstructured grids are considered. As a consequence the multidimensional scheme locally reduces to a standard first order reconstruction at the edge joining the nodes 0 and 5.
Taking this condition into account, the first inequality is written as

$$1 + \frac{\Delta t}{\tau_0}(\eta_{04}|F_{04}| + \eta_{06}|F_{06}|) - \frac{\Delta t}{\tau_0}(|F_{04}| + |F_{05}| + |F_{06}|) \geq 0. \tag{7.1.8}$$

and is clearly positive for higher CFL numbers than the standard upstream weighting scheme. The second and fourth inequalities are equivalent to

$$\begin{aligned} \xi_{01}|F_{01}| + \eta_{06}|F_{06}| &\leq |F_{01}| + \xi_{02}|F_{02}|, \\ \xi_{03}|F_{03}| + \eta_{04}|F_{04}| &\leq |F_{03}|, \end{aligned} \tag{7.1.9}$$

and define a family of multidimensional schemes.

Theorem 7.1.1 *There exist non negative coefficients $\xi_{01}, \xi_{03}, \xi_{02}$ and η_{04}, η_{06} that satisfy the inequalities in Equations (7.1.9) and the choice of these parameters is non unique. Also, equations (7.1.5) and (7.1.4) define a family of linear positive and consistent genuinely multidimensional schemes for this section under the conditions Equations (7.1.9), (7.1.7) and (7.1.8).*

Proof The node contributions in Equation (7.1.5) sum to one by construction and are positive for a choice that uses locally the upwind and downwind flux information corresponding to

$$\eta_{06} = \frac{1}{2}\frac{F_{01}}{F_{06}}\ ,\ \xi_{01} \leq \frac{1}{2}\ ,\ \xi_{02} \leq 1$$

and

$$\eta_{04} = \frac{1}{2}\frac{F_{03}}{F_{04}}\ ,\ \xi_{03} \leq \frac{1}{2}.$$

Note here that this choice is non symmetric and uses a local stencil.

Unlike the analysis performed on Cartesian grids (chapter 6, section 6.2.3) that deals with the node contribution, the discussion presented here makes use of the full stencil and motivates the following analysis on unstructured triangular meshes.

Positive Linear Schemes on Unstructured Triangular Schemes

The stability analysis of the family of schemes Equations (7.1.2) on an arbitrary unstructured triangular grid for linear advection is closely related to the positivity analysis on quadrilateral meshes presented in chapter 6, section 6.3.1. Again, we start by expanding Equation (7.1.1) with respect to the data yielding:

$$S_j^{n+1} = \alpha_j S_j^n + \sum_{k=1, i(k)\neq j}^{N_V} \alpha_{i(k)} S_{i(k)}^n. \tag{7.1.10}$$

where α_i are the vertex support coefficients of S_i and N_V is net number of supporting vertices. The arrows in Figure 7.4(a) shows an illustration of the case $\chi = 1$ for the three

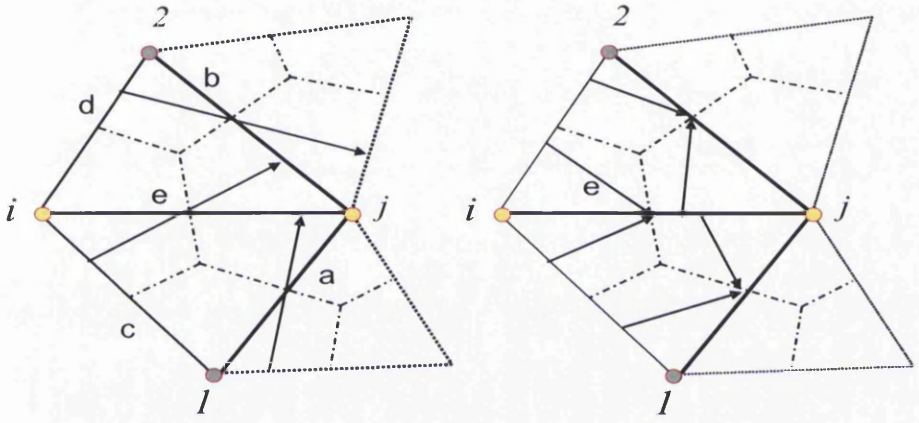

(a) (b)

Figure 7.4: (a) Wave direction orientation with respect to the key edges e, a and b (in bold) is given by the arrows that correspond to χ equals one. (b) Contributions from the node i.

edges. Then Equation (7.1.1) is written as:

$$\begin{aligned}
\frac{\tau_j}{\Delta t}(S_j^{n+1} - S_j^n) &= F_{T_e}^+[(1-\xi_e)\mathbf{S}_i^n + \xi_e(\chi_e \mathbf{S}_1^n + (1-\chi_e)\mathbf{S}_2^n)] \\
&+ F_{T_e}^-[(1-\eta_e)\mathbf{S}_j^n + \eta_e(\chi_e \mathbf{S}_2^n + (1-\chi_e)\mathbf{S}_1^n)] \\
&+ F_{T_a}^+[(1-\xi_a)\mathbf{S}_1^n + \xi_a(1-\chi_a)\mathbf{S}_i^n] \\
&+ F_{T_a}^-[(1-\eta_a)\mathbf{S}_j^n + \eta_a\chi_a\mathbf{S}_i^n] \\
&+ F_{T_b}^+[(1-\xi_b)\mathbf{S}_2^n + \xi_b\chi_b\mathbf{S}_i^n] \\
&+ F_{T_b}^-[(1-\eta_b)\mathbf{S}_j^n + \eta_b(1-\chi_b)\mathbf{S}_i^n] + ET
\end{aligned} \tag{7.1.11}$$

where ET (extra terms) signifies any contributions coming from cells other than $cell_1$ and $cell_2$ and the associated weights to the node i is written as:

$$\alpha_i = \frac{\Delta t}{\tau_j}((1-\xi_e)F^+_{T_e} + \xi_a(1-\chi_a)F^+_{T_a} + \xi_b\chi_b F^+_{T_b} + \eta_a\chi_a F^-_{T_a} + \eta_b(1-\chi_b)F^-_{T_b}), \quad (7.1.12)$$

which is different than the quadrilateral case Equation (6.3.7) as it involves two extra positive terms that account for the contributions of the nodes 1 and 2. The associated weight to the central node j is expressed as

$$\alpha_j = 1 + \frac{\Delta t}{\tau_j}\sum_{e=1}^{NedV}(1-\eta_e)F^-_{T_e} \quad (7.1.13)$$

and implies a larger allowable time step than the standard first order single point upstream weighting scheme for non-vanishing η.

Also, the multidimensional triangular approximation is consistent by construction in the sense that the coefficients α_k sum to unity.

Considering the contribution from node i in Equation (7.1.12), a necessary and sufficient condition for α_i to be positive is:

$$\xi_e F^+_{T_e} - \chi_a\eta_a F^-_{T_a} - (1-\chi_b)\eta_b F^-_{T_b} \leq F^+_{T_e} + \xi_a(1-\chi_a)F^+_{T_a} + \xi_b\chi_b F^+_{T_b}. \quad (7.1.14)$$

It is clear that this condition is less restrictive than than the key constraint 6.3.11 derived for quadrilateral grids. The stability of the multidimensional scheme is enhanced by the positive contributions of the fluxes $F^+_{T_a}$ and $F^+_{T_b}$ on the right hand side of the inequality. A sufficient condition which is applicable in the general case is used in the rest of this analysis and is written as:

$$\xi_e F^+_{T_e} - \chi_a\eta_a F^-_{T_a} - (1-\chi_b)\eta_b F^-_{T_b} \leq F^+_{T_e}. \quad (7.1.15)$$

This implies that in the case where $F^+_{T_e} = 0$ i.e. the flux is oriented from j to i, the upwind information with respect to the edge a (b respectively) does not originate from $cell_1$ ($cell_2$ respectively). Equation (7.1.14) reduces then to:

$$-\eta_a F^-_{T_a} - \eta_b F^-_{T_b} \leq 0. \quad (7.1.16)$$

assuming that $\chi_a = 1$ and $\chi_b = 0$. Positivity condition requires $\eta_a = 0$ and $\eta_b = 0$ in the case where $F_{T_a} < 0$ and $F_{T_b} < 0$.

Applying the same reasoning while considering the control volume i instead of control volume j, this observation leads to the first constraint at a stagnation point as for quadrilateral grids namely:

Theorem 7.1.2

if $F_{T_e} \geq 0$ with respect to j, and with respect to i $F_{T_c} \leq 0$ and $F_{T_d} \leq 0$ i.e. F_{T_e} is oriented from i to j, F_{T_c} is oriented from node i to the node 1 and F_{T_d} is oriented from node i to the node 2 as illustrated in Figure 7.5(a) then $\xi_e = 0$. This means that at a stagnation point the standard single-point upstream weighting scheme is recovered locally with respect to the edge $e(i,j)$.

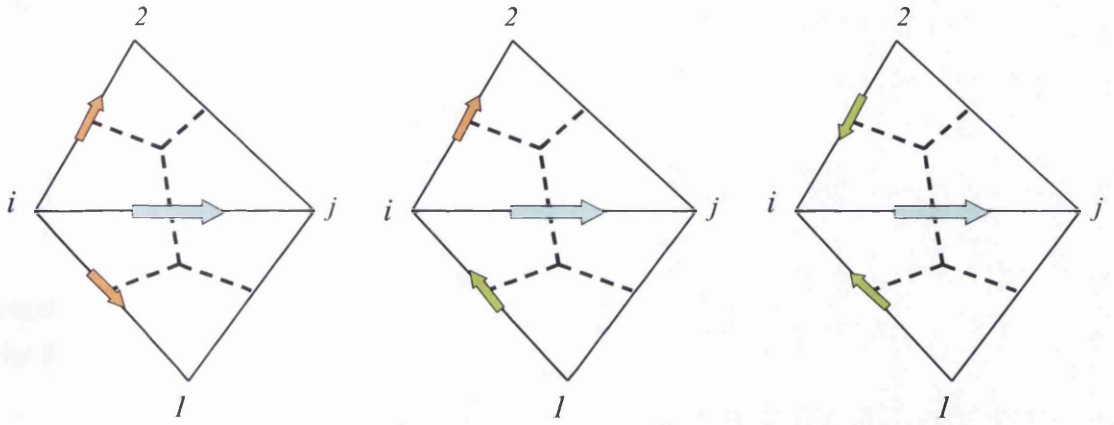

Figure 7.5: Different cases for the flow

On the other hand, in the case where $F_{T_e} > 0$, $F_{T_a} < 0$ and $F_{T_b} < 0$ i.e. F_{T_e} is oriented from i to j, F_{T_a} is oriented from node j to the node 1 F_{T_b} is oriented from node j to the node 2 as shown in Figure 7.6(a), a sufficient condition for the inequality 7.1.15 to be satisfied is that

$$\xi_e|F_{T_e}| + \eta_a|F_{T_a}| + \eta_b|F_{T_b}| \leq |F_{T_e}|. \tag{7.1.17}$$

Setting the weights to be proportional to the ratio of the inward and outward fluxes, i.e.

$$\eta_a = \beta \min(\frac{F_{T_e}}{|F_{T_a}|}, 1), \eta_b = \beta \min(\frac{F_{T_e}}{|F_{T_b}|}, 1), \tag{7.1.18}$$

yields

$$\beta \leq \frac{1}{3} \text{ and } \xi_e \leq \frac{1}{3}. \tag{7.1.19}$$

Again, the actual bound (of unity) on the flux ratio $\frac{F_{T_e}}{F_{T_a}}$ ($\frac{F_{T_e}}{F_{T_a}}$ respectively) is deduced from the tracing analysis relative to edge a (b respectively). Note here that the condition Equation (7.1.19) is relaxed when at least one of the fluxes F_{T_a} and F_{T_b} is non strictly

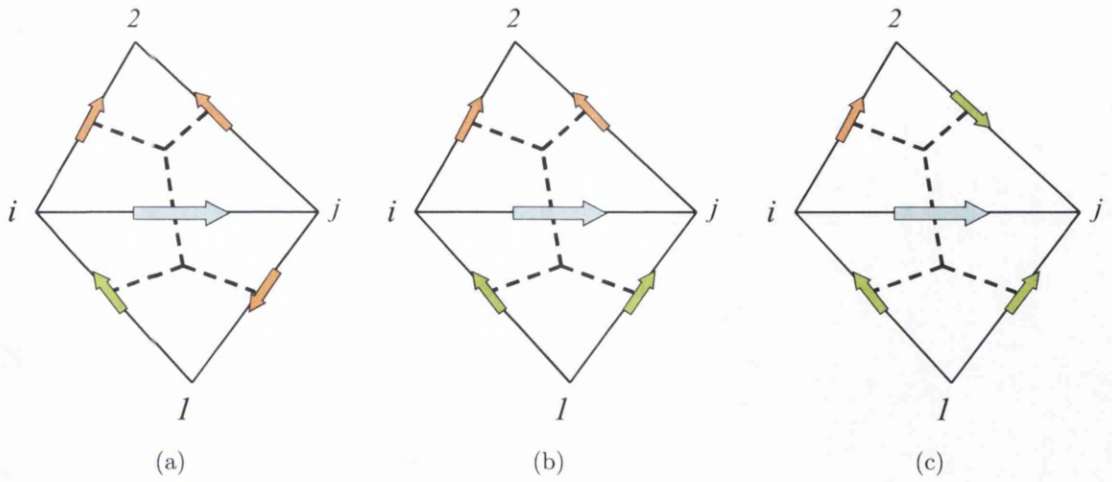

Figure 7.6: Weighting factor

negative (Figure 7.6(b)) and the inequality 7.1.19 becomes $\beta \leq \frac{1}{2}$. Furthermore, define the flux ratios R_{1e} and R_{2e} as:

$$R_{1e} = \frac{F_{T_c}}{F_{T_e}}, R_{2e} = \frac{F_{T_d}}{F_{T_e}}. \tag{7.1.20}$$

and let $R = \max(R_{1e}, R_{2e}, 0)$, then, the weighting factor takes the form:

$$\xi_e \leq \beta \min(1, R) \text{ with } \beta = \begin{cases} \frac{1}{3} & \text{if } F_{T_a} < 0 \text{ and } F_{T_b} < 0, \\ \frac{1}{2} & \text{otherwise} \end{cases} \tag{7.1.21}$$

Other alternatives could be chosen such as an average between both fluxes e.g.

$$R_{1e} = \frac{F_{T_c}^+}{F_{T_e}^+ + F_{T_c}^+}, R_{2e} = \frac{F_{T_d}^+}{F_{T_e}^+ + F_{T_d}^+}. \tag{7.1.22}$$

which leads to $\xi_e \leq \beta R$ with β and R defined as above in Equation (7.1.21).
Also we note that in case Figure 7.6(c), where both cross fluxes are entering the control volume i, the upwind subcell is selected with the edge that corresponds to a larger flux ratio in order to maximize the CFL condition, which may lead to a gain in accuracy. However, the main result of this subsection is the general limiter of Equation (7.1.21) on the angle of the characteristic/streamline to ensure positivity.

7.1.2 Nonlinear Formulation

As for the quadrilateral counterpart, we compare two formulations taking into account the general case where the flux is nonlinear in saturation.

Nonlinear Flux of Multi-dimensional Data

The first formulation involves multi-dimensional upwind data correction where we define the generalized flux by:

$$\begin{aligned} f(S_L^n) &= f\big((1-\xi_e)S_i^n + \xi_e[\chi_e S_1^n + (1-\chi_e)S_2^n]\big), \\ f(S_R^n) &= f\big((1-\eta_e)S_j^n + \eta_e[\chi_e S_2^n + (1-\chi_e)S_1^n]\big). \end{aligned}$$

Nonlinear Multi-dimensional Flux

The second formulation involves the multi-dimensional upwind flux correction where we define the generalized flux by:

$$\begin{aligned} f(S_L^n) &= (1-\xi_e)f(S_i^n) + \xi_e[\chi_e f(S_1^n) + (1-\chi_e)f(S_2^n)], \\ f(S_R^n) &= (1-\eta_e)f(S_j^n) + \eta_e[\chi_e f(S_2^n) + (1-\chi_e)f(S_1^n)]. \end{aligned}$$

Here, we have used conditions of Equations (7.1.3), (6.3.10) and (7.1.21) for stability in our calculations.

7.2 Edge-based Multidimensional Schemes On Hybrid Meshes In 2-D

For completeness, the multidimensional edge based formulation is presented in this section for unstructured hybrid meshes. The notation used here is adopted in the next chapters.

7.2.1 Formulation using Data

Consider the key edge e and the adjacent cells sharing the edge as shown in Figure 7.7(b), then the left and right states at the integration point on the edge $e(i,j)$ oriented from i to j are calculated as:

$$\begin{aligned} \mathbf{S}_{L_e}^n &= (1-\xi_e)\mathbf{S}_i^n + \xi_e[\chi_e \mathbf{S}_1^n + (1-\chi_e)\mathbf{S}_2^n] \\ \mathbf{S}_{R_e}^n &= (1-\eta_e)\mathbf{S}_j^n + \eta_e[\chi_e \mathbf{S}_4^n + (1-\chi_e)\mathbf{S}_3^n] \end{aligned} \tag{7.2.1}$$

where

$$\chi_e = \begin{cases} 1 \text{ if the wave velocity is pointing from subcell I to subcell IV,} \\ 0 \text{ if the wave velocity is pointing from subcell II to subcell III.} \end{cases} \tag{7.2.2}$$

and $0 \leq \xi \leq 1$ and $0 \leq \eta \leq 1$ denote the weighting factors where ξ (respectively η) is used to interpolate the left (respectively right) state as a linear combination of S_i (respectively S_j) and S_1 (respectively S_3) or S_2 (respectively S_4) depending on the direction of the wave speed. Note here that node 1 and 3 coincide.

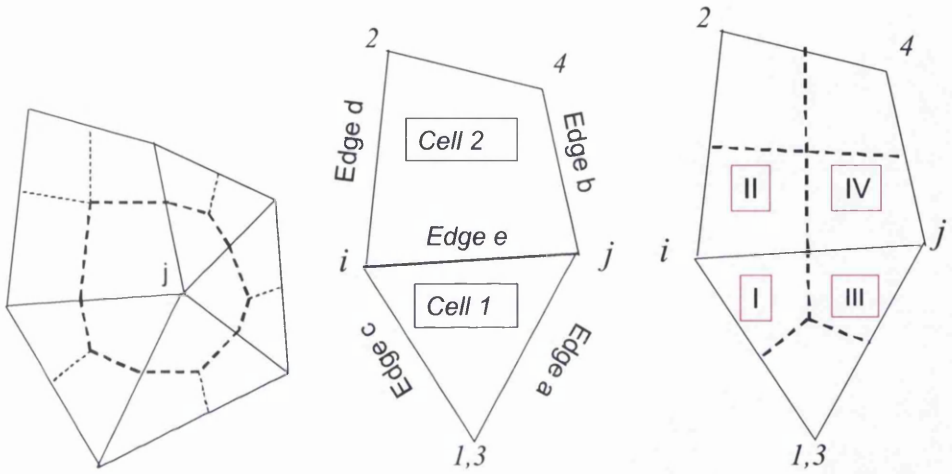

(a) (b) (c)

Figure 7.7: (a) Control volume (dashed line) (b) compact stencil (b) subcells.

7.2.2 Positive Linear Schemes

In this section, we will analyze the stability and consistency of the family of schemes defined by Equations (7.1.1), (7.2.2) and (7.2.1) for linear advection on an arbitrary unstructured grid comprised of triangles and quadrilaterals. The discretisation using the multidimensional edge based scheme of Equation (7.1.1) on the unstructured grid Figure 7.7 with respect to the control volume j is similar to 9.1.16 and 9.1.5 and now takes the form:

$$\begin{aligned}
\frac{\tau_j}{\Delta t}(S_j^{n+1} - S_j^n) &= F_{T_e}^+[(1-\xi_e)\mathbf{S}_i^n + \xi_e(\chi_e\mathbf{S}_1^n + (1-\chi_e)\mathbf{S}_2^n)] \\
&+ F_{T_e}^-[(1-\eta_e)\mathbf{S}_j^n + \eta_e(\chi_e\mathbf{S}_4^n + (1-\chi_e)\mathbf{S}_1^n)] \\
&+ F_{T_a}^+[(1-\xi_a)\mathbf{S}_1^n + \xi_a(1-\chi_a)\mathbf{S}_i^n] \\
&+ F_{T_a}^-[(1-\eta_a)\mathbf{S}_j^n + \eta_a\chi_a\mathbf{S}_i^n] \\
&+ F_{T_b}^+[(1-\xi_b)\mathbf{S}_4^n + \xi_b\chi_b\mathbf{S}_2^n] \\
&+ F_{T_b}^-[(1-\eta_b)\mathbf{S}_j^n + \eta_b(1-\chi_b)\mathbf{S}_i^n] + ET
\end{aligned} \tag{7.2.3}$$

where the same notation as in 7.1 is adopted and ET (extra terms) denote the contributions coming from cells other than $cell_1$ and $cell_2$. The coefficient of node i, α_i then takes the form:

$$\alpha_i = \frac{\Delta t}{\tau_j}((1-\xi_e)F_{T_e}^+ + \xi_a(1-\chi_a)F_{T_a}^+ + \eta_a\chi_a F_{T_a}^- + \eta_b(1-\chi_b)F_{T_b}^-). \tag{7.2.4}$$

As for triangular and quadrilateral grids, the scheme is consistent by construction and the positivity limit is

$$\xi_e F_{T_e}^+ - \eta_a\chi_a F_{T_a}^- - \eta_b(1-\chi_b)F_{T_b}^- \leq F_{T_e}^+ + \xi_a(1-\chi_a)F_{T_a}^+, \tag{7.2.5}$$

that reduces to

$$\xi_e F_{T_e}^+ - \eta_a\chi_a F_{T_a}^- - \eta_b(1-\chi_b)F_{T_b}^- \leq F_{T_e}^+. \tag{7.2.6}$$

7.2.3 Stagnation Point

The most restrictive case corresponds to $F_{T_e}^+ = 0, F_{T_a}^- < 0$ and $F_{T_b}^- < 0$ where the postivity condition Equation (7.2.5) reduces to

$$-\eta_a F_{T_a}^- - \eta_b F_{T_b}^- = 0 \tag{7.2.7}$$

for $\chi_a = 0$ and $\chi_b = 1$ and yields $\eta_a = 0$ and $\eta_b = 0$.

Theorem 7.2.1

if $F_{T_e} \geq 0$ with respect to node j, and with respect to node i $F_{T_c} < 0$ and $F_{T_d} < 0$ i.e. F_{T_e} is oriented from i to j, F_{T_c} is oriented from node i to the node 1 and F_{T_d} is oriented from node i to the node 2 as illustrated in Figure 7.8(a) then $\xi_e = 0$. This means that at a stagnation point the standard single-point upstream weighting scheme is recovered locally with respect to the edge $e(i,j)$.

Proof c.f. Proof 6.3.2 based on Equation (7.2.6).

7.2.4 Weighting Factors

The derivation of the weighting factors follows the same reasoning as for the triangular grids section 7.1. In the case where $F_{T_e} = F_{T_e}^+ > 0$, $F_{T_a} = F_{T_a}^- < 0$ and $F_{T_b} = F_{T_b}{}^- < 0$ i.e. F_{T_e} is oriented from i to j, F_{T_a} is oriented from node j to the node 3 F_{T_b} is oriented from

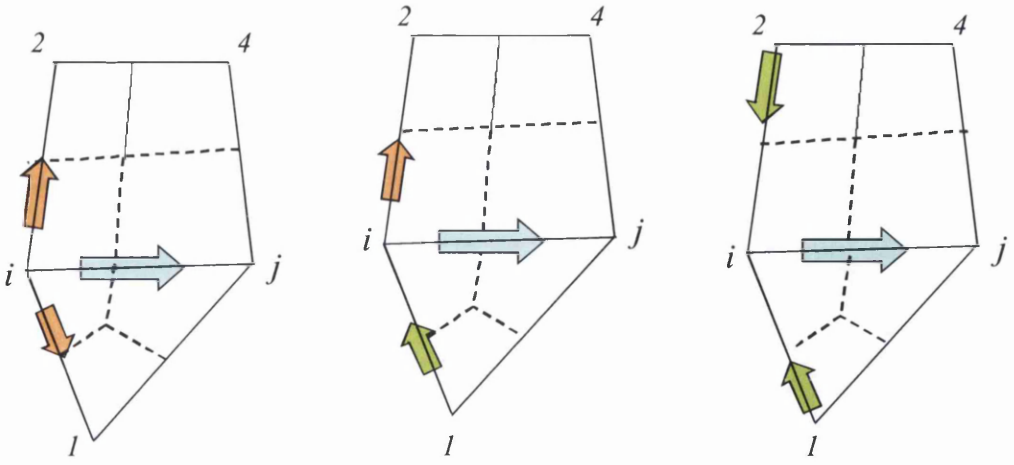

(a) (b) (c)

Figure 7.8: Different cases for the flow

node j to the node 4 as shown in Figure 7.9(a), a sufficient condition for the inequality in Equation (7.2.5) to be satisfied is that

$$\xi_e|F_{T_e}| + \eta_a|F_{T_a}| + \eta_b|F_{T_b}| \leq |F_{T_e}|. \tag{7.2.8}$$

Setting the weights to be proportional to the ratio of the inward and outward fluxes, i.e.

$$\eta_a = \beta \min(\frac{F_{T_e}}{F_{T_a}}, 1), \eta_b = \beta \min(\frac{F_{T_e}}{F_{T_b}}, 1), \tag{7.2.9}$$

yields

$$\beta \leq \frac{1}{3}. \tag{7.2.10}$$

Again, the condition of Equation (7.2.10) is relaxed when at least one of the fluxes F_{T_a} and F_{T_b} is positive Figure 7.9(b) and the inequality in Equation (7.2.10) becomes

$$\beta \leq \frac{1}{2}. \tag{7.2.11}$$

Furthermore, define flux ratios R_{1e} and R_{2e} as:

$$R_{1e} = \frac{F_{T_c}}{F_{T_e}}, R_{2e} = \frac{F_{T_d}}{F_{T_e}}. \tag{7.2.12}$$

and let $R = \max(R_{1e}, R_{2e}, 0)$, then, the weighting factor takes the form:

$$\xi_e \leq \beta \min(1, R) \text{ with } \beta = \begin{cases} \frac{1}{3} & \text{if } F_{T_a} < 0 \text{ and } F_{T_b} < 0, \\ \frac{1}{2} & \text{otherwise} \end{cases} \tag{7.2.13}$$

For non-linear fluxes, the edge based multidimensional schemes are defined as in section 6.3.3.

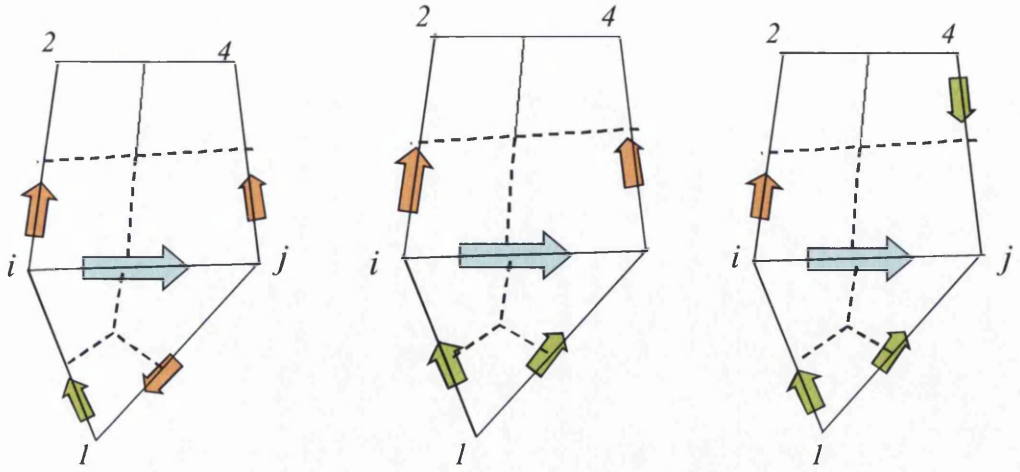

(a) (b) (c)

Figure 7.9: Weighting factor

7.3 Numerical Results

The test cases involve two phase flow (oil-water). Initial oil saturation is prescribed and water is injected. Water saturation contours are shown in each case. Solid wall (zero normal flow) boundary conditions are applied on all solid boundaries of each reservoir domain. In all cases, flow rate is specified at the (inflow) injector and pressure is prescribed at the (outflow) producer and a consistent Darcy flux approximation is used. Both regular and distorted unstructured triangular grids are tested. Results involve full-tensor coefficient velocity fields due to the grid or permeability field (or both), with strong cross-terms that induce significant cross-flow across grid cells which adds to the full-tensor effect due to the unstructured nature of the grid.

7.3.1 Case 1: Linear Piston Buckley Leverett Flow

The first case is a study of a linear flow problem using a triangular grid shown in Figure 7.10(a) as in case 1 presented in chapter 5 section 5.4.1. Here, water saturation contours are shown at 0.5 pore volumes injected (PVI). The first result, Figure 7.10(b), shows the effect of employing the standard first order upwind scheme for the convective flux approximation. The multidimensional scheme result is shown in Figure 7.10(c). The first order scheme result shows a strong dependency on the grid structure. The multidi-

mensional scheme provides considerable improvement in the resolution of the saturation front compared to the standard scheme and is independent of the grid structure for this case.

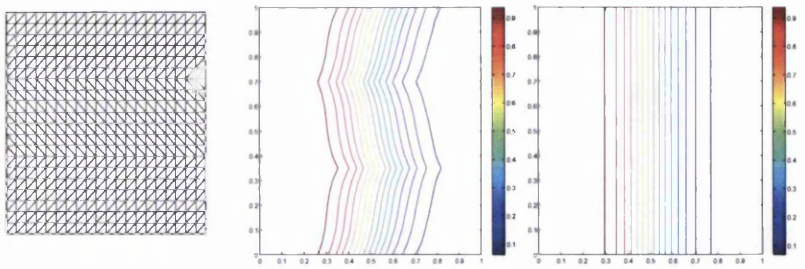

(a) (b) (c)

Figure 7.10: Case 1 - (a) ZigZag mesh; saturation profiles using (a) single-point upstream-weighting and (b) multidimensional approximations.

7.3.2 Case 2: Linear Full Tensor Quarter Five Spot

The second case involves a linear Buckley Leverett flux, corresponding with linear relative permeabilities and has the same set up as case 1 presented in chapter 6 section 6.4.1. Here water saturation contours are shown at 0.25 pore volumes injected (PVI) for the same CFL number equal to 0.4. The main feature of this case is the advection of the stable discontinuity across the grid. The standard single-point upstream results on distorted structured and unstructured triangular grids are shown in Figures 7.11(b), 7.12(b) and 7.13(b). The multidimensional upwind results are shown in Figures 7.11(c), 7.12(c) and 7.13(c). The standard scheme results show a largely diffused front. In contrast, the multidimensional scheme provides improved symmetry of the problem, while predicting earlier breakthrough with minimal cross-flow spreading.

7.3.3 Case 3: High Mobility Ratio Piston Flow

The third case involves a nonlinear Buckley Leverett flow subject to fluid injection on the left hand boundary and specified pressure on the right hand boundary and a full homogeneous permeability tensor with principal axes oriented at 45 degrees to the reservoir domain with 20 to 1 anisotropy ratio. The water and oil relative permeabilities are respectively $k_{rw} = S^2$ and $k_{ro} = (1 - S)^2$. The normalized tensors have components

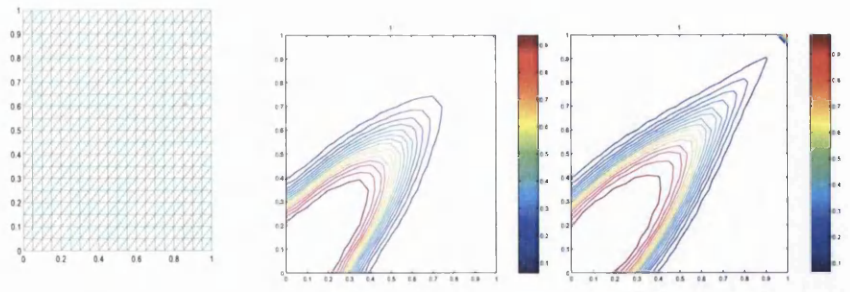

(a) (b) (c)

Figure 7.11: Case 2 - (a) Triangular mesh oriented in the direction of the flow (21x21); saturation profile using (b) single-point upstream-weighting and (c) multidimensional scheme.

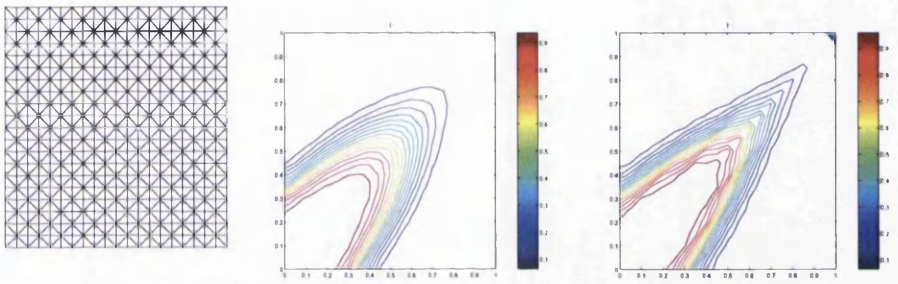

(a) (b) (c)

Figure 7.12: Case 1 - (a) Cross Mesh (21x21); saturation profile using (b) single-point upstream-weighting and (c) multidimensional scheme.

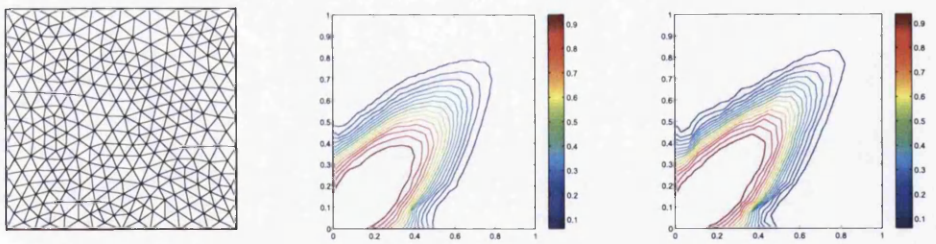

(a) (b) (c)

Figure 7.13: Case 2 - (a) Delaunay mesh (290 nodes); saturation profile using (b) single-point upstream-weighting and (c) multidimensional scheme.

$K_{xx} = 1.0$, $K_{yy} = 1.0$, $K_{xy} = 0.9$. The flow mobility ratio is set to $M = 40$. The results are computed on the triangular grid with an aspect ratio 4:1 shown in Figure 7.14(a). The result obtained using standard single-point upstream weighting is shown in Figure 7.14(b) and that obtained using the data based multidimensional wave-oriented higher dimensional upwind scheme is shown in Figure 7.14(c). The multidimensional flux result is shown in Figure 7.14(d). Figure 7.15 shows a reference solution on a 64x64 cartesian grid. The standard first order results indicate a strong grid orientation bias with a spread front that first collides with the top wall before breakthrough occurs at the right hand boundary. In contrast the results obtained with the multidimensional schemes show reduced grid dependence and provide improvement in front resolution, although the multidimensional flux result is slightly sharper than the multidimensional data result. The flow pattern is now consistent with the problem, where the full tensor forces the flow across the domain, with breakthrough at the right hand boundary now consistent with the reference solution.

7.3.4 Case 4: Nonlinear piston Full Tensor Flow

The last case has the same domain, boundary conditions and non-linear relative permeabilities as Case 3, now with a unity mobility ratio i.e. $M = 1$ and involves a full permeability tensor with a 10 to 1 anisotropy ratio. The normalized tensors have components $K_{xx} = 1.0$, $K_{yy} = 1.0$, $K_{xy} = 0.82$. Results are computed on a triangular grid. The reference solution is shown on a 64x64 regular grid in Figure 7.17. The results obtained using standard single-point upstream weighting are shown in Figure 7.16(b) and those obtained using the data based multidimensional wave-oriented upwind scheme are shown in Figure 7.16(c). The multidimensional flux results are shown in Figure 7.16(d).
The standard first order results indicate a more diffused front, whereas the results obtained with the multidimensional schemes show reduced grid dependence on the distorted unstructured meshes and provide improvement of front resolution with a clearer indication of the flow pattern, which is consistent with the problem, where the full tensor forces the flow across the domain.

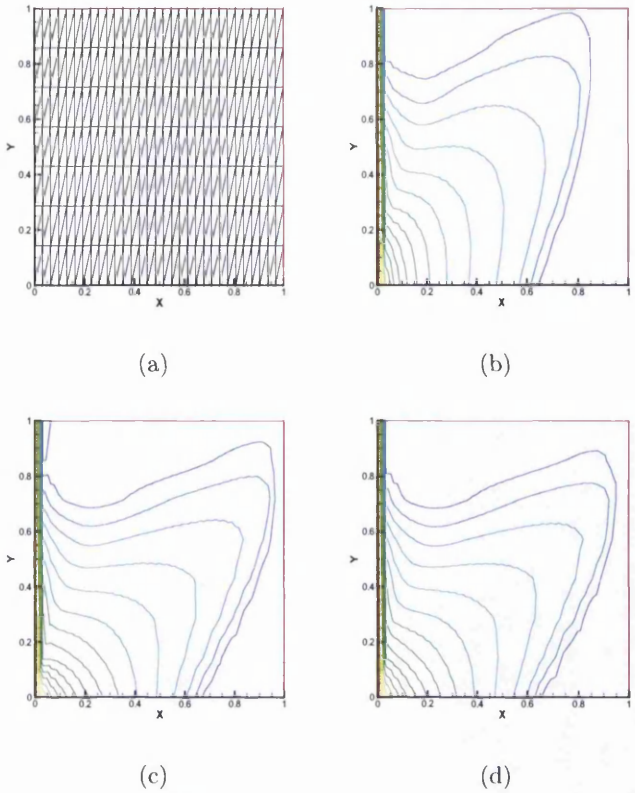

(a) (b)

(c) (d)

Figure 7.14: Case 3 - (a) Grid (40x10); saturation profile using (b) single-point upstream-weighting,(c) multidimensional data based scheme and (d) multidimensional flux based scheme.

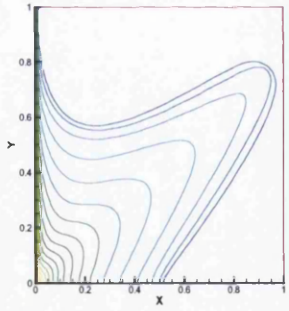

(a)

Figure 7.15: Case 3 - Reference solution on a 64x64 cartesian mesh

7.4 Conclusions

A family of multidimensional upwind schemes is presented for hyperbolic conservation laws on triangular grids. The methods are locally conservative and are coupled with

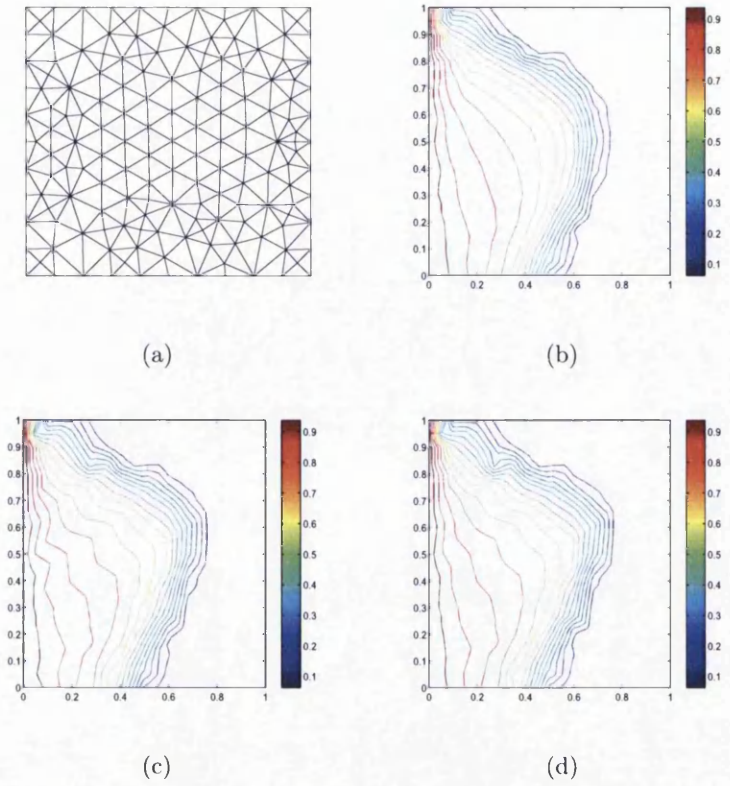

Figure 7.16: Case 4 - (a) Unstructured triangular grid (159 nodes); saturation profile using (b) single-point upstream-weighting, (c) multidimensional data based scheme and (d) multidimensional flux based scheme.

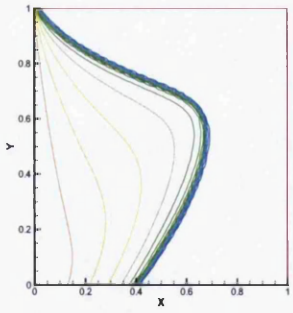

Figure 7.17: Case 4 - Reference solution on a 64x64 cartesian mesh

consistent and efficient continuous Darcy flux approximations and applied to two-phase flow problems. Positivity conditions are derived for linear convection including the CFL limits. The schemes permit higher CFL numbers than the standard upwind scheme.

Two-phase flow results are presented. Comparisons with the standard first order single point upstream weighting scheme are made on a both regular and distorted unstructured triangular grids for cases involving full-tensor coefficient velocity fields. The comparisons demonstrate the benefits of the higher dimensional schemes both in terms of improved front resolution and significantly reduced cross-wind diffusion.

Chapter 8

Gravity and Systems

This chapter describes the application of the numerical methods presented in chapters 5-7 to gravity driven flow problems as well as to multi-component multi-phase flow systems through the study of a three component two phase flow polymer flood system in two dimensional space.

The main objectives are first to provide an extension of the multidimensional schemes in order to handle general flow situations involving counter current gravity flows. The second aim is to develop a multidimensional formulation for systems of hyperbolic equations. Finally, we investigate different tracing formulations.

A two phase flow water and oil system is considered for the gravity case. A polymer flood systemis considered here which is comprised of a miscible aqueous phase (water and polymer) and an immiscible oleic phase.

The chapter is organised as follows. The first section 8.1 deals with gravity driven flows, where two upwind approximations are presented and two different multidimensional data based reconstructions are proposed. The different formulations are compared for a gravity segregation on quadrilateral and triangular unstructured meshes. Section 8.2 is devoted to the two dimensional three component two phase flow system, where the first order and higher order upwind formulations based on componentwise reconstructions following the ideas in [51, 21] are presented. Three different limiting strategies involving conservative, primitive and characteristic variables are adopted for the higher order method. Also, three innovative tracing approaches are also introduced in the same section that lead to a novel family of multidimensional data based first order schemes for hyperbolic systems for flow in porous media. Finally, numerical results are presented and comparisons of the different formulations illustrate the benefits of the new formulations with respect to the

standard methods.

8.1 Gravity Driven Flows

8.1.1 Formulation

Recall the continuity equations for a gravity driven two phase flow:

$$\int_{\Omega_{cv}} \frac{\partial S_p}{\partial t} d\Omega + \oint_{\partial\Omega_{cv}} \mathbf{V}_p \cdot \hat{\mathbf{n}} ds = m_p \tag{8.1.1}$$

where the integral is taken over Ω_{cv} and where S_p, $\mathbf{V}_p$ and m_p are the p^{th} phase saturation, Darcy velocity and specified phase flow rate respectively. Here we consider two upwind formulations: the first one corresponds with the upstream mobility weighting [13, 128]. This approach is the reservoir simulation standard and is physically motivated. The idea is to solve for both phase saturations independently using the phase velocities (modeled by Darcy's law) in order to decide upon the flow direction for each phase. This enables the scheme to account for the counter current flow when the phases migrate in opposite directions, which is typical of gravity segregation problems. The second approach uses a fractional flow formulation and involves expressing the flux in terms of a single phase saturation, water saturation being the usual choice and is favoured here. Two phase incompressible flow is governed by a single scalar hyperbolic equation coupled with an equation for the pressure equation in general case; the saturation for the oil is deducted from the volume balance equation, where the saturations sum to one. Upwinding is performed according to the characteristic wave speed defined from the hyperbolic equation. This scheme is well established [73] and provides physically consistent solutions.
The phase continuity equations (8.1.1) are coupled through the discrete pressure equation (4.2.8). Control volume distributed Darcy flux approximations presented in [52] (see section 4.2.1) are used for the elliptic component. Note here that, in order to account for gravity, Equation (4.2.9) is adjusted and takes the form:

$$\mathrm{F}_{T_i} = -\int_{\partial\Omega_{cv}} \Lambda \sum_{j=1}^{2} T_{ij}(\phi_{\xi_j} + \overline{\rho} g h_{\xi_j}) \mathrm{d}\Gamma_i, \tag{8.1.2}$$

where ξ_i are local curvilinear parametric coordinates, Γ_i is the parametric coordinate surface increment and ϕ_{ξ_j} (respectively h_{ξ_j}) is the derivative of ϕ (respectively h) with respect to ξ_j and $\mathbf{T} = J\mathbf{J}^{-1}\mathbf{K}\mathbf{J}^{-T}$ is the general tensor defined via the Piola transformation which

is a function of the Cartesian permeability tensor and geometry, where $J_{ij} = \partial x_i / \partial \xi_j$ is the Jacobian of the local curvilinear coordinate transformation, and $J = x_\xi y_\eta - y_\xi x_\eta$ is the Jacobian determinant and $\bar{\rho}$ is defined by Equation (2.2.7).
An IMPES algorithm, section 4.2.5, is adopted here using the consistent locally conservative control volume distributed Darcy flux approximation. Explicit first order forward Euler method is used for the temporal discretisation. In this chapter, we consider a finite volume edge based cell vertex approximation with focus on the spatial discretisation.

Scheme A: Velocity Upwind

In the absence of capillary forces, the Darcy velocities of the aqueous and oleic phases including gravity are written as:

$$\begin{aligned} \mathbf{V}_w &= -\lambda_w \mathbf{K}(\nabla\phi + \rho_w g \nabla h), \\ \mathbf{V}_o &= -\lambda_o \mathbf{K}(\nabla\phi + \rho_o g \nabla h). \end{aligned} \tag{8.1.3}$$

We recall the upstream mobility weighting finite volume approximation written as:

$$(S_{p_i}^{n+1} - S_{p_i}^n)\tau_i + \Delta t \sum_{j=1}^{N_{edV}} \lambda_p(\mathbf{S}_L^n, \mathbf{S}_R^n) w_{p_e(i,j)}(\phi^{n+1}) = \Delta t M_{p_i}, \tag{8.1.4}$$

as before where the approximate upwind mobility is defined according to the sign of the local wave velocities w_{p_e} with respect to the local frame of reference aligned with the direction i to j along the edge $e(i,j)$, as defined in section 4.2.2. Here, $\mathbf{S}_L^n, \mathbf{S}_R^n$ are the left and right hand values of the phase saturation vectors with respect to edge $e(i,j)$ and n denotes the time level of the scheme. The upwind scheme is then written as:

$$\lambda_p(\mathbf{S}_L^n, \mathbf{S}_R^n) = \begin{cases} \lambda_p(\mathbf{S}_L^n) & w_{p_e} \geq 0 \\ \lambda_p(\mathbf{S}_R^n) & w_{p_e} < 0 \end{cases} \tag{8.1.5}$$

The local p^{th} phase wave velocity corresponds with the net edge based single phase Darcy flux (for the phase p) at the edge $e(i,j)$, referred to herein as w_{p_e} and consists of the sum of the sub-face discrete fluxes expressed on each cell sharing the edge e as:

$$F_{p_i}(\phi) = -\int_{\partial\Omega_{cv}} \lambda_p \sum_{j=1}^{2} T_{ij}(\phi_{\xi_j} + \bar{\rho} g h_{\xi_j}) \mathrm{d}\Gamma_i. \tag{8.1.6}$$

The first order upwind scheme is defined with $\mathbf{S}_L^n = \mathbf{S}_i^n$ and $\mathbf{S}_R^n = \mathbf{S}_j^n$. Note here that we solve for both the water and oil saturations.

Scheme B: Characteristic Upwind

Using the fractional approach the integral continuity equations (8.1.1) reduce to a hyperbolic equation for the water saturation S, written as:

$$\int_{\Omega_{cv}} \frac{\partial S}{\partial t} + \oint_{\partial\Omega_{cv}} \mathbf{V} \cdot \hat{\mathbf{n}} \mathrm{d}s = 0 \tag{8.1.7}$$

in the absence of source terms where $\mathbf{V}$ is the water velocity and takes the form:

$$\mathbf{V}(S) = f(S)\mathbf{V}_T + \gamma(S)\mathbf{V}_G. \tag{8.1.8}$$

Here,

$$\mathbf{V}_T = \mathbf{V}_w + \mathbf{V}_o$$

is the total velocity and

$$\mathbf{V}_G = g(\rho_o - \rho_w)\mathbf{K}\nabla h.$$

The fractional flow is defined by:

$$f(S) = \frac{\lambda_w(S)}{\Lambda(S)} = \frac{MS^\zeta}{MS^\zeta + (1-S)^\zeta} \tag{8.1.9}$$

and the function γ corresponds to:

$$\gamma(S) = \lambda_o f(S) = \frac{\lambda_o(S)\lambda_w(S)}{\Lambda(S)} = \frac{M(1-S)^\zeta S^\zeta}{MS^\zeta + (1-S)^\zeta} \tag{8.1.10}$$

where ζ defines to the order of mobility. The edge-based vertex centered finite volume discretization of Equation (8.1.7) on unstructured grids takes the form:

$$(S_i^{n+1} - S_i^n)\tau_i + \Delta t \sum_{j=1}^{N_{edV}} [\mathrm{f}(\mathbf{S}_L^n, \mathbf{S}_R^n) F_{T_{e(i,j)}}(\phi^{n+1}) + \gamma(S_L^n, S_R^n) F_{G_{e(i,j)}}] = 0, \tag{8.1.11}$$

where $F_{T_{e(i,j)}}$ is the net edge based flux defined by Equation (8.1.2) and accounts for the total velocity contribution. The net component of flux due to gravity $\mathrm{F}_{G_{e(i,j)}}$ includes the gravity potential discretisation written as

$$\mathrm{F}_G = -\int_{\partial\Omega_{cv}} (\rho_w - \rho_o) g \sum_{j=1}^{2} T_{ij} h_{\xi_j} \mathrm{d}\Gamma_i. \tag{8.1.12}$$

The net Darcy flux is then defined by $\mathfrak{V}_e$ where

$$\mathfrak{V}_e(S) = \mathrm{f}(S) F_{T_{e(i,j)}}(\phi^{n+1}) + \gamma(S) F_{G_{e(i,j)}}, \tag{8.1.13}$$

and the characteristic wave velocity is written as

$$w_{c_e}(S) = \frac{\partial \mathrm{f}}{\partial S} F_{T_{e(i,j)}}(\phi^{n+1}) + \frac{\partial \gamma}{\partial S} F_{G_{e(i,j)}}. \tag{8.1.14}$$

The characteristic upwind flux approximation used here is defined by:

$$\mathfrak{V}_e(S_L^n, S_R^n) = \begin{cases} \mathfrak{V}_e(S_L^n) & \text{if } w_{c_e}(S) \geq 0, \text{ for } S \in [S_L, S_R], \\ \mathfrak{V}_e(S_R^n) & \text{if } w_{c_e}(S) \leq 0, \text{ for } S \in [S_L, S_R], \\ \mathfrak{V}_e^{LLF} & \text{otherwise} \end{cases} \tag{8.1.15}$$

where at sonic points, a Local Lax Friedrichs (LLF) flux approximation $\mathfrak{V}_e^{LLF}$ is used as an entropy fix in order to disperse expansion shocks, [148, 73]. Again, here the sonic loci are determined using a test for the change of sign in w_{c_e} evaluated at the left and right states of the local Riemann problem. Practically, the LLF approximation is adopted when $w_{c_e}(S_L) < 0$ and $w_{c_e}(S_R) > 0$ as inspired from [73]. The Local Lax Friedrichs numerical flux is written as:

$$\mathfrak{V}_e^{LLF} = \frac{1}{2}[(\mathfrak{V}(S_L^n) + \mathfrak{V}(S_R^n)) - \max_{[S_L, SR]} \mid w_{c_e} \mid (S_R^n - S_L^n)]. \tag{8.1.16}$$

8.1.2 Multidimensional Schemes and Tracing Velocities

In the case of two phase immiscible flow, the tracing velocities are well defined and correspond to the total Darcy flux F_{Te} on the grid edges as detailed in chapters 5-7. The tracing parameters are independent of saturation data.

In this section, the family of genuinely multidimensional edge-based finite volume schemes on unstructured grids using a data formulation is adopted. The details of approximation are discussed in section 7.2. In the following, we adopt the same notations as in chapter 7, section 7.2. The multidimensional data reconstructions with respect to the key edge $e(i,j)$ (Figure7.7(b)) are defined by:

$$\begin{aligned} \mathbf{S}_{L_e}^n &= (1-\xi_e)\mathbf{S}_i^n + \xi_e[\chi_e \mathbf{S}_1^n + (1-\chi_e)\mathbf{S}_2^n] \\ \mathbf{S}_{R_e}^n &= (1-\eta_e)\mathbf{S}_j^n + \eta_e[\chi_e \mathbf{S}_4^n + (1-\chi_e)\mathbf{S}_3^n] \end{aligned} \tag{8.1.17}$$

where

$$\chi_e = \begin{cases} 1 \text{ if the wave velocity is pointing from subcell I to subcell IV,} \\ 0 \text{ if the wave velocity is pointing from subcell II to subcell III.} \end{cases} \tag{8.1.18}$$

and $0 \leq \xi \leq 1$ and $0 \leq \eta \leq 1$ denote the weighting factors where ξ (respectively η) is used to interpolate the left (respectively right) state as a convex linear combination of

$\mathbf{S}_i$ (respectively $\mathbf{S}_j$) and $\mathbf{S}_1$ (respectively $\mathbf{S}_3$) or $\mathbf{S}_2$ (respectively $\mathbf{S}_4$) depending on the direction of the wave speed. Note that here node 1 and 3 coincide (respectively 2 and 4) when $cell_1$ (respectively $cell_2$) degenerates to a triangle.

The focus here is on the definition of the tracing parameters ξ and η for gravity driven two phase flow. Instead of using the total Darcy fluxes for the tracing, we propose to use two different tracing velocities. The first formulation corresponds with tracing according to the physical velocities defined in Equation (8.1.3). The second formulation uses the characteristic water phase velocity defined below. Another alternative could also be to use the total Darcy flux for upwinding. Nevertheless, in the case of high gravity numbers where the total Darcy flux term F_T is negligible, the flow is mainly driven by the gravity term F_G. Due to this limitation, this method will not be considered in this work.

Formulation I: Tracing with Phase Velocities

Formulation I follows section 7.2 where the resultant total Darcy flux F_{T_e} used for the tracing is now replaced by the resultant phase Darcy flux at the centre of the edge w_{p_e} defined by Equation (8.1.6) for the tracing step. Also, note that w_{p_e} reduces indeed to F_{T_e} in the absence of gravity. Hence, the flux ratios R_{1e} and R_{2e} are expressed as:

$$R_{1e} = \frac{w_{p_c}}{w_{p_e}}, R_{2e} = \frac{w_{p_d}}{w_{p_e}}; \tag{8.1.19}$$

and $R = \max(R_{1e}, R_{2e}, 0)$. Then, the weighting factor takes the form:

$$\xi_e \leq \beta \min(1, R) \text{ with } \beta = \begin{cases} \frac{1}{3} & \text{if } w_{p_a} < 0 \text{ and } w_{p_b} < 0, \\ \frac{1}{2} & \text{otherwise} \end{cases} \tag{8.1.20}$$

Formulation II: Tracing with Characteristic Velocity

First, define the characteristic flux at the edge $e(i, j)$ for the aqueous phase as:

$$W_{c_e} = \begin{cases} \frac{\mathfrak{V}_e(S_R) - \mathfrak{V}_e(S_L)}{S_R - S_L}, & \mid S_R - S_L \mid \geq \epsilon; \\ w_{c_e}(S), & \mid S_R - S_L \mid \leq \epsilon. \end{cases} \tag{8.1.21}$$

where the characteristic wave speed w_{c_e} is defined in Equation (8.1.14) and the Darcy flux $\mathfrak{V}_e$ is defined by Equation (8.1.13).

Note here that formulation II involves the resultant characteristic wave velocity for the water phase at the centre of the edge W_{c_e} defined by Equation (8.1.21) in the tracing step

instead of using the resultant total Darcy flux F_{T_e}.
Then, the flux ratios R_{1e} and R_{2e} become:

$$R_{1e} = \frac{W_{c_c}}{W_{c_e}}, R_{2e} = \frac{W_{c_d}}{W_{c_e}}, \tag{8.1.22}$$

and the weighting factor is written as:

$$\xi_e \leq \beta \min(1, R) \text{ with } \beta = \begin{cases} \frac{1}{3} & \text{if } W_{c_a} < 0 \text{ and } W_{c_b} < 0, \\ \frac{1}{2} & \text{otherwise} \end{cases} \tag{8.1.23}$$

with $R = \max(R_{1e}, R_{2e}, 0)$.

8.1.3 Case Study of Gravity Segregation: Oil Shale Barrier

Gravity driven two-phase flow is used to investigate the different multidimensional formulations in two dimensions. Quadratic relative permeabilities are assumed with $\zeta = 2$. The mobility ratio is set to unity. The permeability tensor is assumed to be diagonal isotropic.
The initial condition consists of an oil lens sitting on top of a shale barrier, in an otherwise gas filled reservoir, with solid walls at the sides and top boundaries.
Pressure is specified on the lower boundary. The boundaries and initial interface are shown in Figure 8.1. All oil saturations are shown at the same output time 0.25 PVI

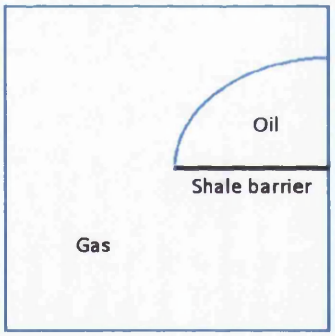

Figure 8.1: Characteristics

where the shock due to the downward moving heavier water phase has formed followed by the Buckley Leverett expansion. A CFL of 0.45 is used for low order. The time step is reduced by a factor 2 for higher order results.

	Upstream Upwinding Scheme A	Characteristic upwinding Scheme B
Standard first order	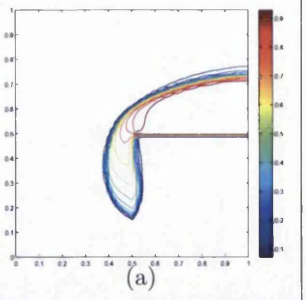 (a)	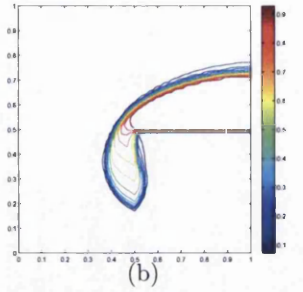 (b)
Standard higher order	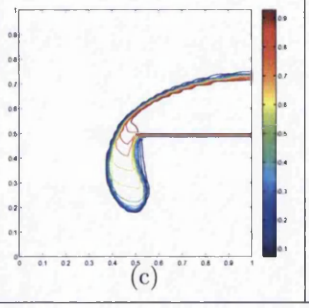 (c)	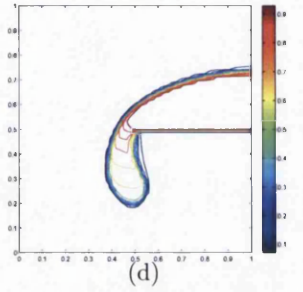 (d)

Figure 8.2: Reference Standard First order and higher order Solutions on a 65x65 Cartesian mesh.

Scheme	Upwind
A	Velocity
B	Characteristic

Table 8.1: Notation - Upwind schemes.

Reference Solutions

Reference solutions on a uniform 65x65 Cartesian grid using standard first order and standard higher order (detailed in chapter 6) are shown in Figure 8.2 for both upwind formulations A and B. Results are computed on unstructured triangular and quadrilateral grids shown in Figure 8.3.

The first-order schemes smears the discontinuity (Figure 8.2(a) and (b)). Higher order results (figures 8.2(c) and (d)) for both schemes A and B show a noticeable improvement of the saturation front resolution compared with the low order method (figures 8.2 (a) and (b)).

The results using scheme B show better solution quality overall than those computed

Combination	Correspondance
A-I	Velocity upwind Phase velocity tracing
A-II	Velocity upwind Characteristic tracing
B -I	Characteristic upwind Phase velocity tracing
B -II	Characteristic upwind Characteristic tracing

Table 8.2: Notation - Multidimensional formulations.

using the upstream mobility upwind scheme A in terms of saturation front detection.

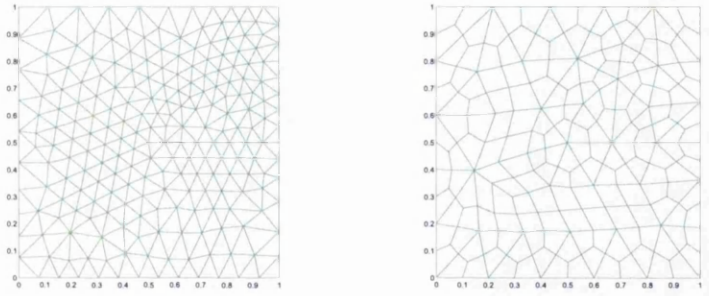

(a) (b)

Figure 8.3: Meshes.

Multidimensional Solutions

Standard first order results on the unstructured grids show a smeared front for both upwind formulations with scheme B providing better resolution of the rarefaction and a more accurate position of water front than the scheme A.

The multidimensional velocity upwind characteristic trace formulation (A-II) shows a sign of instability and provides oscillatory results on both triangular and quadrilateral grids as indicated in Figures 8.4(e) and 8.5(e).

Also, the characteristic upwind using velocity tracing formulation (B-I) yields overshoots in the saturation profile on the quadrilateral grid (Figure 8.5(d)). This is most likely due to the characteristic velocity and phase fluxes having opposite signs, which results in an inconsistency between the upwind strategy and tracing fluxes used in the multidimensional tracing step.

Note here that the multidimensional characteristic upwind velocity trace (B-I) result on the triangular mesh in Figure 8.4(d) is essentially oscillation free. This observation infers

that the structure of the triangular mesh has contributed in restricting the weighting coefficients in regions where the same scheme failed on the quadrilateral mesh adding a stabilizing effect to the formulation.

Multidimensional results using consistent tracing options (A-I) (Figures 8.4(c)) and 8.5(c)) and (B-II) (Figures 8.4(f) and 8.5(f)) provide oscillation free results with noticeably sharper resolution of the saturation front, particularly in regions where a cross flow is important, when compared with standard first order.

	Velocity Upwinding Scheme A	Characteristic upwinding Scheme B
Standard first order	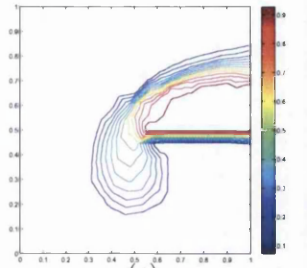 (a)	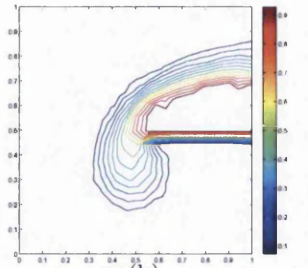 (b)
Tracing on the Wave Velocity Formulation I	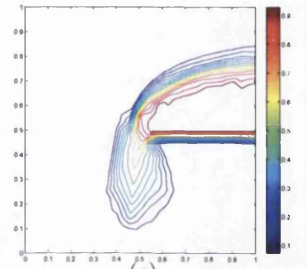 (c)	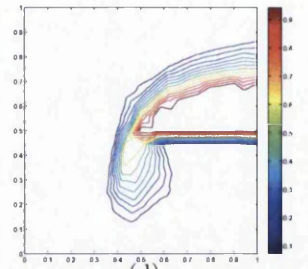 (d)
Tracing on the Characteristic velocity Formulation II	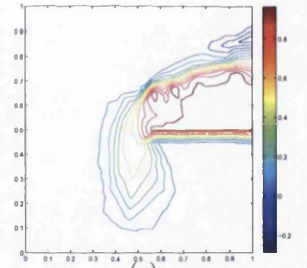 (e)	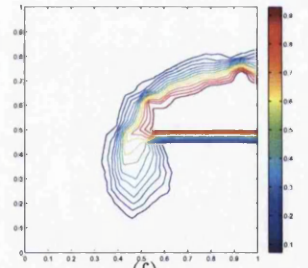 (f)
Standard Higher order	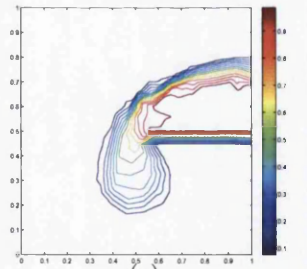 (g)	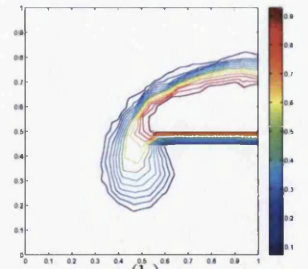 (h)

Figure 8.4: Case1: Saturation profiles on the triangular mesh.

	Velocity Upwinding Scheme A	Characteristic upwinding Scheme B
Standard First Order	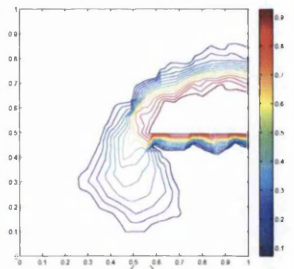 (a)	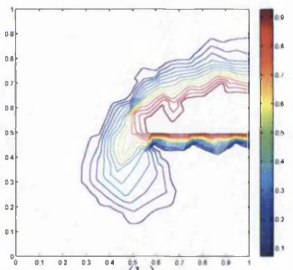 (b)
Tracing with phase velocity Formulation I	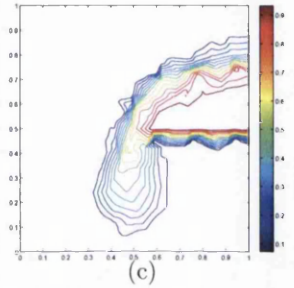 (c)	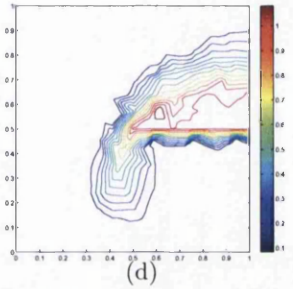 (d)
Tracing with characteristic velocity Formulation II	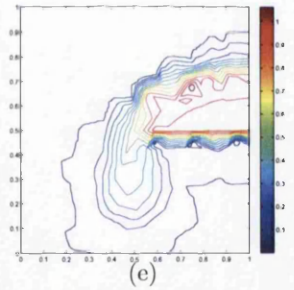 (e)	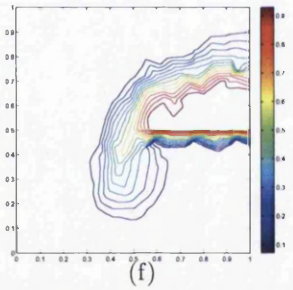 (f)
Standard higher Order	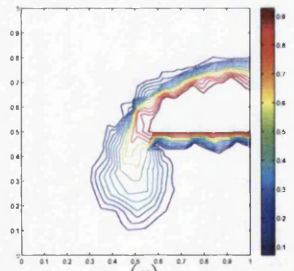 (g)	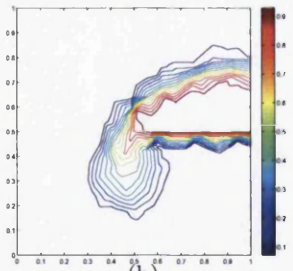 (h)

Figure 8.5: Case1: Saturation profiles on the unstructured quadrilateral grid.

8.2 Polymer flood three component two phase flow systems

8.2.1 Flow Equations

The integral conservation equations for a polymer flood three component two phase flow system over Ω in the absence of source and sink terms are written as:

$$\int_{\Omega} \frac{\partial \mathbf{S}}{\partial t} + \oint_{\partial \Omega_{cv}} \mathbf{F}(\mathbf{S}) \cdot \hat{\mathbf{n}} ds = \mathbf{0}, \tag{8.2.1}$$

where $\mathbf{F} = (\mathbf{V}, C\mathbf{V})^T$ and $\mathbf{S}$ is the vector of conservative variables defined by Equation (2.3.12) (see section 2.3.2). In this section, S denotes the miscible phase saturation and C the component concentration in the miscible phase, here the aqueous phase, $\mathbf{V}$ refers to the Darcy velocity of the aqueous phase defined by:

$$\mathbf{V}(\mathbf{S}) = f(\mathbf{S})\mathbf{V}_T + \gamma(\mathbf{S})\mathbf{V}_G. \tag{8.2.2}$$

The fractional flow takes the same form as in Equation (8.1.9) where the water viscosity is now a function of concentration and is set to $\mu_w = 0.5 + C$. For convenience, the gravity term is omitted in the following and the Darcy velocity reduces to

$$\mathbf{V}(\mathbf{S}) = f(\mathbf{S})\mathbf{V}_T. \tag{8.2.3}$$

8.2.2 Characteristic Upwind approximation

We use a characteristic decomposition upwind scheme. The edge based vertex centered finite volume discretisation of Equation (8.2.1) with respect to control volume j takes the form

$$\tau_j \frac{\mathbf{S}_j^{n+1} - \mathbf{S}_j^n}{\Delta t} + \sum_{e=1}^{N_{edV}} \mathrm{f}(\mathbf{S}_{L_e}^n, \mathbf{S}_{R_e}^n) F_{T_e} = 0, \tag{8.2.4}$$

where F_{T_e} is the discrete total Darcy flux evaluated at the centre of the edge e. The system is first decomposed into characteristic form. Decomposition is performed via the local transformation with respect to the edge e

$$\Delta \mathbf{S} = \mathbf{R}_e \Delta W, \tag{8.2.5}$$

where $\mathbf{R}_e$ is the matrix of right eigenvalues of the system Jacobian matrix $A = \frac{\partial \mathbf{F}}{\partial \mathbf{S}}$ and the matrix of eigenvalues Γ_e is defined via

$$\Gamma_e = \mathbf{R}_e^{-1} \mathbf{A}_e \mathbf{R}_e \tag{8.2.6}$$

and $\Delta\mathbf{S}$, $\Delta\mathbf{W}$ represent the respective conservative and characteristic variable increments. The matrix of discrete eignevalues Γ_e is written as

$$\mathbf{\Gamma_e} = \begin{bmatrix} \frac{\partial f}{\partial S} & 0 \\ \\ 0 & \frac{f}{S} \end{bmatrix}. \tag{8.2.7}$$

and the transformation matrix $\mathbf{R_e}$ is defined by:

$$\mathbf{R_e} = \begin{bmatrix} 1 & \frac{\partial f}{\partial C} \\ \\ C & C\frac{\partial f}{\partial C} + S(\frac{f}{S} - \frac{\partial f}{\partial S}) \end{bmatrix}. \tag{8.2.8}$$

The upwind scheme is in effect applied to each characteristic wave component and the discrete system is recomposed into a conservative form. The numerical flux corresponding to the edge e is defined by:

$$f(\mathbf{S_{L_e}}, \mathbf{S_{R_e}}) = \frac{1}{2}[(\mathbf{f}(\mathbf{S_{L_e}})) + \mathbf{f}(\mathbf{S_{R_e}}) - \mathbf{R} \mid \mathbf{\Gamma}_e \mid \mathbf{R}^{-1}(\mathbf{S_{R_e}} - \mathbf{S_{L_e}})], \tag{8.2.9}$$

Remark 8.2.1 *In the presence of stagnation points or if equal eigenvalues are detected (in which case, $\mathbf{R_e}$ becomes singular), a Rusanov flux approximation is locally applied [55]. The approximate flux thus takes the form:*

$$f(\mathbf{S}_{L_e}, \mathbf{S}_{R_e}) = \frac{1}{2}[(f(\mathbf{S}_{L_e})) + f(\mathbf{S}_{R_e}) - \mid \mathbf{\Gamma}_e^{RU} \mid (\mathbf{S}_{R_e} - \mathbf{S}_{L_e})], \tag{8.2.10}$$

where

$$\mid \Gamma^{RU} \mid = \max_{[S_L, S_R]} \max_{k} \mid \Gamma_e^k(\boldsymbol{S}) \mid \boldsymbol{I} \tag{8.2.11}$$

The matrix $\mathbf{R}$ is singular when the eigenvalues are equal. Also at sonic points, a Rusanov local Lax Friedrichs flux is applied locally i.e.

$$f(\mathbf{S}_{L_e}, \mathbf{S}_{R_e}) = \frac{1}{2}[(f(\boldsymbol{S}_L) + f(\boldsymbol{S}_R)) - \mid \Gamma_{RU} \mid (\boldsymbol{S}_R - \boldsymbol{S}_L)] \tag{8.2.12}$$

First order reconstructions correspond with $S_L = S_i$ and $S_R = S_j$. The CFL condition applies with respect to the maximum eigenvalue of the system.

8.2.3 Higher Order Approximations

Higher order approximation is introduced wave by wave and applied to the characteristic variables W, followed by recomposition to the conservative variables [55, 51].

Here, higher order expansions are introduced componentwise for the left and right states respectively where the higher order reconstruction are applied to the characteristic $\mathbf{W}$, conservative $\mathbf{S}$ or the primitive variables $\mathbf{C}$ repectively. We refer to chapter 5, section 5.2 for details of the higher order formulation on unstructured meshes, the same notation is adopted in this subsection.

Conservative Variables

The componentwise higher order left and right states are defined with respect to the *key* edge e (joining vertices i and j) are expressed as:

$$\begin{aligned} \mathbf{S_L} &= \mathbf{S}_i + \frac{1}{2}\Phi(\mathbf{r}_{ji}^{+})\Delta\mathbf{S}_{ji}, \\ \mathbf{S_R} &= \mathbf{S}_j - \frac{1}{2}\Phi(\mathbf{r}_{ji}^{-})\Delta\mathbf{S}_{ji}. \end{aligned} \tag{8.2.13}$$

where $\Phi(r^{\pm})$ are the slope limiters which are functions of adjacent discrete gradients

$$\begin{aligned} \mathbf{r}_{ji}^{+} &= (\Delta\mathbf{S}_{iu}/\Delta\mathbf{S}_{ji}), \\ \mathbf{r}_{ji}^{-} &= (\Delta\mathbf{S}_{dj}/\Delta\mathbf{S}_{ji}). \end{aligned} \tag{8.2.14}$$

Primitive Variables

Writing the scheme using the primitive variables gives [55]

$$\begin{aligned} \mathbf{S_L} &= \mathbf{S}_i + \frac{1}{2}\mathbf{P}_e\Phi(\mathbf{r}_{ji}^{+})\Delta\mathbf{S}_{ji}, \\ \mathbf{S_R} &= \mathbf{S}_j - \frac{1}{2}\mathbf{P}_e\Phi(\mathbf{r}_{ji}^{-})\Delta\mathbf{S}_{ji}. \end{aligned} \tag{8.2.15}$$

where $\mathbf{P}_e$ denotes the transformation matrix between conservative and primitive variables and the slope limiter Φ is fucntion of

$$\begin{aligned} \mathbf{r}_{ji}^{+} &= (\Delta\mathbf{C}_{iu}/\Delta\mathbf{C}_{ji}), \\ \mathbf{r}_{ji}^{-} &= (\Delta\mathbf{C}_{dj}/\Delta\mathbf{C}_{ji}). \end{aligned} \tag{8.2.16}$$

Characteristic Variables

Writing the scheme using the characteristic variables gives

$$\begin{aligned} \mathbf{S_L} &= \mathbf{S}_i + \frac{1}{2}\mathbf{R}_e\Phi(\mathbf{r}_{ji}^{+})\mathbf{R}_e^{-1}\Delta\mathbf{S}_{ji}, \\ \mathbf{S_R} &= \mathbf{S}_j - \frac{1}{2}\mathbf{R}_e\Phi(\mathbf{r}_{ji}^{-})\mathbf{R}_e^{-1}\Delta\mathbf{S}_{ji}. \end{aligned} \tag{8.2.17}$$

where $\mathbf{R}_e$ denotes the transformation matrix between characteristic and conservative defined in Equation (8.2.5) and the slope limiter Φ is fucntion of

$$\begin{aligned} \mathbf{r}_{ji}^{+} &= (\Delta\mathbf{W}_{iu}/\Delta\mathbf{W}_{ji}), \\ \mathbf{r}_{ji}^{-} &= (\Delta\mathbf{W}_{dj}/\Delta\mathbf{W}_{ji}). \end{aligned} \tag{8.2.18}$$

8.2.4 Multidimensional First Order Approximation

In this section, a family of genuinely multidimensional edge-based finite volume schemes on unstructured grids using a data formulation (chapter 7, section 7.2) is applied to the system.

Componentwise multidimensional data reconstructions with respect to the key edge $e(i,j)$ (Fig.7.7(b)) are proposed where three different tracing strategies are considered.

Scheme C: Conservative Tracing

The componentwise multidimensional right an left states reconstruction is written as:

$$\begin{aligned} \mathbf{S}_{L_e}^n &= (1-\xi_e)\mathbf{S}_i^n + \xi_e[\chi_e\mathbf{S}_1^n + (1-\chi_e)\mathbf{S}_2^n], \\ \mathbf{S}_{R_e}^n &= (1-\eta_e)\mathbf{S}_j^n + \eta_e[\chi_e\mathbf{S}_4^n + (1-\chi_e)\mathbf{S}_3^n], \end{aligned} \tag{8.2.19}$$

where in this formulation, the same scalar weighting factor ξ_e (η_e) is used and where both saturation and concentraion components are traced using the characteristic Rankine-Hugoniot wave speed W_{c_e} defined by Equation (8.1.21).

Scheme D: Characteristic Tracing

In the second formulation, the multidimensional approximation is introduced wave by wave and applied to the characteristic variables followed by recomposition to the conservative variables. The left and right multidimensional characteristic reconstruction with respect to the edge e are defined by:

$$\begin{aligned} \mathbf{S}_{L_e} &= \mathbf{S}_i + \mathbf{R}_c\xi_e\chi_e\mathbf{R}_c^{-1}\mathbf{\Delta S}_{i1} + \mathbf{R}_d\xi_e(\mathbf{I}-\chi_e)\mathbf{R}_d^{-1}\mathbf{\Delta S}_{i2}, \\ \mathbf{S}_{R_e} &= \mathbf{S}_j + \mathbf{R}_a\eta_e\chi_e\mathbf{R}_a^{-1}\mathbf{\Delta S}_{j3} + \mathbf{R}_b\eta_e(\mathbf{I}-\chi_e)\mathbf{R}_b^{-1}\mathbf{\Delta S}_{j4}, \end{aligned} \tag{8.2.20}$$

where the weighting factors are defined in a tensorial form, e.g.

$$\xi_{\mathbf{e}} = \begin{bmatrix} \xi_1 & 0 \\ 0 & \xi_2 \end{bmatrix}. \tag{8.2.21}$$

The definition of the weights ξ_1 and ξ_2 follows Equation (7.2.4) and is based on the first and second characteristic wave velocities, W_{c_e} defined in Equation (8.1.21) and $\frac{f}{S}\mathbf{V_e(S)}$ respectively.

Scheme E: Primitive Tracing

The third tracing option involves tracing on the characteristic Rankine-Hugoniot wave speed W_{c_e} for the saturation variable and tracing on $\frac{f}{S}\mathbf{V_e(S)}$ multidimensional reconstruction of the concentration variable. The left and right edge-based multidimensional saturation and concentration reconstructions with respect to the key edge e, are written as:

$$\begin{aligned} \mathbf{S}_{L_e} &= \mathbf{S}_i + \mathbf{P}_c\xi_e\chi_e\mathbf{\Delta C}_{i1} + \mathbf{P}_d\xi_e(\mathbf{I}-\chi_e)\mathbf{\Delta C}_{i2}, \\ \mathbf{S}_{R_e} &= \mathbf{S}_j + \mathbf{P}_a\eta_e\chi_e\mathbf{\Delta C}_{j3} + \mathbf{P}_b\eta_e(\mathbf{I}-\chi_e)\mathbf{\Delta C}_{j4}, \end{aligned} \tag{8.2.22}$$

where the tensors of weighing factors correspond to those used for the multidimensional characteristic reconstructions Equation (8.2.4).

8.2.5 Case Study of a Non Linear High Mobility Full Tensor Polymer Flood

The three component two-phase flow test cases consists of a polymer flood into an oil filled reservoir, where the injected aqueous phase is comprised of polymer miscible with water. Quadratic relative permeabilities are assumed with $\zeta = 2$ and the normalised aqueous viscosity is a function of polymer concentration with $\mu = 0.5 + C$. Injection of polymer miscible with water causes a contact discontinuity to form in aqueous saturation, which terminates the rarefaction before the shock. The reference solution on a 256x256 Cartesian grid is shown in Figure 8.8.

The numerical case involves a full homogeneous permeability tensor with principal axes oriented at 45 degrees to the reservoir domain with 40 to 1 anisotropy ratio. Water and polymer are injected on the left hand boundary and specified pressure on the right hand boundary. The mobility ratio is set to be equal to 10.

The computed saturation are shown in figures 8.6-8.7 at the same output time using a 64x64 regular grid, with the prescribed initial data

$$\begin{cases} S, C = 0.05, 0.1, & x \leq 0.0; \\ S, C = 1.0, 0.7, & \text{otherwise.} \end{cases} \tag{8.2.23}$$

Higher Order solutions As in the one dimensional case, first order results (Figure 8.6(a),(b)) show smeared front resolution whereas the higher order method dramatically improves the resolution of the saturation profile.
The higher order upwind formulation with limiting applied to the conservative variables (Figures 8.6(c), 8.6(d)) fails to preserve the positivity of the solutions. Spurious oscillations are clearly visible in the concentration profile (Figure 8.6(d)). In contrast, the higher order results using both the primitive (Figures 8.6(e), 8.6(f)) and characteristic (Figures 8.6(g), 8.6(h)) variables are oscillation free. Note that the characteristic based higher order results provide the best results with sharp shock front and superior resolution of the rarefaction in the saturation profile when compared with the primitive and conservative formulations which both introduce extra diffusion in the solution particularly for the rarefaction.

Multidimensional Solutions All multidimensional results (Figure 8.7) are essentially oscillation free and show a clear improvement of the front resolution in comparison with the first order results where the saturation and concentration fronts are captured more accurately across the grid with significantly reduced cross-wind diffusion.
The characteristic based multidimensional results are shown in (Figure 8.7 (e), 8.7(f)) and provide the best results with improved resolution in the saturation front and clearly sharper concentration profile.

8.3 Conclusions

Multidimensional first order edge based upwind schemes have been applied to Gravity driven flow where different tracing velocity formulations are tested. Two phase flow numerical results are presented. Comparisons with single point upstream weighing scheme are made on triangular and quadrilateral unstructured grids. The multidimensional schemes provide better resolution of the saturation front than the standard first order

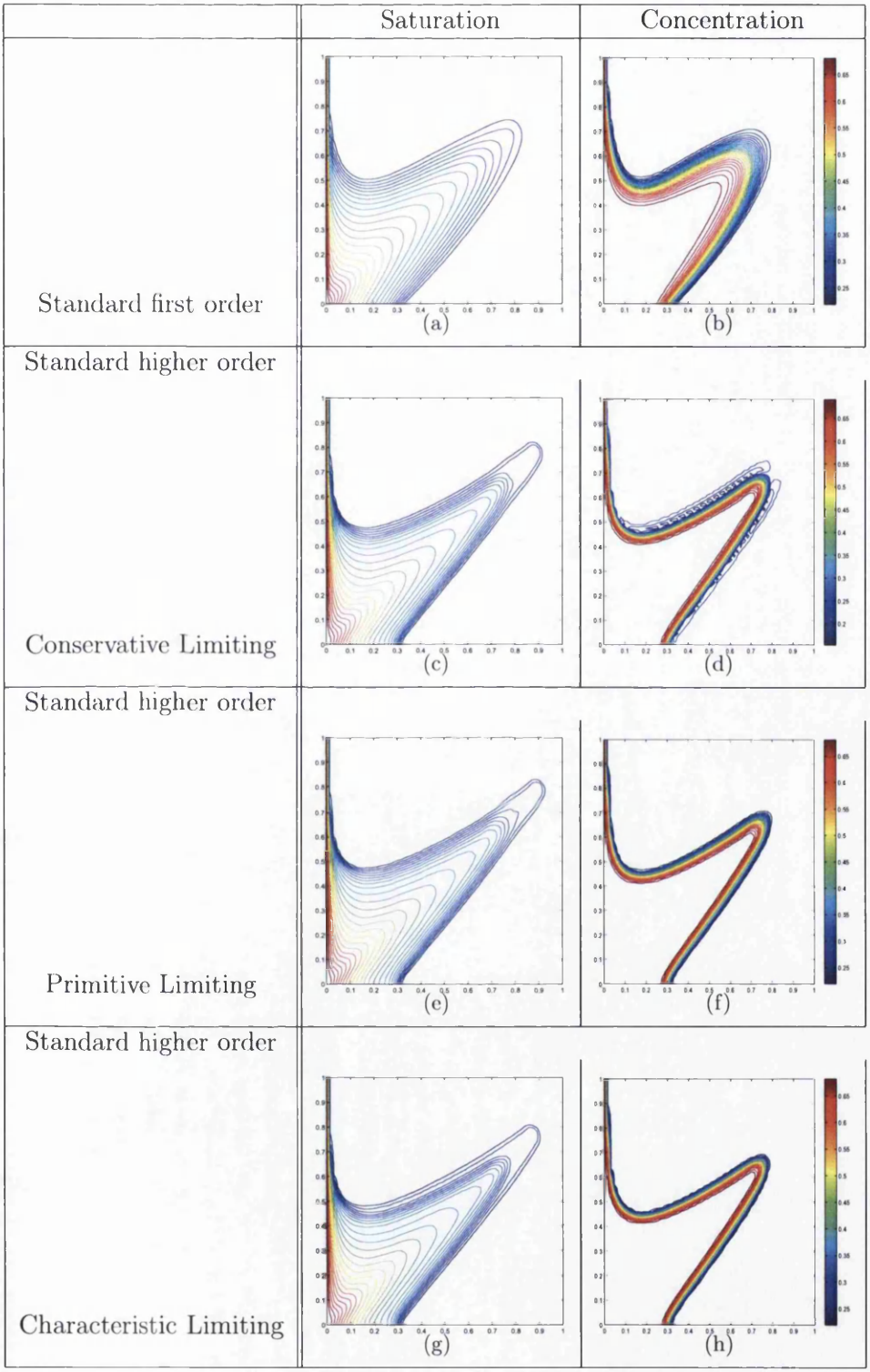

Figure 8.6: Saturation and concentration solutions using standard first order and higher order schemes.

	Saturation	Concentration
Multi-D Tracing with the conservative variables	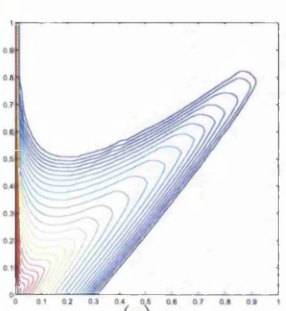 (a)	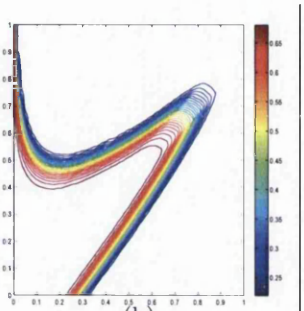 (b)
Multi-D Tracing with the primitive variables	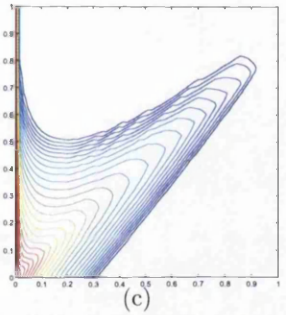 (c)	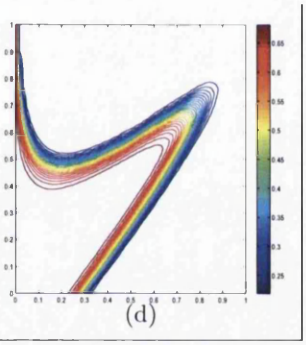 (d)
Multi-D Tracing with the characteristic variables	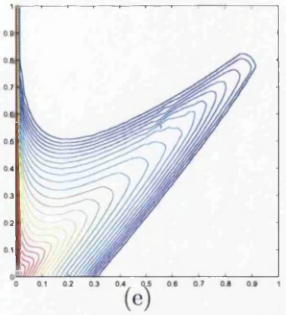 (e)	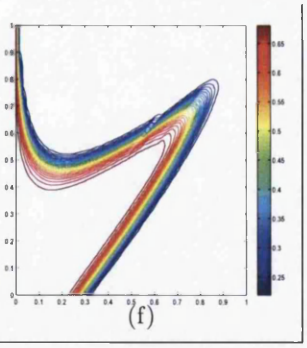 (f)

Figure 8.7: Multidimensional saturation and concentration profiles.

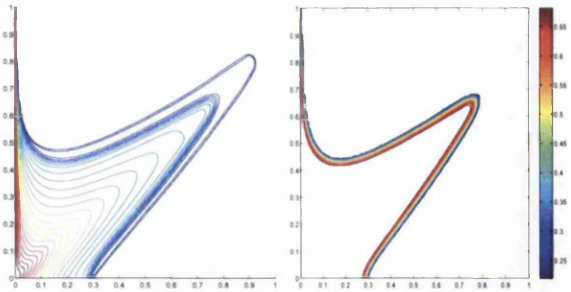

(a) (b)

Figure 8.8: Reference solution on 256x256 Cartesian grid. (a) Saturation profile; (b) concentration profile.

methods where the best results are given when characteristic tracing is used in combination with charateristic upwinding.

Also, both higher order and multidimensional upwind schemes are also introduced for hyperbolic systems where different limiting strategies involving primitive, conservative and characteristic variables are adopted. Numerical test cases involving two phase three component flow demonstrate the benefits of the schemes when compared to standard first order approximations and illustrate the advantage of using the characteristic variables instead of the primitive and conservative variables.

Chapter 9

Cell-Based Multidimensional Schemes on Unstructured Meshes

In this chapter, a cell-based multidimensional flux-consistent upwind formulation is introduced for reservoir simulation on general unstructured grids in two dimensions. The cell-based formulation is presented in 9.1. The motivation for the cell-based formulation is the use of sub-cell fluxes for determining tracing trajectories. Sub-cell fluxes are defined at a finer scale than edge-assembled fluxes which are used in the edge-based formulation. Analogous sub-cell streamline tracing is used in [131] for the streamline method. The cell-based and edge-based methods are contrasted in terms of properties and results in the work below.

9.1 Cell Based Local Multidimensional Approximations

The notation adopted in this section is defined in chapter 7, section 7.2. The same conventions for the flux definitions are used here.
Consider the key edge e and the adjacent cells sharing the edge as shown in Figure 9.1. Let $e1$ and $e2$ denote the control volume sub-faces connected to edge $e(i,j)$ oriented from i to j belonging to the adjacent cells $cell_1$ and $cell_2$.

9.1.1 Formulation using data

First, we present a family of genuinely multidimensional cell-based finite-volume schemes on unstructured grids using a data based formulation.
The left and right states at the integration point of the control volume sub-faces connected to the edge $e(i,j)$ are now defined on triangular cells by:

$$\begin{aligned} \mathbf{S}^n_{L_{e1}} &= (1-\xi_{e1})\mathbf{S}^n_i + \xi_{e1}\mathbf{S}^n_1, \\ \mathbf{S}^n_{R_{e1}} &= (1-\eta_{e1})\mathbf{S}^n_j + \eta_{e1}\mathbf{S}^n_1; \end{aligned} \tag{9.1.1}$$

and on quadrilateral cells by:

$$\begin{aligned} \mathbf{S}^n_{L_{e2}} &= (1-\xi_{e2})\mathbf{S}^n_i + \xi_{e2}\mathbf{S}^n_2, \\ \mathbf{S}^n_{R_{e2}} &= (1-\eta_{e2})\mathbf{S}^n_j + \eta_{e2}\mathbf{S}^n_4. \end{aligned} \tag{9.1.2}$$

The weights are locally defined using the subcell sub-face fluxes as shown in Figure 9.1 with $0 \leq \xi_{eq} \leq 1$ and $0 \leq \eta_{eq} \leq 1$ for $q = 1, Nq$.

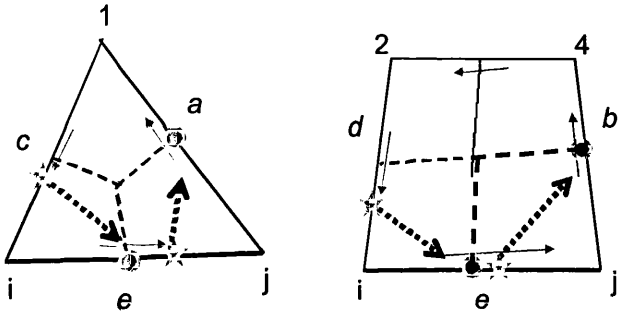

(a) Triangular cell ($cell_1$)

(b) Quadrilateral cell ($cell_2$)

Figure 9.1: Local tracing: local interpolant points are indicated by a star and tracing streamlines are shown in dotted arrows. Grey arrows illustrate sub-cell fluxes calculated at the centre of cell edges.

Linear local positivity analysis

First we shall consider the linear case. Stability of the scheme requires a positive coefficient contribution (convex average) corresponding to each contributing node of the

control volume update. Expanding equation (4.2.17) with respect to the data yields:

$$S_j^{n+1} = \alpha_j S_j^n + \sum_{e=1}^{N_{edV}} \sum_{ic=1}^{Nq} \sum_{k \in cell_{ic}, k \neq j} \alpha_k^{(ic)} S_k^n, \tag{9.1.3}$$

where N_{edV} is the total number of constitutive edges connected to vertex j. The scheme of Equation (9.1.3) is called locally positive if $\alpha_k^{ic} \geq 0$, $\forall\ ic$ and $\forall\ k$ belonging to cell ic such that $k \neq j$ and $\alpha_j \geq 0$ subject to the consistency condition

$$\alpha_j + \sum_{e=1}^{N_{edV}} \sum_{ic=1}^{Nq} \sum_{k \in cell_{ic}, k \neq j} \alpha_k^{(ic)} = 1. \tag{9.1.4}$$

Triangular cell: $cell_1$

The contributions from $cell_1$ to the control volume j update are written as:

$$\begin{aligned} \frac{\tau_j}{\Delta t}(S_j^{n+1} - S_j^n) &= [(1-\xi_{e1})\mathbf{S}_i^n + \xi_{e1}\mathbf{S}_1^n)]F_{T_{e1}}^+ \\ &+ [(1-\eta_{e1})\mathbf{S}_j^n + \eta_{e1}\mathbf{S}_1^n]F_{T_{e1}}^- \\ &+ [(1-\xi_{a1})\mathbf{S}_1^n + \xi_{a1}\mathbf{S}_i^n]F_{T_{a1}}^+ \\ &+ [(1-\eta_{a1})\mathbf{S}_j^n + \eta_{a1}\mathbf{S}_i^n]F_{T_{a1}}^- + ET1, \end{aligned} \tag{9.1.5}$$

where ET1 (extra terms) signifies any contributions coming from cells other than $cell_1$. The associated weights corresponding to node i are expressed as:

$$\alpha_i^{(1)} = \frac{\Delta t}{\tau_j}((1-\xi_{e1})F_{T_{e1}}^+ + \xi_{a1}F_{T_{a1}}^+ + \eta_{a1}F_{T_{a1}}^-). \tag{9.1.6}$$

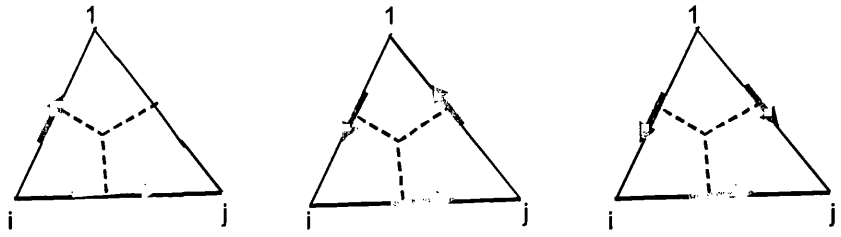

(a) Stagnation point (b) $\beta_1 = \frac{1}{2}$ (c) $\beta_1 = 1$

Figure 9.2: Weighting factor for triangular cells.

The purpose of this subsection is to derive conditions governing interpolation weights over each cell sharing the key edge e, so that the scheme satisfies the local positivity

condition.

For the scheme of Equations (9.1.1) to satisfy the local positivity condition on, a necessary condition is:

$$\xi_{e1}F^{+}_{T_{e1}} - \eta_{a1}F^{-}_{T_{a1}} \leq F^{+}_{T_{e1}} + \xi_{a1}F^{+}_{T_{a1}}. \tag{9.1.7}$$

Equation (9.1.7) implies that in the case where $F^{+}_{T_{e1}} = 0$ i.e. the sub-face flux is oriented from j to i, the upwind information with respect to the edge c does not originate from $cell_1$ and inequality in Equation (9.1.7) reduces to

$$-\eta_{a1}F^{-}_{T_{a1}} \leq \xi_{a1}F^{+}_{T_{a1}}, \tag{9.1.8}$$

which yields $\eta_{a1} = 0$ when the sub-face flux $F_{T_{a1}} < 0$ and is oriented from node j to node 1.

Applying the same reasoning while considering the control volume i instead of j, this observation leads to the first constraint at a stagnation point namely:

Theorem 9.1.1

if $F_{T_{e1}}$ is oriented from i to j, and $F_{T_{c1}}$ is pointing from i to 1 as illustrated in Figure 9.2 then $\xi_{e1} = 0$. This means that at a stagnation point the standard single-point upstream weighting scheme is recovered locally on the control volume sub-face belonging to $cell_1$.

Proof The coefficient of node 1 in the contributions from $cell_1$ to the control volume i update in the case where both subcell fluxes $F_{T_{e1}}$ and $F_{T_{c1}}$ are leaving the control volume i reduces to:

$$-\xi_{e1}F^{+}_{T_{e1}}. \tag{9.1.9}$$

Local positivity condition requires $\xi_{e1} = 0$.

In the case where $F_{T_{e1}} = F^{+}_{T_{e1}} > 0$, $F_{T_{a1}} = F^{-}_{T_{a1}} < 0$ i.e. $F_{T_{e1}}$ is oriented from i to j, $F_{T_{a1}}$ is oriented from node j to the node 1 as shown in Figure 9.2(a), a sufficient condition for the inequality of Equation (9.1.7) to be satisfied is that:

$$\xi_{e1}|F_{T_{e1}}| + \eta_{a1}|F_{T_{a1}}| \leq |F_{T_{e1}}|. \tag{9.1.10}$$

Setting the weights to be proportional to the ratio of the inward and outward fluxes, i.e.

$$\eta_{a1} = \beta_1 \frac{F_{T_{e1}}}{|F_{T_{a1}}|} \text{ and } \eta_{a1} \leq 1 \tag{9.1.11}$$

yields

$$\beta_1 \leq \frac{1}{2} \text{ and } \xi_{e1} \leq \frac{1}{2}. \tag{9.1.12}$$

Notice here that the condition of Equation (9.1.12) is relaxed when the sub-cell flux $F_{T_{a1}}$ is positive i.e. $F^-_{T_{a1}} = 0$ (Figure 9.2(b)) and the inequality 9.1.12 becomes

$$\beta_1 \leq 1 \text{ and } \xi_{e1} \leq 1. \tag{9.1.13}$$

Furthermore, define the flux ratio R_{e1} as

$$R_{e1} = \frac{F_{T_{c1}}}{F_{T_e 1}}, \tag{9.1.14}$$

then, the weighting factor takes the form:

$$\xi_{e1} \leq \beta_1 \min(1, \max(R_{e1}, 0)) \text{ with } \beta_1 = \begin{cases} 1/2 \text{ if } F_{T_{c1}} < 0, \\ 1 \text{ otherwise.} \end{cases} \tag{9.1.15}$$

Quadrilateral cell: $cell_2$

The contributions from $cell_2$ to the control volume j update are written as:

$$\begin{aligned} \frac{\tau_j}{\Delta t}(S_j^{n+1} - S_j^n) &= [(1-\xi_{e2})\mathbf{S}_i^n + \xi_{e2}\mathbf{S}_2^n)]F^+_{T_{e2}} \\ &+ [(1-\eta_{e2})\mathbf{S}_j^n + \eta_{e2}\mathbf{S}_4^n]F^-_{T_{e2}} \\ &+ [(1-\xi_{b2})\mathbf{S}_4^n + \xi_{b2}\mathbf{S}_2^n]F^+_{T_{b2}} \\ &+ [(1-\eta_{b2})\mathbf{S}_j^n + \eta_{b2}\mathbf{S}_i^n]F^-_{T_{b2}} + ET2, \end{aligned} \tag{9.1.16}$$

where ET2 (extra terms) signifies any contributions coming from cells other than $cell_2$.

The associated weights corresponding to node i are expressed as:

$$\alpha_i^{(2)} = \frac{\Delta t}{\tau_j}((1-\xi_{e2})F^+_{T_{e2}} + \eta_{b2}F^-_{T_{b2}}). \tag{9.1.17}$$

For the scheme of Equations (9.1.2) to satisfy the local positivity condition, a necessary condition is:

$$\xi_{e2}F^+_{T_{e2}} - \eta_{b2}F^-_{T_{b2}} \leq F^+_{T_{e2}}. \tag{9.1.18}$$

Following a similar argument as for a triangular cell, a local positivity constraint at a stagnation point is established.

Theorem 9.1.2

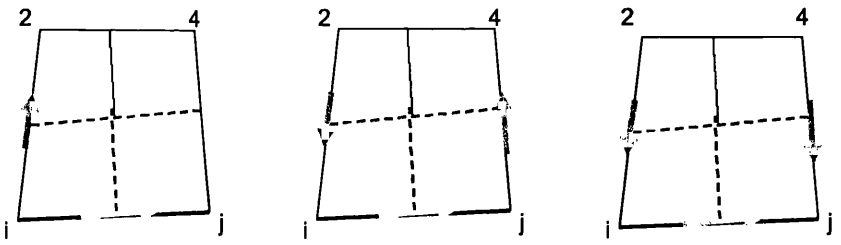

(a) Stagnation point (b) $\beta_2 = \frac{1}{2}$ (c) $\beta_2 = 1$

Figure 9.3: Weighting factor for quadrilateral cells.

if $F_{T_{e2}}$ is oriented from i to j, and $F_{T_{d2}}$ is pointing from i to 2 as illustrated in Figure 9.3(a) then $\xi_{e2} = 0$. This means that at a stagnation point the standard single-point upstream weighting scheme is recovered locally on the control volume sub-face belonging to $cell_2$.

Proof The coefficient of node 2 in the contributions from $cell_2$ to the control volume i update in the case where both subcell fluxes $F_{T_{e2}}$ and $F_{T_{d2}}$ are leaving the control volume i reduces to:

$$-\xi_{e2} F^{+}_{T_{e2}}. \tag{9.1.19}$$

Local positivity condition requires $\xi_{e2} = 0$.

In the case where $F_{T_{e2}} = F^{+}_{T_{e2}} > 0$, $F_{T_{b2}} = F^{-}_{T_{b2}} < 0$ i.e. $F_{T_{e2}}$ is oriented from i to j, $F_{T_{b2}}$ is oriented from node j to the node 4 as shown in Figure 9.3(b), a sufficient condition for the inequality Equation (9.1.18) to be satisfied is that:

$$\xi_{e2}|F_{T_{e2}}| + \eta_{b2}|F_{T_{b2}}| \leq |F_{T_{e2}}|. \tag{9.1.20}$$

Setting the weights to be proportional to the ratio of the inward and outward fluxes, i.e.

$$\eta_{b2} = \beta \frac{F_{T_{e2}}}{F_{T_{b2}}} \text{ with } \eta_{b2} \leq 1, \tag{9.1.21}$$

yields

$$\beta_2 \leq \frac{1}{2} \text{ and } \xi_{e2} \leq \frac{1}{2}. \tag{9.1.22}$$

Note here that the condition Equation (9.1.22) is relaxed when the sub-cell flux $F_{T_{b2}}$ is positive i.e. $F^{-}_{T_{b2}} = 0$ (Figure 9.3(c)) and the inequality Equation (9.1.22) becomes

$$\beta_2 \leq 1 \text{ and } \xi_{e2} \leq 1. \tag{9.1.23}$$

Furthermore, define the flux ratio R_{e2} as

$$R_{e2} = \frac{F_{T_{d2}}}{F_{T_e 2}}, \tag{9.1.24}$$

then, the weighting factor takes the form:

$$\xi_{e2} \leq \beta_2 \min(1, \max(R_{e2}, 0)) \text{ with } \beta_2 = \begin{cases} 1/2 \text{ if } F_{T_{b2}} < 0, \\ 1 \text{ otherwise.} \end{cases} \tag{9.1.25}$$

Stability

The associated weights of node j can be expressed in the form:

$$\alpha_j = 1 + \frac{\Delta t}{\tau_j} \sum_{e=1}^{NedV} \sum_{ic=1,Nq} (1 - \eta_{e_{ic}}) F^-_{T_{e_{ic}}}, \tag{9.1.26}$$

for both triangular and quadrilateral grids. The stability condition is derived from Equation (9.1.26) which shows that the scheme permits a larger CFL number than the standard upwind method if $\eta_{e_{ic}}$ are not all equal to zero.

$$\Delta t < -\frac{\tau_j}{\sum_{e=1}^{NedV} \sum_{ic=1}^{Nq} (1 - \eta_{e_{ic}}) F^-_{T_{e_{ic}}}}. \tag{9.1.27}$$

Again the use of directional information will enhance stability of the method.

9.1.2 Relation between Edge and Cell based tracing formulations

Consider a Cartesian grid with $F_{T_{e1}} = F_{T_{e2}} = \frac{F_{T_e}}{2} \geq 0$, the local weighting factors in the cell based formulation are written as:

$$\begin{aligned} \xi_{e1} &\leq \beta_1 \min(1, \max(\frac{F_{T_d}}{F_{T_e}}, 0)), \\ \xi_{e2} &\leq \beta_2 \min(1, \max(\frac{F_{T_c}}{F_{T_e}}, 0)). \end{aligned} \tag{9.1.28}$$

Summing the contribution of node i in the update of the j^th control volume over the cells $cell_1$ and $cell_2$ sharing the edge e, the cell based formulation could be interpreted as an edge based formulation with a corresponding global weighting factor:

$$\begin{aligned} \xi_e^{Cellbased} &= \frac{1}{2}(\xi_{e1} + \xi_{e2}) \\ &= \frac{1}{2}(\beta_1 + \beta_2) \min(1, \frac{\beta_1}{\beta_1 + \beta_2} \max(\frac{F_{T_d}}{F_{T_e}}, 0) + \frac{\beta_2}{\beta_1 + \beta_2} \max(\frac{F_{T_c}}{F_{T_e}}, 0)) \end{aligned} \tag{9.1.29}$$

where β_k, $k = 1, 2$ takes the values, 0, 1/2 or 1 depending on the subcell flux directions as discussed in the previous section. Note here that the weighting factor in the edge based formulation takes the form:

$$\xi_e^{Edgebased} = \beta \min(1, \frac{\max(F_{T_c}, F_{T_d}, 0)}{F_{T_e}}), \tag{9.1.30}$$

where the range of values for β is included in {0, 1/3, 1/2}. From Equations (9.1.29) and (9.1.30), equivalence between edge-based and cell-based formulations is established on Cartesian grids.

9.1.3 Nonlinear Flux formulation

As for the edge based multidimensional higher-order reconstructions, we present two cell based formulations analogous to the schemes introduced in chapter 7, section 7.2. However for unstructured grids, the cell-based scheme proves to be overall the most robust and relies on sub-cell flux tracing therefore uses finer scale information.

Nonlinear Flux of Multi-dimensional Data

The first formulation involves multi-dimensional upwind data where we define the generalized flux for e.g. triangle cell 1 by:

$$\begin{aligned} f(S_L^n) &= f\big((1-\xi_{e_1})S_i^n + \xi_{e_1} S_1^n\big), \\ f(S_R^n) &= f\big((1-\eta_{e_1})S_j^n + \eta_{e_1} S_1^n\big). \end{aligned}$$

Nonlinear Multi-dimensional Flux

The second formulation involves the multi-dimensional upwind flux where we define the generalized flux for e.g. triangle cell 1 by:

$$\begin{aligned} f(S_L^n) &= (1-\xi_{e_1}) f(S_i^n) + \xi_{e_1} f(S_1^n), \\ f(S_R^n) &= (1-\eta_{e_1}) f(S_j^n) + \eta_{e_1} f(S_1^n). \end{aligned}$$

Here, we have used conditions of Equations (9.1.4) and (9.1.15) for stability in our calculations.

9.2 Numerical Results

The test cases involve two phase flow (oil-water). Initial oil saturation is prescribed and water is injected. Water saturation contours are shown in each case. Solid wall (zero normal flow) boundary conditions are applied on all solid boundaries of each reservoir domain. In all cases, flow rate is specified at the (inflow) injector and pressure is prescribed at the (outflow) producer and a consistent Darcy flux approximation is used.

Results involve full tensor coefficient velocity fields, with strong cross terms that induce significant cross-flow across grid cells which also adds to the full tensor effect due to the unstructured nature of the grid.

Three different cases are presented involving full and diagonal permeability tensors in homogeneous and heterogeneous media. Linear and nonlinear fluxes are considered and results are computed using a range of structured and unstructured triangular and quadrilateral grids.

9.2.1 Case 1: Linear Full Tensor Quarter Five Spot

The first case involves a linear Buckley Leverett flux, corresponding with linear relative permeabilities. Injection and production wells are located along opposite sides of the rectangular domain. Total mobility is constant and the permeability tensor is assumed to be diagonal isotropic so that the pressure is solved exactly (in this particular case) using the consistent Darcy flux. Thus any error in the saturation field is entirely due to the convective flux approximation. Water saturation contours are shown at 0.5 pore volumes injected (PVI).

The results are computed on an unstructured triangular Delaunay mesh shown in Figure 9.4(a). The standard single-point upstream weighting result (Figure 9.4(b)) shows that the front is largely diffused. In contrast, the multidimensional schemes (Figures 9.4(c) and 9.4(d)) provide sharper resolution and improve the symmetry of the problem about the diagonal while reducing cross-flow spread of the saturation front.

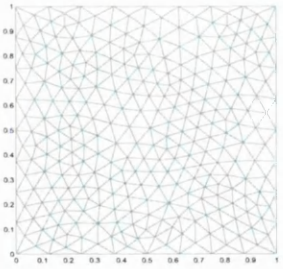

(a) Delaunay mesh 290 nodes

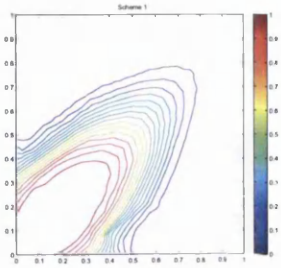

(b) Single point upwind

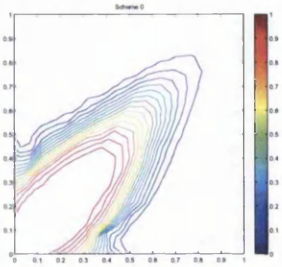

(c) Multi-D Edge-based

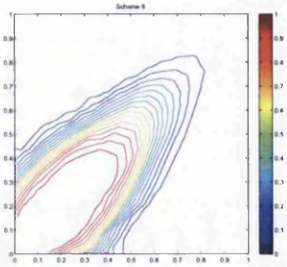

(d) Multi-D Cell-based

Figure 9.4: Case 1 - Saturation profiles for the linear quarter five spot problem with full tensor at 45 degrees.

9.2.2 Case 2: Nonlinear Full Tensor Piston Flow

The second case involves a quadratic Buckley Leverett flow subject to fluid injection on the left hand boundary and specified pressure on the right hand boundary and a full homogeneous permeability tensor with principal axes oriented at 45 degrees to the reservoir domain with 10 to 1 anisotropy ratio. The water and oil relative permeabilities are respectively $k_{rw} = S^2$ and $k_{ro} = (1-S)^2$ and the flow mobility ratio is set to unity $M = 1$. The results are first computed on the unstructured triangular grid shown in Figure 9.5(a). The nonlinear case highlights the difference between the flux of Multi-D data and Multi-D flux. The reference solution on a 64x64 Cartesian grid is shown in Figure 9.6(a).
The results obtained using standard single-point upstream weighting are shown in Figures 9.5(b) and 9.5(c) and those obtained using the data based multidimensional wave-oriented higher dimensional upwind scheme are shown in Figures 9.6(b) edge based and 9.6(d) cell based. The multidimensional flux results are shown in Figures 9.6(c) (edge-based) and 9.6(e)(cell-based) on the unstructured triangular grid.
The standard first order results are quite smooth whereas the results obtained with the

multidimensional schemes show reduced grid dependence and provide considerable improvement of front resolution with a clearer indication of the flow pattern, particularly for the Multi-D cell-based schemes with results that are most consistent with the problem.

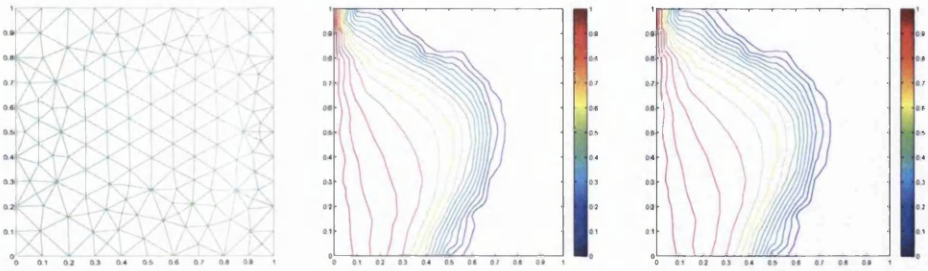

(a) Grid (b) SPU Edge-based (c) SPU Cell-based

Figure 9.5: Case 2 - Standard first order saturation profiles.

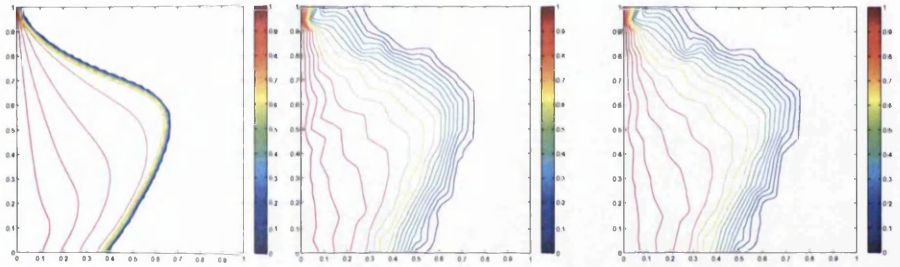

(a) Reference Solution on a 64x64 Cartesian Grid (b) Flux of Multi-D Data Edge-based (c) Multi-D Flux Edge-based

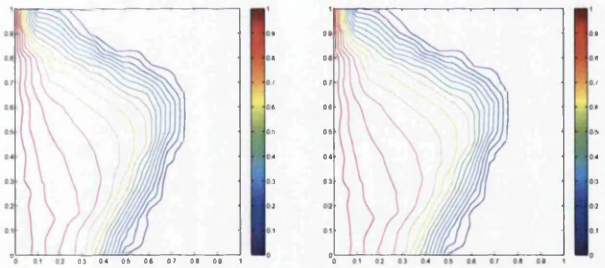

(d) Flux of Multi-D Data Cell-based (e) Multi-D Flux Cell-based

Figure 9.6: Case 2 - Multi-Dimensional first order saturation profiles on triangular mesh.

The equivalent unstructured quadrilateral grid (Figure 9.7(a)) which has the same vertices as the triangular grid of Figure 9.5(a) provides the second part of this test case. First, we

show a comparison between standard first order edge-based and cell-based schemes which highlights a difference between the two types of formalism that can become apparent even with standard first order upwind (Figures 9.7(b),(c)). The first order results show strong local grid orientation effect. The multidimensional comparison clearly demonstrates that cell-based Multi-D (Figure 9.8) consistently provides the best results.

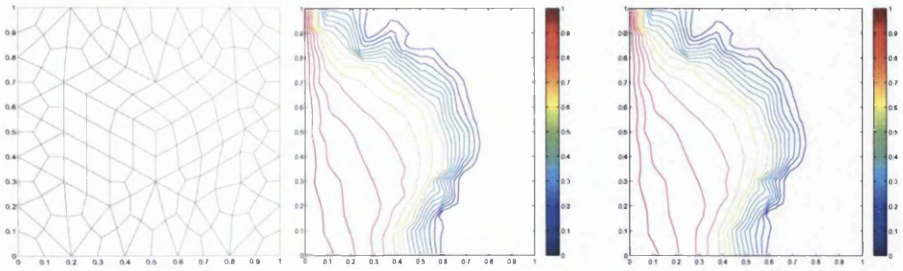

(a) Grid (b) SPU Edge-Based (c) SPU Cell-Based

Figure 9.7: Case 2 - Standard first order saturation profiles on quad-mesh.

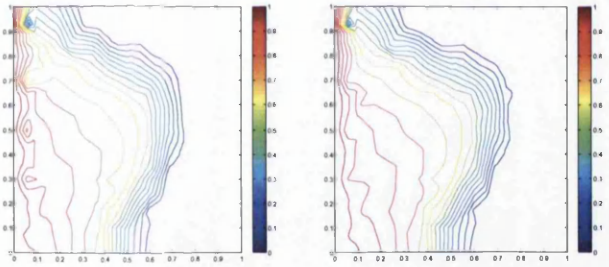

(a) Multi-D Data Edge-based (b) Multi-D Flux Edge-based

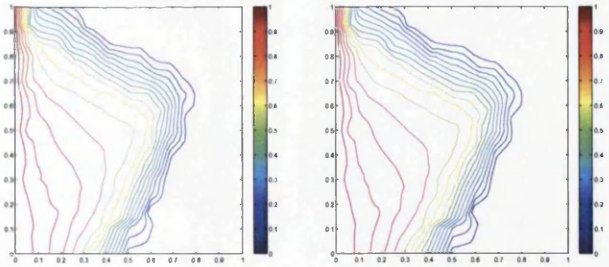

(c) Flux of Multi-D Data Cell-based (d) Multi-D Flux Cell-based

Figure 9.8: Case 2 - Multi-Dimensional first order saturation profiles on quad-mesh.

9.2.3 Case 3: Piston Flow in a Heterogeneous Medium

The third case involves linear injection into a heterogeneous medium where injection and production wells are located along opposite sides of the rectangular domain. Results are obtained using a 60x220 uniform grid. The permeability distribution is from Layer 3 of Model 2 of the 10th SPE Comparative Solution Project [28]. Figure 9.9 shows the logarithm of the permeability field. Water saturation contours are shown at 0.005 pore

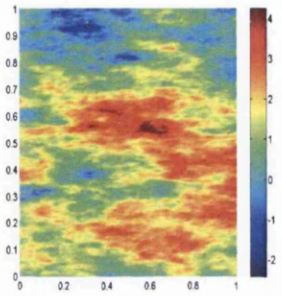

Figure 9.9: Logarithm of the permeability field.

volumes (PV) injected. Figure 9.10 shows saturation profiles computed with the standard single-point upwind method (Figure 9.10(a)). The first order Multi-D edge based (Figure 9.10(b)) and cell based (Figure 9.10(c)) schemes provide similar and much improved solution resolution compared to the standard method. The Multi-D schemes provide the best overall resolution of the finger like features of the solution Figures 9.10(e),(f).

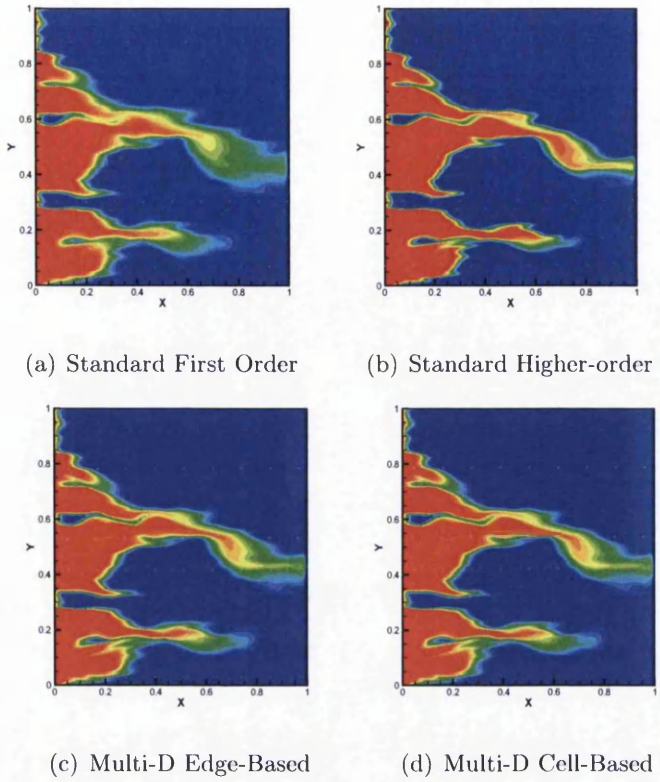

(a) Standard First Order (b) Standard Higher-order

(c) Multi-D Edge-Based (d) Multi-D Cell-Based

Figure 9.10: Case 3 - Saturation profiles for the heterogeneous Case.

9.3 Conclusions

Families of cell-based multidimensional upwind formulations are presented for hyperbolic conservation laws on structured and unstructured quadrilateral and triangular grids. The methods are coupled with consistent and efficient continuous Darcy flux approximations. The schemes are locally conservative, conditions for positivity are derived for linear convection. The Multi-D methods permit higher CFL numbers than the standard upwind scheme.

The new methods are compared with single point upstream weighting for two-phase flow problems. The tests are conducted on both structured and unstructured grids and involve full-tensor coefficient velocity fields. The comparisons demonstrate the benefits of multidimensional schemes in terms of improved front resolution together with significant reduction in cross-wind diffusion. While unstructured edge based formulation reduces local crossflow grid orientation and distortion effects compared to single point upwind,

the unstructured cell based multidimensional schemes yield the best results for the test cases presented.

Chapter 10

Higher Order Multidimensional Schemes on Unstructured Meshes

In this chapter, two new higher order families of multidimensional upwind schemes are presented for reservoir simulation on general unstructured grids in two dimensions. The higher-order multi-dimensional convection schemes are coupled with existing continuous Darcy-flux approximations, (chapter 4, section 4.2.1). Although the multidimensional schemes presented in chapters 6, 7 and 9 effectively reduce the cross-wind numerical diffusion in 2-D on general unstructured grids, they do not cure the longitudinal numerical diffusion along the coordinate lines (see section 6, 6.3). These schemes are further enhanced by the development of a higher order multidimensional formulation and the net result is a family of higher order multidimensional schemes that minimizes both crosswind diffusion and coordinate line diffusion.

Standard higher order approximations are summarized in section 10.1 where an extension to general unstructured quadrilateral meshes is presented. Section 10.2 is dedicated to the formulation of cell-wise and edge-wise families of higher order multidimensional schemes. Two-phase flow results are presented in section 10.3 that demonstrate the advantages of the new higher-order higher-dimensional flux-continuous formulation.

10.1 Higher-Order Multi-Phase Flow Approximations on Unstructured Meshes

In this chapter, we recall the higher order reconstructions presented in chapter 5 for distorted triangular meshes and present an extension of theses schemes to quadrilateral meshes.

As detailed in chapter 5, section 5.2, the higher order reconstructions left and right hand side states relative to the mid-point of each edge e (along which flux is to be defined) is defined by expansions about the edge vertices at i and k, Figure 10.1. A local maximum principle is enforced via the use of limiters that account for the non-uniformity of the mesh (chapter 5, section 5.3) in order to prevent the introduction of spurious extrema in the solution.

Referring to Figure 5.1 the left and right states $\mathbf{S_L}$ and $\mathbf{S_R}$ at the midpoint of the *key* edge e (joining vertices i and k) are expressed as

$$\mathbf{S_L} = \mathbf{S}_i + \frac{1}{2}\Phi^+ \Delta \mathbf{S}_{ki}, \tag{10.1.1}$$

where $\Phi^+ = \phi(\mathbf{r}^+_{ki})$ is a function of

$$r^+_{ki} = \frac{\Delta \mathbf{S}_{iu}/\Delta r_{iu}}{\Delta \mathbf{S}_{ki}/\Delta r_{ki}}. \tag{10.1.2}$$

and

$$\mathbf{S_R} = \mathbf{S}_k - \frac{1}{2}\Phi^- \Delta \mathbf{S}_{ki}, \tag{10.1.3}$$

where $\Phi^- = \phi(\mathbf{r}^-_{ki})$ is a function of

$$r^-_{ki} = \frac{\Delta \mathbf{S}_{dk}/\Delta r_{dk}}{\Delta \mathbf{S}_{ki}/\Delta r_{ki}}. \tag{10.1.4}$$

Directional differences are constructed by extrapolating along the *key* edge defined by vector $\Delta \mathbf{r}_{ki}$ in the respective upstream and downstream directions, see arrows in Figure 5.1. Extrapolation of the respective upstream and downstream data is constrained such that a local maximum principle is imposed. The upstream triangle is defined using nodes $i, 1, 2$ and is labelled T_U. Similarly the down stream triangle $k, 3, 4$ is labelled T_D. The space vector corresponding to edge e ($\Delta \mathbf{r}_{ki}$) is extrapolated into the respective triangles T_U, T_D, see arrows in Figure 10.1. This is illustrated further with respect to vertex i. The edge vector is extrapolated to the point of intersection u and d respectively, on the opposite edge of the triangle T_U and T_D respectively as shown in Figure10.1.

In the following, we refer to this formulation as the standard higher-order scheme.

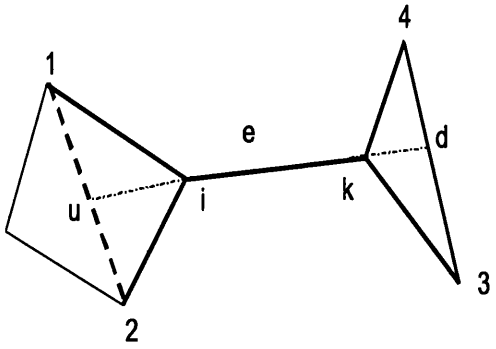

(a)

Figure 10.1: Higher order support for unstructured grids.

10.2 Higher Order Multi-Dimensional Schemes

The higher order multidimensional upwind schemes are comprised of two steps:

1. higher-order reconstruction of the data that corrects the directional diffusion of the approximation, followed by

2. truly multi-dimensional upwind approximation on the higher order data.

Let $\tilde{S}_{Le}$ ($\tilde{S}_{Re}$ respectively) define the left (right respectively) state higher order reconstruction with respect to the edge e given above, in the following, $\bar{S}_{Le}$ ($\bar{S}_{Re}$ respectively) denotes the left (the right respectively) higher order multidimensional saturation interpolant with respect to the edge $e(i,j)$.

10.2.1 Edge Based Higher-Order Multi-Dimensional Approximation

Formulation using Data

Referring to Figure 10.2, the edge-based Higher order Multidimensional data based formulation is written as

$$\begin{aligned} \bar{S}_{Le} &= (1-\xi_e)\tilde{S}_{Le} + \xi_e[(1-\chi_e)\tilde{S}_{Lc} + \chi_e\tilde{S}_{Ld}], \\ \bar{S}_{Re} &= (1-\eta_e)\tilde{S}_{Re} + \eta_e[(1-\chi_e)\tilde{S}_{Lb} + \chi_e\tilde{S}_{Ra}]. \end{aligned} \tag{10.2.1}$$

The weighting coefficients ξ and η are defined using Equation (7.2.13).

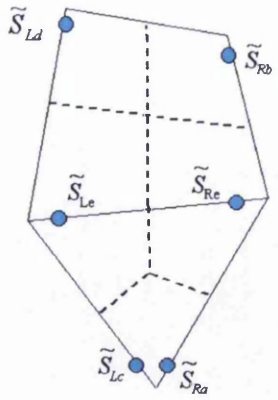

Figure 10.2: Higher order reconstructed data at the edges, dots illustrate the higher order data at the control volume faces.

Nonlinear Flux Formulation

Similar to the first order multidimensional low-order schemes presented in chapters 6 and 7, nonlinear flux is treated using two formulations, where now the multidimensional reconstructions involve the higher order states instead of the first order data.

Nonlinear Flux of Multi-dimensional Higher-order Data The second formulation involves the multi-dimensional upwind flux correction of higher-order data reconstruction where the generalized flux is written as:

$$\begin{aligned} F(\bar{S}_{Le}) &= F((1-\xi_e)\tilde{S}_{Le} + \xi_e[(1-\chi_e)\tilde{S}_{Lc} + \chi_e\tilde{S}_{Ld}]), \\ F(\bar{S}_{Re}) &= F((1-\eta_e)\tilde{S}_{Re} + \eta_e[(1-\chi_e)\tilde{S}_{Rb} + \chi_e\tilde{S}_{Ra}]). \end{aligned} \tag{10.2.2}$$

Nonlinear Multi-dimensional Flux of Higher-order Data The first formulation involves multi-dimensional higher-order upwind data reconstruction where we define the generalized flux by:

$$\begin{aligned} F(\bar{S}_{Le}) &= (1-\xi_e)F(\tilde{S}_{Le}) + \xi_e[(1-\chi_e)F(\tilde{S}_{Lc}) + \chi_e F(\tilde{S}_{Ld})], \\ F(\bar{S}_{Re}) &= (1-\eta_e)F(\tilde{S}_{Re}) + \eta_e[(1-\chi_e)F(\tilde{S}_{Rb}) + \chi_e F(\tilde{S}_{Ra})]. \end{aligned} \tag{10.2.3}$$

Here, we have used conditions of Equations (7.2.2), (6.3.10) and (7.2.13) for stability in our calculations.

10.2.2 Cell-Based Higher-Order Multi-Dimensional Approximation

Formulation using data

Cell-based Higher order Multidimensional data based reconstruction takes the form:

$$\bar{S}_{Le1} = (1-\xi_{e1})\tilde{S}_{Le1} + \xi_{e1}\tilde{S}_{Lc1}, \tag{10.2.4}$$

$$\bar{S}_{Re1} = (1-\eta_{e1})\tilde{S}_{Re1} + \eta_{e1}\tilde{S}_{Ra1}, \tag{10.2.5}$$

with respect to $cell_1$ and

$$\bar{S}_{Le2} = (1-\xi_{e2})\tilde{S}_{Le2} + \xi_{e2}\tilde{S}_{Ld2}, \tag{10.2.6}$$

$$\bar{S}_{Re2} = (1-\eta_{e2})\tilde{S}_{Re2} + \eta_{e2}\tilde{S}_{Rb2}, \tag{10.2.7}$$

with respect to $cell_2$. The weighting coefficients ξ_{e1} and η_{e1} are defined using Equation (9.1.7) whereas ξ_{e2} and η_{e1} are defined using Equation (9.1.18).

Nonlinear Flux formulation

As for the edge-based multidimensional higher-order reconstructions, we present two cell based analogous formulations to the schemes introduced in section 10.1.

Nonlinear Flux of Multi-dimensional Higher-order Data The second formulation involves the multi-dimensional upwind flux correction of higher-order data reconstruction where we define the generalized flux by:

$$F(\bar{S}_{Le1}) = F((1-\xi_{e1})\tilde{S}_{Le1} + \xi_{e1}\tilde{S}_{Lc1}), \tag{10.2.8}$$

$$F(\bar{S}_{Re1}) = F((1-\eta_{e1})\tilde{S}_{Re1} + \eta_{e1}\tilde{S}_{Ra1}),$$

with respect to the $cell_1$ and

$$F(\bar{S}_{Le2}) = F((1-\xi_{e2})\tilde{S}_{Le2} + \xi_{e2}\tilde{S}_{Ld2}), \tag{10.2.9}$$

$$F(\bar{S}_{Re2}) = F((1-\eta_{e2})\tilde{S}_{Re2} + \eta_{e2}\tilde{S}_{Rb2}),$$

with respect to $cell_2$.
Equations (9.1.4), (9.1.15) and (9.1.25) have been used for stability.

Nonlinear Multi-dimensional Flux of Higher-order Data The first formulation involves multi-dimensional higher-order upwind data reconstruction where the generalized flux is defined by:

$$\begin{aligned} F(\bar{S}_{Le1}) &= (1-\xi_{e1})F(\tilde{S}_{Le1}) + \xi_{e1}F(\tilde{S}_{Lc1}), \\ F(\bar{S}_{Re1}) &= (1-\eta_{e1})F(\tilde{S}_{Re1}) + \eta_{e1}F(\tilde{S}_{Ra1}), \end{aligned} \tag{10.2.10}$$

with respect to the $cell_1$ and

$$\begin{aligned} F(\bar{S}_{Le2}) &= (1-\xi_{e2})F(\tilde{S}_{Le2}) + \xi_{e2}F(\tilde{S}_{Ld2}), \\ F(\bar{S}_{Re2}) &= (1-\eta_{e2})F(\tilde{S}_{Re2}) + \eta_{e2}F(\tilde{S}_{Rb2}), \end{aligned} \tag{10.2.11}$$

with respect to $cell_2$. Again, here, we have used Equations (9.1.4), (9.1.15) and (9.1.25) for stability in our calculations.

10.3 Numerical Results

The test cases involve two phase flow (oil-water). Initial oil saturation is prescribed and water is injected. Water saturation contours are shown in each case. Solid wall (zero normal flow) boundary conditions are applied on all solid boundaries of each reservoir domain. In all cases, flow rate is specified at the (inflow) injector and pressure is prescribed at the (outflow) producer and a consistent Darcy flux approximation is used.
Results involve full tensor coefficient velocity fields, with strong cross terms that induce significant cross-flow across grid cells which also adds to the full tensor effect due to the unstructured nature of the grid.
Four different cases are presented involving full and diagonal permeability tensors in homogeneous and heterogeneous media. Linear and nonlinear fluxes are considered and results are computed using a range of structured and unstructured triangular and quadrilateral grids. The flow mobility ratio is set to unity $M = 1$ for all cases presented here.

10.3.1 Case 1: Linear Full Tensor Quarter Five Spot

The first case is a study of a quarter five spot problem involving a linear Buckley Leverett flux.Quarter five spot boundary conditions are imposed together with an anisotropic full tensor permeability field with principal axes oriented at 45 degrees to the reservoir domain with 10 to 1 anisotropy ratio.

Water saturation contours are shown at 0.25 pore volumes injected (PVI) for the same CFL number equal to 0.4.

The results are computed on an unstructured triangular Delaunay mesh shown in Figure 10.3(a). The standard single-point upstream weighting result (Figure 10.3(b)) shows that the front is largely diffused. In contrast, the multidimensional schemes (Figures 10.3(c) and 10.3(d)) provide sharper resolution and improve the symmetry of the solution about the diagonal while predicting an earlier breakthrough with minimal cross-flow spread. We note that the full tensor effect due to the grid is noticeably attenuated in the multidimensional wave oriented results.

Higher-order results are shown in Figures 10.3(e), (g) and (h). The higher order Multi-D edge-based (Figure 10.3(f)) and cell-based (Figure 10.3(g)) both show improved resolution of the front compared to the standard higher order results (10.3(e)), though the cell-based method shows the best overall improvement in resolution, particularly near the boundaries.

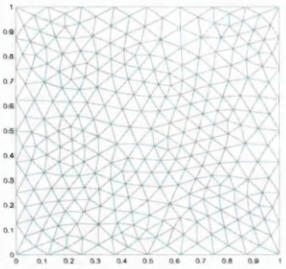

(a) Delaunay mesh 290 nodes

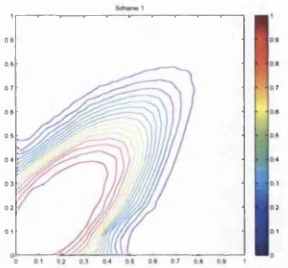

(b) Single point upwind

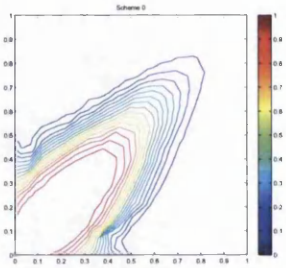

(c) Multi-D Edge-based

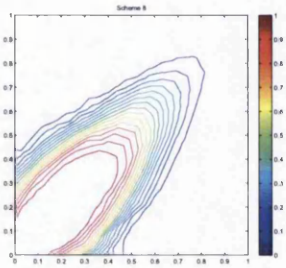

(d) Multi-D Cell-based

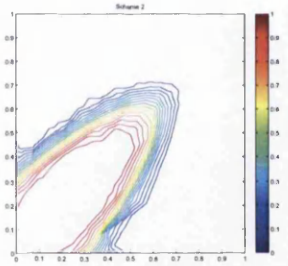

(e) Standard Higher-order

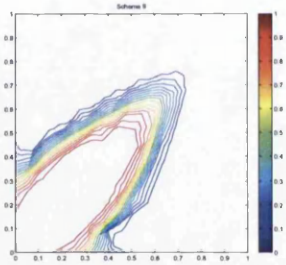

(f) Higher-order Multi-D Edge-based

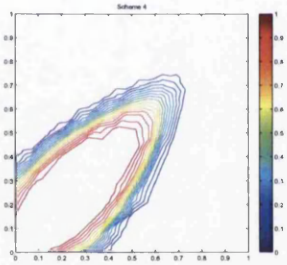

(g) Higher-order Multi-D Cell-based

Figure 10.3: Case 1 - Saturation profiles for the linear quarter five spot problem with full tensor at 45 degrees.

10.3.2 Case 2: Full Tensor Point Source to Point Sink

The second case is a study of local grid orientation effect for a source sink problem involving a linear Buckley Leverett flux and a diagonal isotropic permeability tensor. Results are computed on a distorted triangular grid as shown in Figure 10.4(a). Reference solution on a 81x81 Cartesian grid is depicted in Figure 10.4(b).

The permeability tensor is assumed to be diagonal isotropic so that the pressure field is essentially Laplacian in this case. Injection and production wells are located half way

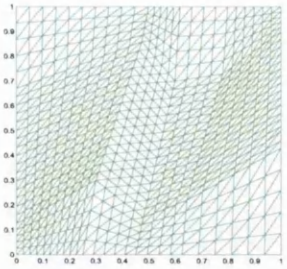

(a) Perturbed triangular mesh

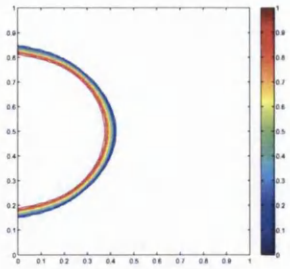

(b) Reference Solution on a 81x81 Cartesian Grid

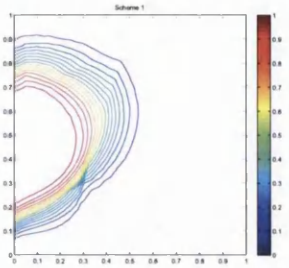

(c) Single point upwind Order

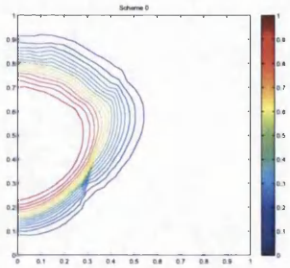

(d) Multi-D Edge-based

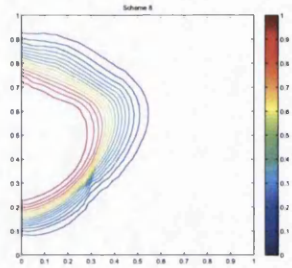

(e) Multi-D Cell-based

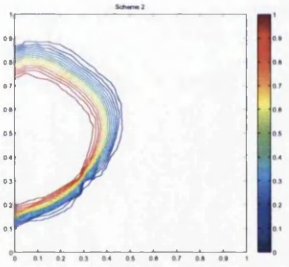

(f) Standard Higher-order

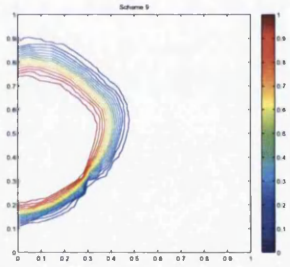

(g) Higher-order Multi-D Edge-based

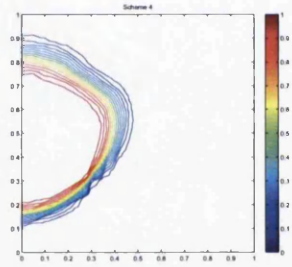

(h) Higher-order Multi-D Cell-based

Figure 10.4: Case 2 - Saturation profiles for the Source and Sink Linear problem.

along opposite sides of the rectangular domain, water saturation contours are shown at 0.2 PVI. First order results in Figure 10.4(c) show that the direction of triangulation effectively introduces a full tensor effect due to the strong local grid orientation.

The edge-based and cell-based Multi-D schemes both improve front resolution reducing the effect of grid orientation. The Standard higher order scheme improves front resolution, however visible signs of grid orientation remain in the solution. In contrast, the higher-order Multi-D schemes (Figures 10.4(g),(h)) provide higher resolution of the front while

reducing grid orientation.

10.3.3 Case 3: Nonlinear Full Tensor Piston Flow

The third case is a study of a nonlinear Buckley Leverett piston flow as in chapter 9 section 9.2.2. For completeness we include earlier results at the first order multidimensional schemes for easy comparison with higher order multidimensional results.
The results are computed on unstructured triangular and quadrilateral grids. The unstructured triangular grid is shown in Figure 10.5(a).
The nonlinear case also highlights the difference between the flux of Multi-D data and Multi-D flux. The results obtained using standard single-point upstream weighting are shown in Figure 10.5(b) and those obtained using the data based multidimensional wave-oriented higher dimensional upwind scheme are shown in Figures 10.6(a) edge based and 10.6(c) cell based. The multidimensional flux results are shown in Figures 10.6(b) and 10.6(d) on the unstructured triangular grid.
The standard first order results indicate a grid orientation bias whereas the results obtained with the multidimensional schemes show reduced grid dependence and provide a definite improvement in front resolution with a clearer indication of the flow pattern, particularly for the Multi-D cell-based schemes with results that are the most consistent with the problem. Reference solution on a 64x64 Cartesian grid is shown in 10.7(d).
The comparison between higher order schemes is illustrated in Figure 10.7. While solution resolution is consistently improved by use of the higher-order schemes, compared with the first order results, the cell-based higher order Multi-D scheme provides the best results.

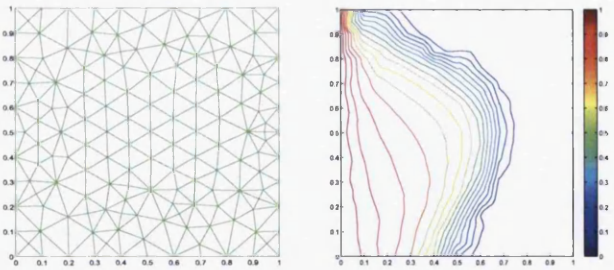

(a) Grid (b) SPU Cell-based

Figure 10.5: Case 3 - Standard first order saturation profile.

The equivalent unstructured quadrilateral grid (Figure 10.8(a)) which has the same

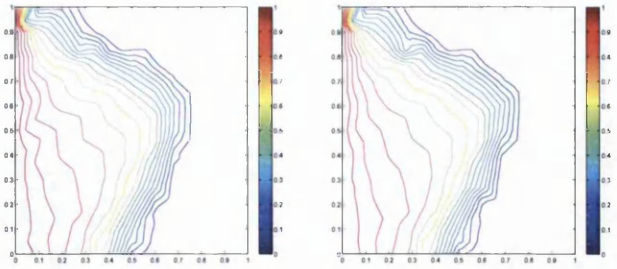

(a) Flux of Multi-D Data Edge-based

(b) Multi-D Flux Edge-based

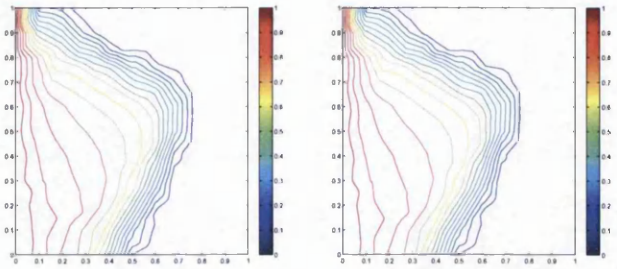

(c) Flux of Multi-D Data Cell-based

(d) Multi-D Flux Cell-based

Figure 10.6: Case 3 - Multi-Dimensional first order saturation profiles on triangular mesh.

vertices as the triangular grid of Figure 10.5(a) provides the second part of this test case. Standard first order upwind (Figures 10.8(b)). Both the first order and higher-order Multi-D comparisons clearly demonstrate that the cell-based Multi-D (Figure 10.9) and higher-order Multi-D schemes (Figure 10.10) consistently provide the best results.

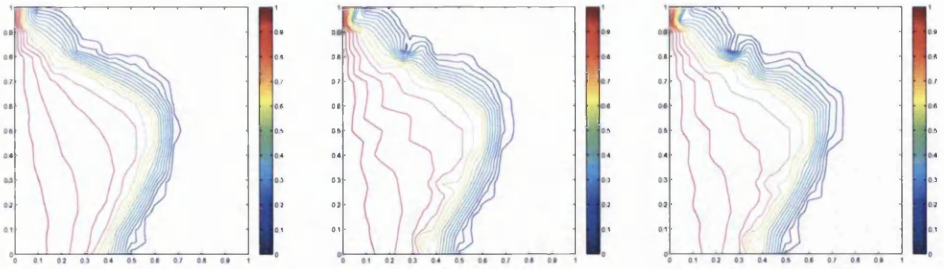

(a) Standard Higher-order

(b) Flux of higher-order Multi-D Data Edge-based

(c) Higher-order Multi-D Flux Edge-based

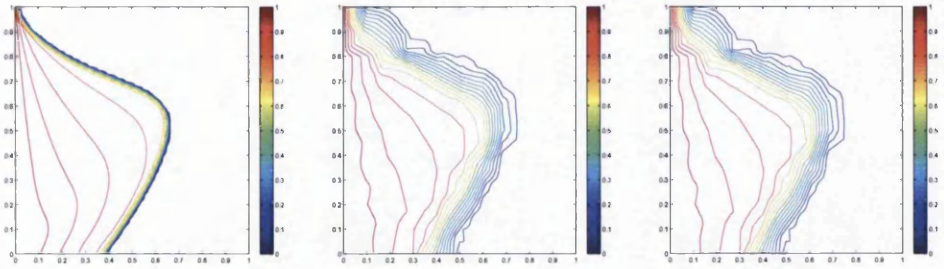

(d) Reference Solution on a 64x64 Cartesian Grid

(e) Flux of higher-order Multi-D Data Cell-based

(f) Higher-order Multi-D Flux Cell-Based

Figure 10.7: Case 3 - Higher order saturation profiles for the non-linear piston problem with full tensor on triangular mesh.

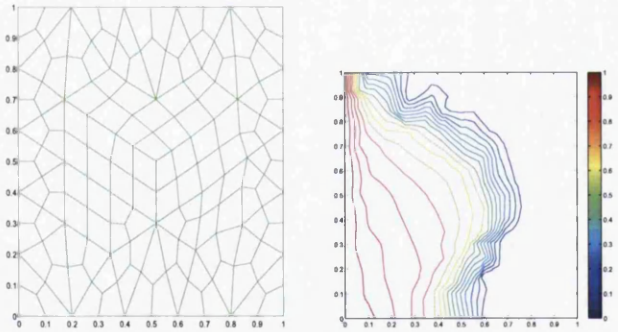

(a) Grid

(b) SPU Cell-Based

Figure 10.8: Standard first order saturation profile on quadrilateral mesh.

10.3.4 Case 4: Tracer Flow in a Heterogenous Medium

We return to the heterogeneous case of chapter 9, section 9.2.3. This case involves a tracer flow in a heterogeneous medium where injection and production wells are located

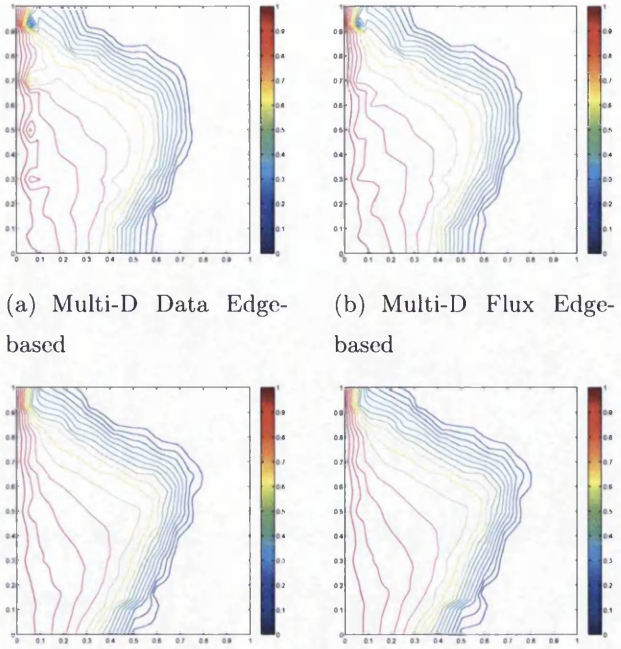

(a) Multi-D Data Edge-based

(b) Multi-D Flux Edge-based

(c) Flux of Multi-D Data Cell-based

(d) Multi-D Flux Cell-based

Figure 10.9: Case 3 - Multi-Dimensional first order saturation profiles on quad-mesh.

along opposite sides of the idealised reservoir domain. Results are obtained using a 30x110 uniform grid. Figure 10.11 shows the logarithm of the upscaled permeability field. Water saturation contours are shown at 0.005 pore volumes (PV) injected. Figure 10.12 shows saturation profiles computed with the standard single-point upwind method (Figure 10.12 (a)) and the higher order method (Figure 10.12 (d)).

The higher order method increases resolution significantly compared to the first order single-point upwind method, the standard first order method shows excessive numerical diffusion producing non-physical features in the numerical solution. The first order Multi-D edge based (Figure 10.12(b)) and cell based (Figure 10.12(c)) schemes provide similar and much improved solution resolution compared to the standard method, the first order Multi-D results are comparable to that of the standard higher-order scheme. The higher-order Multi-D schemes provide the best overall resolution of the finger like features of the solution Figures 10.12(e),(f).

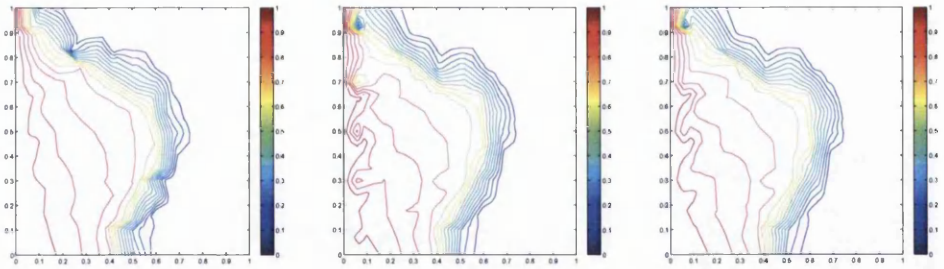

(a) Standard Higher-order

(b) Flux of Higher-order Multi-D Data Edge-based

(c) Higher-order Multi-D Flux Edge-based

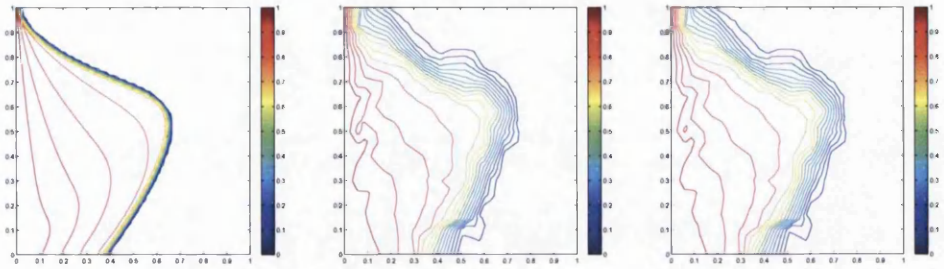

(d) Reference Solution on a 64x64 Cartesian Grid

(e) Flux of Higher-order Multi-D Data Cell-based

(f) Higher-order Multi-D Flux Cell-based

Figure 10.10: Case 3 - Higher order saturation profiles for the non-linear piston problem with full tensor on quad-mesh.

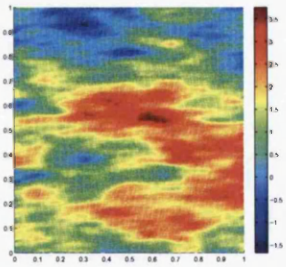

Figure 10.11: Logarithm of the upscaled permeability field.

10.4 Conclusions

Families of higher order edge-based and cell-based multidimensional upwind formulations are presented for hyperbolic conservation laws on general grids. The methods are coupled with consistent and efficient continuous Darcy flux approximations. The schemes are locally conservative, conditions for positivity of the schemes are defined for linear fluxes. The new methods permit higher CFL numbers than the standard upwind scheme.

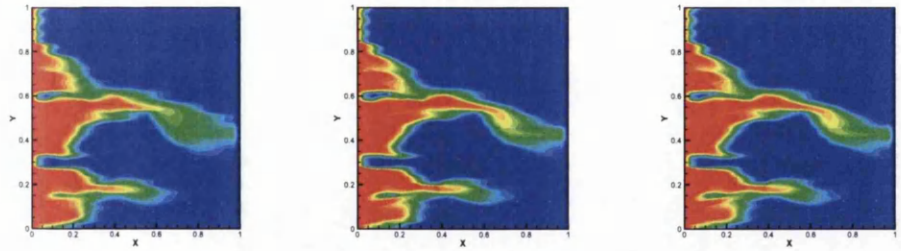

(a) Standard First Order (b) Multi-D Edge-Based (c) Multi-D Cell-Based

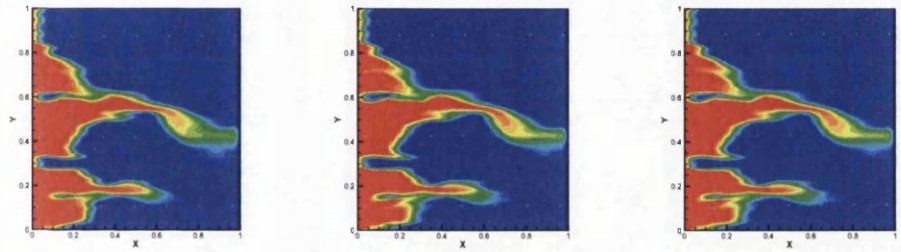

(d) Standard Higher-order (e) Higher-order Multi-D Edge-Based (f) Higher-order Multi-D Cell-Based

Figure 10.12: Case 4 - Saturation profiles for the heterogeneous Case.

The new methods are compared with single point upstream weighting for two-phase flow problems. The tests are conducted on both structured and unstructured grids and involve full-tensor coefficient velocity fields. The comparisons demonstrate the benefits of multidimensional and higher order multidimensional schemes in terms of improved front resolution together with significant reduction in cross-wind diffusion. For cases involving severe grid distortion the cell based multidimensional schemes prove to be more robust than the edge based schemes though both formulations provide notable improvement compared to single point upwind.

Chapter 11

Conclusions and Recommendations

11.1 Conclusions

In this thesis, families of novel edge-based and cell-based multidimensional upwind formulations have been presented for hyperbolic conservation laws on structured and unstructured triangular and quadrilateral grids in two dimensions. Higher resolution as well as higher order multidimensional formulations have also been developed for general structured and unstructured grids.

The schemes are coupled with previously developed consistent and efficient continuous CVD (MPFA) Darcy flux approximations. They are formulated using an IMPES (Implicit in Pressure Explicit in Saturation) strategy for solving the coupled elliptic (pressure) and hyperbolic (saturation) system of equations governing the multi-phase multi-component flow in porous media. The focus in this work is on the spatial discretisation of the multidimensional hyperbolic operator for time dependent problems where first order forward Euler time stepping is employed to advance the saturation front.

The multidimensional formulations are locally conservative, positivity conditions are derived for linear fluxes on unstructured meshes and permit higher CFL numbers than the standard upwind scheme.

The new methods have been compared with single point upstream weighting for two-phase and three-component two-phase flow problems. The tests are conducted on both structured and unstructured grids and involve full-tensor coefficient velocity fields in homogeneous and heterogeneous domains. The comparisons demonstrate the benefits of multidimensional and higher order multidimensional schemes in terms of improved front resolution together with significant reduction in cross-wind diffusion.

In this work, data based and flux based non linear flux approximations are presented. Two-phase flow numerical results show that the edge-based multidimensional flux formalism is more robust than the data based counterpart.
Numerical tests have also shown that while the edge-based formulation provides improved resolution compared to single point upwind, improved performance is obtained with the cell-based multidimensional formulation. This is attributed to the use of fine scale velocity field for characteristic tracing.
In addition, an extension of a class of higher order methods [57] to highly distorted unstructured triangular and quadrilateral grids for flow in porous media has been developed. A sequence of higher resolution non-uniform limiters are introduced and tested for classical two phase flow problems on triangular grids. The schemes are based on MUSCL reconstructions using extended stencils and provide significant improvement compared to standard first order methods.
The multidimensional first order edge-based upwind schemes have been applied to Gravity driven flow where different tracing velocity formulations are tested. Both higher order and multidimensional upwind schemes are also introduced for hyperbolic systems where different limiting strategies involving primitive, conservative and characteristic variables are adopted. Numerical test cases involving two phase three component flow show the benefits of the schemes when compared to standard first order approximations and illustrate the advantage of using the characteristic variables instead of the primitive and conservative variables.

11.2 Recommendations for Future Work

The work presented in this thesis is only the beginning for research and development of the family of higher order multidimensional schemes for hyperbolic conservation laws. This work has laid the foundation for further investigation, which will hopefully give even greater insight into this novel and interesting approach with application to subsurface reservoir simulation. Further possible research routes are suggested here:

i The schemes presented here are coupled with consistent CVD Darcy flux approximations. The quadrature point where the Darcy fluxes are evaluated at the grid edge mid-points where control volume sub-faces join. It has been shown [124] that improved pressure profile resolution is achieved using quadrature points along the

control volume sub-faces. Further investigations need to be carried out in this direction with combination to both cell-base and edge based first order and higher order multidimensional formulations.

ii The innovative higher resolution schemes have been implemented in one dimensional and two dimensional space. The extension of these schemes to 3D constitutes the next step in the development of truly higher dimensional unstructured schemes in reservoir engineering.

iii In this work, the positivity analysis has been performed for the multidimensional schemes on unstructured grids in the case of linear fluxes. A maximum principle analysis should be investigated for the general nonlinear fluxes in order to derive stability weighting factors.

iv The multidimensional schemes presented here use an IMPES strategy for the update of the saturation and concentration. A fully implicit formulation could be also used. Also, first order forward Euler time discretisation has been used to advance the reconstructed saturation data in time using the higher resolution spatial discretizations presented here. Higher order time accuracy is another aspect for further investigation.

v The higher order reconstruction considered here uses the MUSCL strategy which are second order accurate in space. Very high order accuracy could be achieved using alternative higher order interpolation methods such as discontinous galerkin schemes. The DG methods provide an attractive alternative as they use a compact stencil despite the increase in the number of degrees of freedom it might incur.

vi Here, edge-based multidimensional schemes have been applied to gravity driven flow and both phase velocity and characteristic speeds have been investigated for the tracing step via the use of a challenging water-oil gravity segregation case study on unstructured grids. We conclude that the characteristic multidimensional schemes produced the best results. Application of cell based multidimensional formalism and higher order multidimensional methods is the subject of ongoing research and will be the subject of future study.

Bibliography

[1] I. Aavatsmark. Introduction to multipoint flux approximation for quadrilateral grids. *Comput.Geo*, 6:405–432, 2002.

[2] I. Aavatsmark, T. Barkve, Ø. Bøe, and T. Mannseth. Discretization on non-orthogonal, curvilinear grids for multiphase flow. In *Proceedings of* 4^{th} *European Conference on the Mathematics of Oil Recovery*, Norway, 1994.

[3] I. Aavatsmark, T. Barkve, Ø. Bøe, and T. Mannseth. Discretization on non-orthogonal, quadrilateral grids for inhomogeneous, anisotropic media. *J.Comput.Phys.*, 127:2–14, 1996.

[4] I. Aavatsmark, T. Barkve, Ø. Bøe, and T. Mannseth. Discretization on unstructured grids for inhomogeneous, anisotropic media. part i: Derivation of the methods. *SIAM J.Sci.Comput.*, 19:1700–1716, 1998.

[5] I. Aavatsmark, T. Barkve, Ø. Bøe, and T. Mannseth. Discretization on unstructured grids for inhomogeneous, anisotropic media. part ii: Discussion and numerical results. *SIAM J.Sci.Comput.*, 19:1717–1736, 1998.

[6] R. Abgrall. Toward the ultimate conservative scheme: following the quest. *Journal of Computational Physics*, 167(2):277–315, 2001.

[7] R. Abgrall and T.J. Barth. Residual distribution schemes for conservation laws via adaptive quadrature. *SIAM J. Sci. Comput.*, 24(3):732–769, 2002.

[8] R. Abgrall and F. Marpeau. Residual distribution schemes on quadrilateral meshes. *J. Sci. Comput.*, 30(1):131–175, 2007.

[9] R. Abgrall and M. Mezine. Construction of second order accurate monotone and stable residual distribution schemes for unsteady flow problems. *J. Comput. Phys.*, 188(1):16–55, 2003.

[10] R. Abgrall and P.L. Roe. High order fluctuation schemes on triangular meshes. *J. Sci. Comput.*, 19(1-3):3–36, 2003.

[11] T Arbogast, M. F. Wheeler, and I. Yotov. Mixed finite elements for elliptic problems with tensor coefficients as cell centered finite differences. *SIAM J. Numer. Anal.*, 34(2):828–852, 1995.

[12] J.E. Arnes. On the use of mixed multiscale finite element method for greater flexibility and increased speed or improved accuracy in reservoir simulation. *Multiscale Model. Simul.*, 2(3):421–439, 2004.

[13] K. Aziz and A. Settari. *Petroleum Reservoir Simulation.* Applied Science Publishers, London, 1979.

[14] A.A. Baker, L.W. Gelhar, A.L. Gutjahr, and J.R. Macmillan. Stochastic analysis of spatial variability in subsurface flows, i. comparison of one-and three-dimensional flows. *Water Resour. Res.*, 14(2):263–271, 1978.

[15] T. Barth. Numerical methods and error estimation for conservation laws on structured and unstructured meshes. Von Karman Institute Computational Fluid Dynamics Lecture Notes, March 2003.

[16] T.J. Barth and D. C. Jesperson. The design and application of upwind schemes on unstructured meshes. *AIAA Paper 89-0366.*, 1989.

[17] T.J. Barth and M. Ohlberger. *Finite Volume Methods: Foundation and Analysis, Encyclopdeia of Computational Mechanics.* John Wiley and Sons, 2004.

[18] P. Batten, C. Lambert, and D. M. Causon. Positively conservative high-resolution convection schemes for unstructured elements. *Int. J. Numer. Methods Eng.*, 39, 1821-1838 1991.

[19] J. Bear. *Dynamics of Fluids in Porous Media.* Elsevier, New York, 1988.

[20] S.H. Begg, R.R. Carter, and P. Dranfield. Assigning effective values to simulator gridblock parameters for heterogeneous reservoirs. *SPE Reservoir Enginering*, 4(4):455–463, 1989.

[21] J. B. Bell, P. Colella, and J.A. Trangenstein. Higher order godunov methods for general systems of hyperbolic conservation laws. *Journal of Computational Physics*, 82(2):362–397, 1989.

[22] C. Berger, M.J.and Helzel and R.J. LeVeque. H-box methods for the approximation of hyperbolic conservation laws on irregular grids. *SIAM Journal on Numerical Analysis*, 41(3):893–918, 2003.

[23] M.J. Blunt and B. Rubin. Implicit flux-limiting schemes for petroleum reservoir simulation. *Journal of Computational Physics*, 102:194–210, 1992.

[24] R.H. Brooks and A.T. Corey. Hydraulic properties of porous media. Hydrology Papers 3, Colorado State Univerisity, Fort Collins, CO, 1964.

[25] T.F. Herrera I. Celia, M.A.and Russel and R.E. Ewing. An eulearian-lagrangian localized adjoin method for the advection-diffusion equation. *Advances in Water Resources*, 13(4):187–206, 1990.

[26] W.H. Chen, L.J. Durlofsky, B. Engquist, and S. Osher. Minimization of grid orientation effects through use of higher-order finite difference methods. *SPE Advanced Technology Series*, 1(2):4352, 1993.

[27] Z. Chen and T.Y. Hou. A mixed multiscale finite element method for elliptic problems with oscillating coefficients. *Math. Comp.*, 72:541–576, 2003.

[28] M.A. Christie and M.J. Blunt. Tenth spe comparative solution project: A comparison of upscaling techniques. *SPE Reservoir Evaluation Engineering*, 4(4):308–317, 2001.

[29] B. Cockburn. Disconuous galerkin methods for convection dominated problems. high-order methods for computational science and engineering, vol.9. *Springer-Verlag, Berlin*, 1999.

[30] B. Cockburn, G.E. Karniadakis, and C-W. (Eds.) Shu. *Lecture Notes in Computational Science and Engineering. The Development of Discontinuous Galerkin Methods. Discontinuous Galerkin Method. Theory, Computation and Applications.* Springer, Berlin, 2000.

[31] B. Cockburn and C-W. Shu. Tvb runge-kutta local projection discontinuous galerkin finite element method for scalar conservation laws ii: General framework. *Math. Comp.*, (52):411–435, 1989.

[32] B. Cockburn and C-W. Shu. The runge-kutta local projection p^1 discontinuous galerkin finite element method for scalar conservation laws. *RAIRO Modél. Math. Anal.Numer.*, (25):337–361, 1991.

[33] B. Cockburn and C-W. Shu. The runge-kutta discontinuous galerkin finite element method for conservation laws v: Multidimensional systems. *Journal of Computational Physics*, (141):199–224, 1998.

[34] S. Cockburn, B.and Hou and C-W. Shu. Tvb runge-kutta local projection discontinuous galerkin finite element method for conservation laws iv: The multidimensional case. *Math. Comp.*, (54):545–581, 1990.

[35] SY. Cockburn, B.and Lin and Shu C-W. Tvb runge-kutta local projection discontinuous galerkin finite element method for conservation laws iii: One dimensional systems. *Journal of Computational Physics*, (84):90–113, 1989.

[36] P. Colella. Multidimensional upwind methods for hyperbolic conservation laws. *Journal of Computational Physics*, 87(1):171–200, 1990.

[37] A.T. Corey. *Mechanics of Immiscible Fluids in Porous Media.* Water Resources Publications, Littleton, CO, 2nd edition edition, September 1986.

[38] M. Crandall and A. Majda. Monotone difference approximations of scalar conservation laws. *Math. Comp.*, 34:121, 1980.

[39] L.P. Dake. *Fundamentals of Reservoir Engineering.* Elsevier, Amsterdam, 1978.

[40] H. Darcy. Les fontaines publiques de la ville de dijon. 1856.

[41] H. Deconinck and R. Abgrall. Introduction to residual distribution methods. VKI Computational Fluid Dynamics Lecture Series, 06 2005-2006.

[42] H.K. Dhale, R.E. Ewing, and T.F. Russel. Eulerian-lagrangian localized adjoint method for advection-diffusion equation. *Comput. Methods Appl. Mech. Engrg*, 122:223–250, 1995.

[43] D.N. Dietz. A theoretical approach to the problem of encroaching and by-passing edge water. In *Proc. K. Ned. Akad. Wet.*, B 56, pages 83–92, 1953.

[44] R.E. Douglas, Jr. J.and Ewing and M.F. Wheeler. The approximation of the pressure by mixed method in the simulation of miscible discplacement. *A.A.I.R.O Analyse Numerique*, 17:17–33, 1983.

[45] R.E. Douglas, Jr. J.and Ewing and M.F. Wheeler. The approximation of the pressure by mixed method in the simulation of miscible discplacement. *A.A.I.R.O Analyse Numerique*, 17:249–265, 1983.

[46] L. J. Durlofsky, B. Engquist, and S. Osher. Triangle based adaptive stencils for the solution of hyperbolic conservation laws. *J. Comput. Phys.*, 98(1):64–73, 1992.

[47] L.J. Durlofsky. Numerical calculation of equivalent grid block permeability tensors for heterogeneous media. *Water Resources Research*, 27:699–708, 1991.

[48] L.J. Durlofsky. A triangle based mixed finite element finite volume technique for modeling two phase flow through porous media. *J.Comput.Phys*, 105:252–226, April 1993.

[49] M.G. Edwards. Multidimensional upwind schemes for systems of conservation laws with application to the euler equations. in preparation.

[50] M.G. Edwards. Symmetric, flux-continuous positive definite approximation of elliptic full tensor pressure equation in local conservation form. In *SPE 291471,* 13^{th} *SPE Reservoir Simulation Symposium*, pages 553–562, San Antonio, Texas,USA, 1995.

[51] M.G. Edwards. A higher order godunov scheme coupled with dynamic local grid refinement for flow in a porous medium. *Comput. Methods. Appl. Mech. Engrg*, (131):287 – 308, 1996.

[52] M.G. Edwards. M-matrix flux splitting for general full tensor discretization operator on structured and unstructured grids. *J. Comput. Phys.*, (160):1–28, 2000.

[53] M.G. Edwards. Unstructured, control-volume distributed, full tensor finite volume schemes with flow based grids. *Comput. Geo.*, (6):433–452, 2002.

[54] M.G. Edwards. Higher dimensional wave oriented upwind schemes with minimal cross-wind diffusion, spe 79689. In *SPE Reservoir Simulation Symposium*, Houston, Texas, USA, 3-5 Feb 2003.

[55] M.G. Edwards. Non-upwind versus upwind schemes for hyperbolic conservation laws in porous media, spe 93691. In *SPE Reservoir Simulation Symposium*, Houston, Texas, USA, 31 Jan - 2 Feb 2005.

[56] M.G. Edwards. Higher-order hyperbolic-coupled-elliptic flux-continuous cvd finite volume schemes in two and three dimensions. In *European Congress on Computational Methods in Applied Sciences and Engineering*, pages 273–277, Egmond aan Zee, The Netherlands, 5-8th Sept 2006.

[57] M.G. Edwards. Higher-resolution hyperbolic-coupled-elliptic flux-continuous cvd schemes on structured and unstructured grids in 2-d. *International Journal for Numerical Methods in Fluids*, 51(9-10):1059 – 1077, 2006.

[58] M.G. Edwards. Higher-resolution hyperbolic-coupled-elliptic flux continuous cvd schemes on structured and unstructured grids in 3-d. *International Journal of Numerical Methods in Fluids*, (51):1079–1095, 2006.

[59] M.G. Edwards and M.A. Christie. Dynamically adaptive godunov schemes with renormalization for reservoir simulation, spe 25268. In *Twelfth SPE Reservoir Simulation Symposium*, New Orleans, Louisiana, USA, Feb 28-Mar 3 1993.

[60] M.G. Edwards and M. Pal. Positive definite q-families of continuous subcell darcy-flux cvd(mpfa) finite volume schemes and the mixed finite element method. *International Journal for Numerical Methods in Fluids*, 57(4):355 – 387, 2008.

[61] M.G. Edwards and C.F. Rogers. A flux continuous scheme for the full tensor pressure equation. *Proceedings: 4^{th} European Conference on the Mathematics of Oil Recovery, Norway*, 1994.

[62] M.G. Edwards and C.F. Rogers. Finite volume discretization with imposed flux continuity for the general tensor pressure equation. *Comput. Geo.*, (2):259–290, 1998.

[63] M.G. Edwards and H. Zheng. A quasi-positive family of continuous darcy-flux finite-volume schemes with full pressure support. *Journal of Computational Physics*, 227(22):9333–9364, 2008.

[64] B. Engquist and S. Osher. Stable and entropy satisfying approximations for transonic flow calculations. *Math. Comp.*, 34:45–57, 1980.

[65] M.S. Espedal and R.E. Ewing. Characterstic petrov-galerkin subdomain methods for two-phase imiscible flow. *Computer Methods in Applied Mechanics and Engineering*, (46):113–135, 1987.

[66] R.E. Ewing and R.F. Heinemann. Incorporation of mixed finite element in compositional simulation for reduction of numerical dispersion, spe 12267. *Reservoir Simulation Symposium, San Fransisco*, pages 341–347, 1983.

[67] R.E. Ewing, T.F. Russel, and M.F. Wheeler. Simulation of miscible displacement using mixed methods and a modified methods of characterstics, spe 12241. *Reservoir Simulation Symposium, San Francisco*, 1983.

[68] R.E. Ewing and J. Wang. Analysis of multilevel decomposition iterative method for mixed finite element methods. *M^2AN, Math. Modelling and Numer. Anal.*, (28):377–398, 1994.

[69] R.E. Ewing and M.F. Wheeler. *Computational Aspects of Mixed Finite Element Methods, Numerical Methods for Scientific Computing (Ed. R.S. Stepleman).* North-Holland,NY.

[70] C.L. Farmer. Upscaling: a review. *International Journal of Numerical Methods in Fluids*, 40:63–78, 2002.

[71] L. Fung, L.S.-K.and Buchanan and R. Sharma. Hybrid-cvfe method for flexible grid reservoir simulation. In *12th SPE Symposium on Reservoir Simulation (SPE 25266)*, New Orleans, LA, February 28-March 3 1993. Society of Petroleum Engineers.

[72] L.W. Gelhar and C.L. Axness. Three-dimensional stochastic analysis of macrodispersion in aquifers. *Water Resour. Res*, (19(1)):161–180, 1983.

[73] E. Godlewski and P.A. Raviart. *Numerical approximation of hyperbolic systems of conservation laws.* New York, Springer, 1996.

[74] S.K. Godunov. A finite difference method for numerical computation of discontinuous solution of the equation of fluid dynamics. *Math. Sb.*, 47:271 – 290, 1959.

[75] J. Goodman and R.J. LeVeque. On the accuracy of stable schemes for 2d scalar conservation laws. *Mathematics of Computation*, 45(171):15–21, 1985.

[76] A. Harten. Higher resolution schemes for hyperbolic conservation laws. *J. Comput. Physics*, 49(3):357–393, 1983.

[77] A. Harten, B. Engquist, S. Osher, and S. R. Chakravarthy. Uniformly high order accurate essentially non-oscillatory schemes, iii. *J. Comput. Phys.*, 131(1):3–47, 1997.

[78] A. Harten, J. Hyman, and P. Lax. On finite-difference approximations and entropy conditions for shocks. *Comm. Pure Appl. Math.*, 29:297–322, 1976.

[79] Z.E. Heinemann and C.W. Brand. Gridding techniques in resevoir simulation. In *First International Forum on Reservoir simulation*, pages 339–426, Alpbach, Austria, 1988.

[80] Z.E. Heinemann, C.W. Brand, M. Munka, and Y.M. Chen. Modeling reservoir geometry with irregular grids, spe 18412. *10th SPE Reservoir Simulation Symposium, Houston, Feb.6-8*, 1989.

[81] C. Helzel, M.J. Berger, and R.J. LeVeque. A high-resolution rotated grid method for conservation laws with embedded geometries. *SIAM Journal on Scientific Computing*, 26(3):785–809, 2005.

[82] Ch. Hirsch. *Numerical Computation of Internal and External Flows*, volume 2. John Wiley, New York, 1990.

[83] Ch. Hirsch and P. van Ransbeek. Cell centered multidimensional upwind algorithm and structured meshes. In Elsevier, editor, *Proceedings of ECOMAS 1st European CFD Conference*, volume 1, pages 53–60, Amsterdam, The Netherlands, 1992.

[84] R.H.W. Hoppe and B. Wohlmuth. Multilevel iterative solution and adaptive mesh refinement for mixed finite element discretizations. *Applied Numerical Mathematics: Transactions of IMACS*, 23(1):97–117, 1997.

[85] U. Hornung. *Homogenization and Porous Media.* Springer-Verlag,NY, 1997.

[86] H. Hoteit and A. Firoozabadi. Compositional modeling by the combined discontinuous galerkin and mixed methods. *SPE J.*, 11(1):19–34, March 2006.

[87] T.Y. Hou and X.H. Wu. A multiscale finite element method for elliptic problems in composite material and porous media. *J. Comput. Phys.*, (134):169–189, 1997.

[88] M.E. Hubbard and M.J. Baines. Conservative multidimensional upwinding for the steady two-dimensional shallow water equations. *Journal of Computational Physics*, 138(2):419–448, 1997.

[89] J.M. Hyman, R. Knapp, and J.C. Scovel. High order finite volume approximations of differential operators on nonuniform grids. *Physica D*, 60:112–138, 1992.

[90] J.M. Hyman, M. Shashkov, and S. Steinberg. The numerical solution of diffusion problems in strongly heterogeneous non-isotropic materials. *J. Comput. Phys*, pages 327 – 344, 1990.

[91] A. Jameson. Artificial diffusion, upwind biasing, limiters and their effect on accuracy and convergence in transonic and hypersonic flows. american institite for aeronautics and astronautics. Technical report, IAII, 1993.

[92] A. Jameson. Analysis and design of numerical schemes for gas dynamics 1, artificial diffusion, upwind biasing, limiters and their effect on multigrid convergence. *Int. J. of Comp. Fluid Dyn*, 4:171–218, 1995.

[93] A. Jameson and D.A. Caughey. A finite volume method for transonic flow calculations. *AIAA Paper*, pages 77 –635, 1977.

[94] W. Jameson, A.and Schmidt and E. Turkel. Numerical solution of the euler equations by finite volume methods using rungekutta time-stepping schemes. *AIAA Paper*, page 811259, 1981.

[95] P. Jenny, S.H. Lee, and H.A. Tchelepi. Adaptive multiscale finite volume method for multiphase flow and transport in porous media. *Multiscale Model. Simul.*, 3(1):50–64, 2004.

[96] V.V. Jikov, S.M Kozlov, and O.A. Oleinik. *Homogenization of Differential Operators and Integral Functionals.* Springer-Verlag,NY, 1994.

[97] A.G. Journel, C.V. Deutsch, and A.J. Desbarats. Power averaging for block effective permeability, spe15128. *SPE Californial Regional Meeting, Oaklands, California*, 1986.

[98] P.R. King. The use of renormalization in calculating effective permeability. *Transport in Porous Media*, 4:37, 1989.

[99] B. Koren. Low-diffusion rotated upwind schemes, multigrid and defect corrections for steady, multidimensional euler flows. *International Series of Numerical Mathematics*, 98:265–276, 1991.

[100] J. Kozdon, B. Mallison, and M. Gerritsen. Robust multi-d transport schemes with reduced grid orientation effects. *Transport in Porous Media*, 78(1):47–75, 2008.

[101] M.S. Lamine and M.G. Edwards. Higher order multidimensional wave oriented upwind schemes for flow in porous media on unstructured grids, spe 119187. In *SPE Reservoir Simulation Symposium*, The Woodlands, Texas, USA, 2-4 February 2009.

[102] M.S. Lamine and M.G. Edwards. Higher dimensional upwind schemes for flow in porous media on unstructured grids. In *ECMOR XI, 11th European Conference on the Mathematics of Oil Recovery*, Bergen, Norway, 8 - 11 September 2008.

[103] S. Lamine and M.G. Edwards. Multi-dimensional upwind convection schemes for flow in porous media on structured and unstructured quadrilateral grids. *preprint.*

[104] S. Lamine and M.G. Edwards. Multi-dimensional wave oriented upwind convection schemes for flow in porous media on structured and unstructured grids. *preprint.*

[105] S. Lamine and M.G. Edwards. Multi-dimensional wave oriented upwind convection schemes for flow in porous media on triangular grids. *preprint.*

[106] S. Lamine and M.G. Edwards. Higher-resolution convection schemes for flow in porous media on highly distorted unstructured grids. *International Journal for Numerical Methods in Engineering*, 76(8):1139–1158, 2008.

[107] S. Lamine and M.G. Edwards. Higher-dimensional wave oriented upwind convection schemes for flow in porous media on structured and unstructured grids. In *ACOMEN Advanced Computational Engineering Methods*, Liege, Belgium, 26-28 May 2008.

[108] S. Lamine and M.G. Edwards. Unstructured higher resolution convective schemes for flow in porous media. In *ECMOR X, 10th European Conference on the Mathematics of Oil Recovery*, Amsterdam, Netherlands, 4 - 7 September 2006.

[109] S. Lamine and M.G. Edwards. Non upwind discontinuous galerkin schemes for hyperbolic conservation laws in porous media. In *ECCOMAS CFD, European Conference on Computational Fluid Dynamics*, TU Delft, The Netherlands, 5-8 September 2006.

[110] P.D. Lax. Weak solution of nonlinear hyperbolic equations and their numerical computation. *Comm. Pure. Appl. Math.*, 7:159–193, 1954.

[111] P.D. Lax and B. Wendroff. System of conservation laws. *Comm. Pure. Appl. Math.*, 13:217–237, 1960.

[112] R.J. Leveque. *Numerical Methods for Conservation Laws.* Lecture in Mathematics, ETH-Zurich, Birkhauser Verlag,Basel, 2^{nd} edition, 1994.

[113] R.J. Leveque. *Finite Volume Methods for Hyperbolic Problems.* Cambridge University Press-London, 2002.

[114] X-D Liu. A maximum principle satisfying modification of triangle based adaptive stencils for the solution of scalar hyperbolic conservation laws. *SIAM J. Numer. Anal.*, 30(3):701–716, 1993.

[115] X-D Liu and Peter D. Lax. Positive schemes for solving multi-dimensional hyperbolic systems of conservation laws ii. *J. Comput. Phys.*, 187(2):428–440, 2003.

[116] X-D Liu, S Osher, and T Chan. Weighted essentially non-oscillatory schemes. *J. Comput. Phys.*, 115(1):200–212, 1994.

[117] X.D. Liu and S. Osher. Conevx eno high order multidimensional schemes without field by field decomposition on staggered grids. *Journal of Comuptational Physics*, 141:1–27, 1998.

[118] P.R.M. Lyra and K. Morgan. A review and comparative study of upwind biased schemes for compressible flow computation. part iii: Multidimensional extension on unstructured grids. *Archives of Computational Methods in Engineering*, 9(3):207–256, September 2002.

[119] Ch. Marle. *Multiphase Flow in Porous Media.* Editions TECHNIP, 1981.

[120] I. Mishev and S. Nepomnyaschikh. Domain decomposition methods for reservoir simulation problems. *IMACS Conference on Iterative Methods in Scientific Computation, TAMU, Texas*, 2006.

[121] S. Osher. Riemann solvers, the entropy condition, and difference approximations. *SIAM J. Numer. Anal.*, 21(2):217235., 1984.

[122] M. Pal and M.G. Edwards. Quasi-monotonic continuous darcy-flux approximation for general 3-d grids of any element type, spe106486. In *SPE Reservoir Simulation Symposium*, Houston, Texas-USA, 2007.

[123] M. Pal and M.G. Edwards. Convergence of a family of multi-point flux approximation schemes on unstructured grids in two and three dimensions. In *ACOMEN*, Liege, Belgium, 2008.

[124] M. Pal, M.G. Edwards, and A.R. Lamb. Convergence study of a family of flux-continuous finite schemes for the general tensor pressure equation. *International Journal for Numerical Methods in Fluids*, 51:1177–1203, 2006.

[125] C. Palagi. *Generation and Application of Voronoi Grid to Model Flow in Heterogeneous Reservoirs.* PhD thesis, Standford University, 1992.

[126] K. Palagi, C.and Aziz. Use of voronoi grids in reservoir simulation (spe 11889 and 26951). In *Proceedings of the SPE 66th Annual Technical Conference and Exhibition*, Dallas, Texas; Houston, Texas., October 69 1991. Society of Petroleum Engineers.

[127] D.J. Parpia, I.H.and Michalec. Grid-independent upwind scheme for multidimensional flow. *AIAA Journal*, 31(4):646–651, 1993.

[128] D.W. Peaceman. A nonlinear stability analysis for difference equation using semi-implicit mobility. *Trans AIME 263 Soc.Petr.Eng.J.*, 17:79–91, 1977.

[129] K.G. Powell, B. van Leer, and P.L. Roe. Towards a genuinly multi-dimensional upwind scheme. VKI Computational Fluid Dynamics Lecture Series, 03 1993.

[130] M.H. Protter and H.F Weinberger. *Maximum Principles in Differential Equations.* Springer, 1984.

[131] M. Prvost, M.G. Edwards, and M.J. Blunt. Streamlines tracing on curvilinear structured and untructured grids. In *SPE Reservoir Simulation Symposium*, number SPE 66347, Houston, Texas, 11-14 February 2001. SPE.

[132] G. D. Raithby. Skew upstream differencing schemes for problems involving fluid flow. *Computer Methods in Applied Mechanics and Engineering*, 9:153–164, October 1976.

[133] M. Ricchiuto, R. Abgrall, and H. Deconinck. Application of conservative residual distribution schemes to the solution of the shallow water equations on unstructured meshes. *J. Comput. Phys.*, 222(1):287–331, 2007.

[134] J. Rice and R. Schnipke. A monotone streamline upwind method for convection-dominated problems. *Comput. Methods Appl. Mech. Engrg.*, 48:313–327, 1985.

[135] B. Riviere. Discontinuous galerkin method for solving the miscible displacement problem in porous media. *Ph.D.thesis, The University of Texas at Austin*, 2000.

[136] B. Riviere. *Discontinuous Galerkin Methods for Solving the miscible displacement in porous media.* PhD thesis, The University of Texas at Austin, May 2000.

[137] B. Riviere, M.F. Wheeler, and K. Banas. Discontinuous glaerkin method applied to a single phase flow in porous media. *Comput.Geo*, (49):337, 2000.

[138] P. L. Roe and D. Sidilkover. Optimum positive schemes for advection in two and three dimensions. 29(6):1542–1568, Dec 1992.

[139] P.L. Roe. Characteristic-based schemes for the euler equations. *Annual Review of Fluid Mechanics*, 18:337365, 1986.

[140] P.L. Roe. Approximate riemann solvers, parameter vectors, and difference schemes. *J. Comput. Phys.*, 135(2):250–258, 1997.

[141] P.L. Roe, H. Deconinck, and R.J. Struijs von Karman. Fluctualtion splitting for multidimensional convection problems: An alternative to finite volume and finite element methods. VKI Computational Fluid Dynamics Lecture Series, 03 1990.

[142] P.L. Roe, H. Deconinck, and R.J. Struijs von Karman. Recent progress in multidimensional upwinding. In K. W. Morton, editor, *Numerical Methods in Fluid*

Dynamics, volume 371 of *Lecture Notes in Physics, Berlin Springer Verlag*, pages 273–277, 1990.

[143] B. Rubin and M. J. Blunt. Higher-order implicit flux limiting schemes for black oil simulation, spe21222. In *11th SPE Symposium on Reservoir Simulation*, 1991.

[144] B. Rubin and M.G. Edwards. Extension of the tvd mid-point scheme to higher order accuracy in time, spe 25265. In *Twelfth SPE Reservoir Simulation Symposium*, pages 375–386, New Orleans, Louisiana, USA, Feb 28-Mar 3 1993.

[145] T. Russel, F., and M. F. Wheeler. Finite element and finite difference methods for continuous flows in porous media. *Chapter 2, in the Mathematics of Reservoir Simulation, R.E. Ewing ed, Frontiers in Applied Mathematics SIAM*, pages 35 –106, 1983.

[146] T. F. Russel and M. A. Celia. An overview of research on eulerian-lagrangian localized adjoint method (ellam). *Advances in Water Resources Research*, (25(8-12)):1215–1231, 2002.

[147] G.E. Schneider and M.J. Raw. A skewed, positive influence coefficient upwindinf procedure for control-volume-based finite-element convection-diffusion computation. *Numerical Heat Transfer, Part A: Applications*, 9(1):1–26, 1986.

[148] C.W. Shu and S. Osher. Efficient implementation of essentially non-oscillatory shock-capturing schemes,ii. *Journal of Computational Physics*, 83(1):32–78, 1989.

[149] G.R. Shubin and J.B. Bell. An analysis of the grid orientation effect in numerical simulation of miscible displacement. *Computer Methods in Applied Mechanics and Engineering*, 47:47–71, December 1984.

[150] D. Sidilkover. *Numerical solution to steady-state problems with discontinuities.* PhD thesis, Weizmann Institute of Science, Rehovot, Israel, 1989.

[151] D. Sidilkover. A genuinly multidimensional upwind scheme and an efficient multigrid for compressible euler equations. Technical report, ICASE, 1994.

[152] P. K. Smolarkiewicz and Szmelter J. Mpdata: an edge-based unstructured-grid formulation. *Journal of Computational Physics*, 206(2):624–649, 2005.

[153] S.P. Spekreijse. Multigrid solution of monotone second-order discretizations of hyperbolic conservation laws. *Mathematics of Computation*, 49:135155, 1987.

[154] G. Strang. On the construction and comparison of finite difference schemes. *SIAM J. Numer. Anal.*, 5:506–517, 1968.

[155] R. Struijs, H. Deconinck, and P.L. Roe. Fluctuation splitting schemes for the 2d euler equations, vki ls 1991-01,. *Comput. Fluid Dynam.*, 1991.

[156] P.K. Sweby. High resolution schemes using flux limiters for hyperbolic conservation laws. *SIAM Journal on Numerical Analysis*, 21(5):995–1011, October 1984.

[157] M. Thiele and M.G. Edwards. Physically based higher order godunov schemes for reservoir simulation for compositional simulation, spe 66403. In *SPE Reservoir Simulation Symposium*, Houston, Texas, USA, Feb 11-14 2001.

[158] M.Th. van Genuchten. A closed form equation for predicting the hydraulic conductivity in soils. *Soil Sci. Soc. Arm.*, 44:892–898, 1980.

[159] B. van Leer. Multidimensional explicit difference schemes for hyperbolic conservation laws. *Computing Methods in Applied Sciences and Engineering VI.*

[160] B. van Leer. Towards the ultimate conservative difference scheme, v. a second-order sequel to godunov's method. *J. Comput. Phys.*, 32:101–236, 1979.

[161] S. Verma. *Flexible grids for reservoir simulation.* PhD thesis, Stanford University, 1996.

[162] S. Verma and K. Aziz. Two and three dimensional flexible grids in reservoir simulation. 5^{th} *European Conference on Mathematics of oil Recovery, Leoben, Austria, 3-6 Sept*, 1996.

[163] S. Verma and K. Aziz. A control volume scheme for flexible grids in reservoir simulation. In *Proceedings of the Reservoir Simulation Symposium (SPE 37999)*, page 13p., Houston, Texas., October 69 1997. Society of Petroleum Engineers.

[164] H. K. Versteeg and W. Malalasekera. *An Introduction to Computational Fluid Dynamics: The Finite Volume Method.* Reading, MA: Addison-Wesley, 1995.

[165] M. F. Wheeler and I. Yotov. Physical and computational domain decomposition for modeling subsurface flows. *Contemp. Math.*, 218:217–228, 1998.

[166] P. Woodward and P. Colella. The numerical simulation of two-dimensional fluid flow with strong shocks. *Journal of Computational Physics*, 54:115–173, April 1984.

[167] L.C. Young. A study of spatial approximation for simulating fluid displacements in petroleum reservoirs. *Comp. Meth. in Appl. Mech. Eng.*, (47):2–46, 1984.

[168] K. Zhang, Y.S. Wu, C. Ding, K. Pruess, and E. Elmroth. Parallel computing techniques for large-scale reservoir simulation of multi-component and multiphase fluid flow. *SPE Reservoir Simulation Symposium, Houston - Texas*, (SPE 66343), 2001.